Universität Duisburg-Essen
Institut für Produkt Engineering
Lehrstuhl für Werkstofftechnik

NORTHWESTERN UNIVERSITY

Diplomarbeit

zum Thema

New Insights in Interfaces and Hard Phases of CoCrMo Alloys

vorgelegt von:

Priska Stemmer

Matrikelnummer: 2216470

Betreuer:

Prof. Laurence D. Marks

Prof. Dr.-Ing. Alfons Fischer

24.06.2011

Acknowledgment

Of the many people who have been enormously supportive in the preparation of this thesis, I am especially thankful to Prof. L. D. Marks and Prof. Dr.-Ing. A. Fischer for giving me the opportunity to work on that project and for supervising me during my thesis.

I also want to warmly acknowledge Yifeng Liao, Robin Pourzal, Birgit Gleising, Ralf Theissmann, Prof. Dudzinski and the members of the EPIC-Center for their help and many useful discussions.

I also want to thank the German Academic Exchange Service (Deutscher Akademischer Austausch Dienst, DAAD) for the financial support.

Lastly, I offer my regards and blessings to all of those who supported me in any respect during the completion of the project.

I. Index

II. Terminology

BF	Bright field
EDS/EDX	Energy-dispersive x-ray spectroscopy
EELS	Electron energy loss spectroscopy
FIB	Focused ion beam
GB	Grain boundary
HC	High carbon
MoM	Metal on metal
PB	Phase boundary
SEM	Scanning electron microscope
STEM	Scanning transmission electron microscope
TEM	Transmission electron microscope
ZC	Z-contrast (Z: atomic number)

1. Introduction

CoCrMo alloys are commonly used for orthopedic prostheses such as knee and hip replacements. As is generally known, the structure and chemical composition of materials influence its properties and performance [1]. In order to increase durability and minimize wear of metal on metal hip implants it is necessary to get a better understanding the influence of the alloy microstructure on its wear behavior. It was shown [2] that the microstructure of CoCrMo alloys used in hip implants varies largely in their grain size and the appearance of hard phases. CoCrMo alloys are standardized by ASTM but only concerning its chemical composition and mechanical properties.

The aim of this study was the investigation of grain boundaries of wrought CoCrMo alloys concerning chemical alterations as well as phase boundaries and hard phases within wrought and cast cobalt-based alloys used in metal-on-metal hip replacements.

2. Background

2.1 Grain boundaries

Grain boundaries generate during alloy solidification. Grain growth starts with nucleation and growth of small crystallites. These crystallites continue to grow until they encounter adjacent crystals. In general, the individual grains will differ in their orientation [3]. Grain boundaries can appear atomically sharp and coherent, semicoherent with networks of interfacial dislocations or incoherent [4].

Grain boundaries have an essential influence on many material properties and physical phenomenons, such as plastic deformation and fracture, transport processes or phase transformations [4].

2.2 Diffusion

Most phases in technical alloys are more or less far from the equilibrium state. Hence, they exist only at low temperatures where atoms and molecules are practically immobile. At higher temperatures atoms can move from one lattice site to another, this process is called diffusion. The diffusion of solute elements is directed toward the lowest free enthalpy, which often correlates with the concentration gradient.

In metals diffusion can either occur interstitial or substitutional. Interstitial atoms have to conquer the activation energy when jumping in between the lattice. The atoms gain the required energy due to thermally induced lattice oscillations. Thus, the frequency of jumps increases with the temperature.

For substitutional jumps a vacant lattice site is needed additional to reach the activation energy. Thus, the diffusion of substitutes also depends on the amount of vacancies within the lattice. In crystals dislocations and

grain boundaries support diffusion that means a decrease of the activation energy. [5]

2.3 Segregation

Segregation is the uneven distribution of alloying elements within the microstructure. Commonly, solidification of alloys proceeds on a temperature range, while partitioning and redistribution of solute amongst solid and liquid phases take place in an attempt to maintain chemical equilibrium. Segregation occurs when overall equilibrium is not attained. The effects of segregation can be reduced or eliminated due to heat treatments. [6]

When the solute segregates on the grain boundaries, the physical properties of the grain boundaries, such as energy, cohesion, mobility, sliding, diffusion, precipitation and corrosion can be seriously influenced. This, on the other hand, affects the properties of the bulk material like temper brittleness, recrystallization, grain growth, diffusion creep, fatigue strength and stress corrosion cracking. [7]

2.4 Nano-indentation

Nano-indentation can be used to measure mechanical properties of materials on the submicron scale. Atomic force microscopy (AFM) is used to image the indentation.

With the use of instruments which are able to continuously measure force and displacement during an indentation load-displacement curves can be recorded. With help of the measured data the two most frequent measured mechanical properties, hardness H and elastic modulus E can be calculated. The hardness is defined by the equation:

$$H = \frac{P_{max}}{A}$$

where P_{max} is the maximum load and A is the projected area. The projected area of the indent can be calculated when the tip geometry (usually a Berkovich tip) is known. The Berkovich tip is a three sided pyramid with a total included angle of 142.3° and an a half angle of 65.3°.

The Young´s modulus can be determined by using parameters from the unloading curve. The unloading curve is fit using the power law relation

$$P = C(h - h_f)^m$$

here, P is the load, $(h\text{-}h_f)$ the elastic displacement and C and m are material constants. The reduced modulus E_r results from the equation:

$$E_r = \frac{\sqrt{\pi}}{2\sqrt{A}} S$$

where S is the stiffness. [8]

2.5 TEM-analyzing methods

2.5.1 Energy dispersive x-ray spectroscopy (EDS)

To generate the emission of x-rays a high energetic beam has to strike the specimen [9].

If the electrons of the incident beam eject an electron from an inner shell of an atom, it creates an electron hole. This hole gets filled with an electron of a higher energetic shell. The difference within the energies is emitted in form of an x-ray. The energy of the x-ray is characteristic for the element and the shell from which it was emitted [10]. Only about 1% of the emitted characteristic x-rays get recorded by an EDX detector [11].

A detector connected to a multichannel analyzer counts the emitted x-rays which can be sorted on the basis of their energies [12].

Advantages of energy dispersive x-ray spectroscopy are that it is easy to use and the results can be quickly interpreted. A disadvantage of EDS compared to EELS is the low energy resolution which is >100 eV and <1 eV, respectively [9].

2.5.2 Electron energy-loss spectroscopy (EELS)

The analysis of energy distribution of electrons which have passed a specimen is called electron energy-loss spectroscopy. When the electrons pass through a very thin sample they may pass without interaction with the specimen or they may have lost energy due to inelastic collision [9].

If an electron passes through a thin specimen and undergoes inelastic scattering it loses a certain amount of energy and its path gets slightly deflected. Inelastic scattering is caused by phonon, plasmon, single valence electron or inner shell excitation. The energy loss can be measured with a magnetic spectrometer which is mounted behind the sample. Before the electron hits the position sensitive detector a magnetic field deflects the path of the electron with a 90° angle. Electrons with greater energy undergo slightly less deflection and the beam is dispersed into a spectrum of energies.

An electron energy loss spectrum is usually built up of three regions: The zero loss peak, which is generated from electrons which have suffered just a negligible amount of energy on their way through the sample, that is usually the majority.

The low loss region is characterized by plasmon peaks caused by electrons which have lost up to around 50 eV. Those electrons which have excited one plasmon on their passage through the specimen built the first plasmon peak. After the first plasmon peak there can be several more

corresponding to those electrons which have excited more than one plasmon. If the fourth plasmon peak is visible the specimen is too thick to be useful for analysis.

For analytic purpose the absorption edges at higher energies, between around 100 eV and 2000 eV, are used. Those edges are characteristic for each element and can be compared with tabulated values. One advantage of EELS compared with EDX is that it can detect edges of element whose x-rays are too soft to be measured. [13]

2.5.3 Energy filtered transmission electron microscopy (EFTEM)

Like EELS EFTEM detects energy losses of electrons caused by inelastic scattering from interaction with the specimen. For EFTEM images only electrons of particular energies are used. Those are filtered using an energy-selecting slit. EFTEM images using the absorption edges correspond to elemental maps. The simplest way to generate qualitative information in terms of elemental distribution is to subtract a pre-edge background image and a post edge image. [9]

3. Material and methods

3.1 Material

The studied samples were four DePuy MoM retrievals. Two couples were made of high carbon (hc) wrought alloy (PT09-285, PT10-117) and two of hc cast alloy (PT09-238, PT10-004). All of them had to be removed at an early stage due to aseptic loosening or pain. The duration was between 13 and 79 month.

Further an hc wrought alloy (hip 004 (ULTIMA, Warsaw, IN, USA)) and an hc cast alloy (hip 17 (ASR, Warsaw, IN, USA)) from DePuy have been investigated. (Table 1)

3.2 Sample preparation

3.2.1 Optical and secondary electron microscopy

The preparation for the optical microscopy (OM) and secondary electron microscopy (SEM) samples required polished and etched samples to visualize the microstructure.

Whenever a good marginal sharpness was required the samples have been embedded, using duroplast. Otherwise the samples have been glued onto a steel block using wax. Grinding and polishing has been carried out using manual grinding and polishing plates. The samples have been grinded via 320 emery paper and polished with 6 µm and 3 µm on an ultra-pol cloth (Struers) and 1 µm on a micro-cloth (Struers).

The etchant was a mixture of H_2O, 32%-HCl (hydrochloric acid) and $K_2S_2O_5$ (potassicdisulfite).

For the scanning electron microscopy an Hitachi S-3400 VP-SEM has been used.

3.2.2 Nano-indentation test

Samples for investigation using nano-indentation have to be flat and coplanar to prevent the tip of being damaged. Depending on the sample size embedded and unembedded samples were used.

To investigate the hardness of the hard phases it was necessary in some cases to use polished samples because its surface roughened due to the etching process making it impossible to get applicable results from the nano-indentation. A micro-hardness tester (Duramin 5, Struers) has been used to mark hard phase locations which were not visible in the polished state using the optical microscope of the tribo-indenter.

The polishing protocol was the same as for the optical and secondary electron microscopy. The measurements have been progressed on a Hysitron TI-950 TriboIndenter.

3.2.3 Transmission electron microscopy

Due to the use of analyzing techniques like EELS and EFTEM very thin samples were necessary. Therefore a FIB (FEI Helios NanoLab) was employed for accurate sample preparation.

To protect the surface from damage caused by the electron and ion beam, the samples have been sputtered with an approximately 15 nm thick gold layer. After finding the desired location on the sample an around 300 nm thick platinum layer has been depositioned on the surface using the electron beam at 2 kV and 2.7 nA. After tilting the sample about 52 a second platinum layer with a thickness of approx. 3 µm has been put upon the first using the ion beam at 30 kV and 93 pA/0.28 nA. The surrounding bulk material has been removed with the Ga ion beam. To reduce ion beam induced artifacts, lower voltages and currents have been used to thin the sample down to around 1.5 µm. Afterwards the sample has been loosened from the surrounding material using the so called ‘U-cut’. Using

the Omniprobe the sample could be lifted out and mounted on a TEM grid. The mounted sample has been thinned using the ion beam with decreasing currents and voltages to minimize ion beam induced damage.

The specimen have been investigated using an Hitachi HD2300-A STEM and an JOEL J2100F TEM.

4. Results

4.1 Hard phases introduction

The investigation of the specimens revealed different phases within the alloys. In wrought alloys (Figure 3 a) carbides of different types ($M_{23}C_6$, M_7C_3 or M_6C) and in various sizes (coarse: 3-8 µm; fine: 1-2 µm; very fine: ~0.5 µm) were found as well as fine and very fine intermetallic phases.

In cast alloys fine (1-15 µm) lamellar carbides of the types $M_{23}C_6$ and M_7C_3 were found (Figure 3 b). Also three different mixed phases were observed. Figure 3 c) shows a coarse (>15 µm) mixed hard phase (type I) with a pitted structure composed of nano-sized carbides and intermetallic phases. In Figure 3 d) a mixed hard phase (type II) with a smooth structure made up of different phases is shown. The mixed percolated phase (Figure 3 e) is characterized by fine carbides within the mixed phase. Figure 3 f) shows an arrangement of fine hard phases (carbides and intermetallic phases).

4.2 Microstructure

The microstructure of the hc wrought alloy retrievals (PT09-285, PT10-117) exhibited typical fine grains. The cups had a homogeneous microstructure with fine evenly distributed hard phases. The heads on the contrary had a banded structure with hard phase rich and depleted regions (Figure 4).

The ZC-images in Figure 5 of PT10-117 head and cup show very fine intermetallic phases on the grain boundaries as well as some fine carbides. The specimens PT09-285 on the other hand exhibited pits on the

grain boundaries and within the grain as well as some fine intermetallic phases and carbides.

The EDX mapping of PT10-117 cup exhibited intermetallic phases on the grain boundaries (Figure 6) and molybdenum-rich intermetallic phases with an increased silicon content (Figure 7).

The OM-images of the hc cast alloys (PT09-238, PT10-004) exhibit differences in grain size and shape as well as the distribution of the hard phases (Figure 8). In Figure 8 d) the dendritic structure of the cast alloy can be seen. Figure 9 shows the different hard phases within the alloys. The PT10-004 cup had coarse mixed percolated phases on the grain boundaries and compact hard phases within the grains. In contrast, the PT10-004 head showed lamellar arrangements of carbides within the grains and on the grain boundaries. The micrograph from PT09-238 cup exhibited mixed percolated phases on the grain boundaries and coarse mixed hard phases within the grains. However, PT09-238 head showed fine mixed percolated phases and arrangements of fine hard phases at the grain boundaries as well as within the grains.

4.3 Nano-indentation

In order to receive information concerning the mechanical properties of the different phases nano-indentation tests have been conducted.

Figure 10 shows AFM-scans of indents in mixed hard phases (type I) within hip 017. The small size of the indents within the hard phases compared to those within the matrix is a sign of the higher hardness of around 12.5 GPa (Table 2) and 7 GPa (Table 20), respectively.

To assign the measured values to the real locations of the indents AFM-scans before and after testing as well as SEM images after the indentation have been done.

The AFM-scan with the click-script (a) shows the desired locations of the indents, whereas the AFM-scan (b) and the SEM-image (c) after the test show the real location of the indents.

Figure 11 and Figure 12 show carbides in PT10-004 head. The hardness of the carbides was measured with 18.95 ± 1.86 GPa (Table 3) and 19.52 ± 0.57 GPa (Table 4), respectively. The matrix on the other hand had a hardness of 6.78 ± 0.11 GPa (Table 20). The SEM images (d) show the typical homogeneous, smooth appearance of the carbides.

The nano-indentation test on mixed percolated phases within the PT10-004 cup (Figure 13; Figure 14) revealed a hardness of 8.04 ± 0.86 GPa (Table 5) and 8.37 ± 0.99 GPa (Table 6), respectively. The hardness of the matrix was 7.24 GPa (Table 20). The SEM images (c; d) revealed the inhomogeneous structure of the mixed percolated phase.

The mixed hard phases (type II) within PT10-004 cup shown in Figure 15 and Figure 16 revealed a hardness of 16.46 ± 0.83 GPa (Table 7) and 17.29 ± 0.66 GPa (Table 8). The Z-contrast images (d) exhibited the very fine molybdenum- and chromium-rich phases within the mixed hard phase.

The PT09-238 cup revealed two types of mixed hard phases. The measurements on type II mixed hard phases shown in Figure 17 and Figure 18 yield a hardness of 17.63 ± 0.82 GPa (Table 9) and 17.0 ± 0.21 GPa (Table 10). The type I mixed hard phases (Figure 19; Figure 20) exhibited a lower hardness of 14.47 ± 1.20 GPa (Table 11) and 11.50 ± 0.78 GPa (Table 12), respectively. The hardness of the matrix was measured with 6.42 ± 0.54 GPa (Table 20).

The nano-indentation on the accumulated hard phases (PT09-238 head) shown in Figure 21 and Figure 22 exhibited a hardness of 21.40 ± 0.80 GPa (Table 13) and 21.30 ± 0.54 GPa (Table 15) for the carbides and 20.81 ± 0.43 GPa (Table 14) and 20.75 ± 1.02 GPa (Table 16), respectively for the intermetallic phases.

The hardness of the mixed percolated phases (Figure 23; Figure 24; Figure 25) within the PT09-238 head was determined as 9.07 ± 0.40 GPa (Table 17), 9.23 ± 0.34 GPa (Table 18) and 9.01 ± 0.45 GPa (Table 19). The matrix exhibited a hardness of 7.46 ± 0.15 GPa (Table 20).

In Figure 26 and Figure 27 overviews of hardness and Young´s modulus of the different phases are given. Thus, the carbides and intermetallic phases were the hardest with around 20 GPa. The hardness of the mixed hard phases varies between approximately 12 - 17 GPa. The mixed percolated phases were just slightly harder than the matrix with around 8.5 GPa and around 7 GPa, respectively.

The indentation test on accumulated hard phases processed with increasing loads was conducted in order to check if the hard phases are crack-prone. In Table 21 the different loads are shown. However, the SEM-image in Figure 28 exhibited no sign of crack formation up to a load of 10 µN.

4.4 TEM-analysis

Different TEM-analyzing methods (EDX, EELS and EFTEM) have been used to investigate grain and phase boundaries in hc CoCrMo wrought alloys as well as hard phases within cobalt base wrought and cast alloys.

4.4.1 Chemical alterations at grain boundaries

Across the grain boundary in the hip 004, an EDX line scan was made (Figure 29 and Figure 30). The diagrams in Figure 31 and Figure 32 have

been made with different measuring rates (points per length). No alteration within the chemical composition at the grain boundary could be observed.

In the BF-image in Figure 33 a grain boundary is highlighted. The ZC-image (Figure 34) indicates the location of the EELS scans. The darker color of grain 1 is noticeable. Figure 35 shows the direction in which the line scan was measured (here from right to left). The curves in the diagrams in Figure 36 rose within grain 1. The carbon spectrum showed enrichment at the grain boundary. The molybdenum diagram revealed no significant results.

The EELS line scan has been repeated at this location (Figure 37) and the measurement direction has been adjusted. Again the diagrams exhibited an increase in the curve within grain 1 (Figure 38) and an enrichment in carbon at the grain boundary.

4.4.2 Chemical composition at hard phases

The BF-image in Figure 39 revealed a chromium- rich and a molybdenum-rich hard phase within the hc wrought alloy (hip 004). An EELS line scan has been conducted across the phase boundary between the two hard phases. In Figure 40 a high degree of contamination was observed which was presumably caused by the electron beam. The arrow indicated the desired location and direction of the scan. However, due to sample drift the measured results (Figure 41) were not evaluable.

An EDX mapping has been made at the molybdenum rich phase surrounded by the matrix (Figure 42). The EDX mappings in Figure 43 clearly showed enrichment in molybdenum within the hard phase as well as the cobalt depletion. The chromium content on the other hand showed no alteration. By means of the extracted line scans (Figure 44 and Figure 45) from the EDX mapping, an increase in silicon could be determined within the molybdenum rich hard phase.

Figure 46 shows a BF-image of a carbide located between two grains. Figure 47 shows the location and direction of the progressed EDX line scans. In terms of trying to minimize the sample drift one scan was made without the EDX-aperture. This line scan (Figure 48) exhibited a high influence of the surrounding. The next EDX scan, measured with the EDX aperture, showed no visible influence of the surroundings. The diagram (Figure 49) exhibited the typical enrichment in chromium and depletion in cobalt within the carbide.

At the same location an EELS line scan was made. Figure 50 shows a carbide indicated by the increased chromium content. The EELS line scans (Figure 51) exhibited the same run of the cobalt and chromium curve like shown in the EDX scan. The carbon curve exhibited a distinct enrichment in carbon at the phase boundary and increased carbon content within the carbide.

In Figure 52 another location off an EELS measurement across a phase boundary is shown. The carbide visible in the ZC-image in Figure 53 indicated an increase of the chromium and carbon content due to the darker contrast. In Figure 54 the exact location and direction of the EELS scan are indicated. The diagrams in Figure 55 showed the typical run of the chromium and cobalt curve. The carbon content increased within the carbide. The combined diagram clarified that the results had no qualitative informative value.

Further EELS scans were made on the phase boundary (Figure 56) across a decreased measured length compared with the previous scan. Again decreased cobalt and increased chromium content within the carbide could be shown. However, the carbon curve exhibited an unusual enrichment of carbon within the matrix (Figure 57).

Figure 58 shows a carbide within a hc wrought alloy. From the area marked with the rectangle an EDX mapping was made (Figure 59). The cobalt and chromium mappings showed mostly a distinct transition from

carbide to matrix, on the left side however the transition is blurry. In the molybdenum map a small part of a molybdenum rich phase was visible. This phase also exhibited an enrichment of silicon. The diffraction pattern (Figure 60) showed that the carbide is of the type M_7C_3.

In Figure 61 the sampling location for a FIB lamella across an arrangement of hard phases within hc cast alloy (PT09-238) is shown. Figure 62 showed the thinned FIB lamella. The ZC-image exhibited an accumulation of hard phases with different chemical composition. The EDX mappings in Figure 65 revealed chromium rich and molybdenum rich hard phases. The molybdenum rich phases also exhibited enrichment of silicon. The chromium rich hard phase has been determined as $Cr_{23}C_6$ carbide according to the analysis of the electron diffraction pattern in Figure 63. The diffraction pattern (Figure 64) taken from the molybdenum rich hard phase supported the presence of σ-phase lattice. In order to receive more information concerning the distribution from element of lower order EFTEM mappings have been made. Concerning the cobalt chromium and molybdenum distribution the results correlate with the EDX mapping. The carbon enriched region matched those of the $Cr_{23}C_6$ carbide. The silicon enriched regions, however fit with the molybdenum rich phase.

5. Discussion

The micrographs of the hc wrought alloys (PT09-285 and PT10-117) in Figure 4 uncommonly exhibited a homogeneous microstructure for the cup and a banded for the head, respectively. Usually it is the other way round because the raw material of the head undergoes more forming processes due to the smaller diameter.

The SEM images of the sample PT09-285 (Figure 5) exhibited pits along the grain boundaries. These have been generated during the preparation due to the removal of intermetallic phases. However, the micrographs of the PT10-117 sample showed intermetallic phases on the grain boundaries. In contrast to sample PT09-285, PT10-117 has been polished and etched very carefully. The removal due to the preparation indicates low coherency of the interfaces between matrix and intermetallic phases.

Even though all retrievals were from the same manufacturer, each one exhibited differences in its microstructure and hard phases (Figure 8; Figure 9). The same patterns have been observed within hip replacements of other manufacturers [14]. This can be seen as a result of the fact that heat treatments for cobalt-based alloys are not standardized and stipulated. ASTM standard only concerns the chemical composition and the mechanical properties, but not the microstructure.

The results of the nano-indentation tests on hard phases revealed a high hardness of ~20 GPa for the carbides and intermetallic phases, whereas the mixed percolated phase was just slightly harder than the matrix with approx. 8.5 GPa and 7 GPa, respectively (Figure 26). The hardness of the mixed hard phases on the other hand was between approx. 17 GPa and 12.5 GPa. Considering the SEM images (c+d) of the mixed hard phases within PT09-238 cup (Figure 17 - Figure 20) a relation between the structure and the hardness of the phases can be seen. The hard phase in Figure 17 appeared perforated but showed no different phases and

revealed a hardness of 17.63 ± 0.82 GPa (Table 9). In Figure 18 the mixed hard phase exhibited partly different phases as well as a perforated structure with smaller holes around the phase mixtures. The hardness was measured with 17.0 ± 0.21 GPa (Table 10). The mixed hard phase in Figure 19 had a pitted structure with some bigger holes. The Z-contrast image (d) exhibited the nano-sized different phases. The hard phase in Figure 20 appeared even more pitted and exhibited nano-sized grains of different chemical compositions. This one had the lowest hardness of the mixed hard phases with 11.50 ± 0.78 GPa (Table 12). The lower hardness of mixed hard phases may be related to the larger amount of interfaces within one phase.

Grain boundary analysis using EDX showed no accurate results. This can be explained due to the disability of EDX to detect elements of low atomic number as much as the lower resolution compared with EELS. EDX scans also need more time, thus negative effects like sample drift and contamination have more influence on the results.

EDX mappings across hard phases on the other hand showed good results. It was noticeable that the molybdenum-rich phases came along with enrichments in silicon (Figure 7; Figure 43; Figure 59; Figure 65). This confirms the results of the electron diffraction pattern analysis since it is known from steel that silicon stabilizes the σ-phase. Further it is known that the σ-phase is brittle, which may have negative influence on the mechanical properties and tribological behavior of the alloy.

The enrichment in carbon at phase and grain boundaries detected with EELS line scans (Figure 51; Figure 36; Figure 38) indicates carbon diffusion toward the interfaces.

The enrichment in carbon within the matrix visible in Figure 57 can possibly be caused due to carbon enrichments within dislocations at the phase boundary.

The ZC-image in Figure 34 indicates differences within the chemical composition of two grains according to its contrast. However, the EELS scans (Figure 36; Figure 38) exhibited no results to affirm that assumption, though the curves show an increase in intensity within grain 1. Thus, it is more likely that this effect is thicknesses related.

EDX and EFTEM mappings in Figure 65 and Figure 66 respectively, revealed different hard phases within the hc cast alloy. The EFTEM carbon map showed that only chromium-rich phases exhibited carbon enrichments. Thus, the molybdenum-rich phase cannot be assessed as carbide. Electron diffraction pattern suggest the presence of σ-phase. Although the electron diffraction pattern analysis (Figure 64) was not 100% conclusive, the results must be accurate considering the observed silicon enrichment and the lack of carbon.

6. Summary and conclusion

Within cast CoCrMo alloys hard phases of different sizes, structures and chemical compositions were found. The nano-indentation tests showed that mixed percolated phases were just slightly harder than the matrix with approx. 8.5 GPa and 7 GPa, respectively. The hardness of mixed hard phases, on the other hand varied between around 12-17 GPa depending on its structure. Carbides and single intermetallic phases exhibited the highest hardness of around 20 GPa. However, crack formation was not observed up to an induced load of 10 µN.

The compact hard phase within hc wrought alloy was clearly identified as M_7C_3 carbide. The lamellar arrangement of hard phases within cast alloy exhibited $M_{23}C_6$ carbide and molybdenum-rich intermetallic phase. The intermetallic phase exhibited silicon enrichment and a lack of carbon. The electron diffraction pattern analysis was not 100% conclusive, but supports the presence of σ-phase lattice.

The TEM-analysis showed that EDX was not sufficient for grain boundary investigation. With EELS, on the other hand, carbon enrichment on grain boundaries could be detected. It is to say that EELS is more sufficient with rather low measuring time in order to minimize drifting and to avoid beam induced contamination.

7. Tables

Table 1 - Material

sample name	alloy	manu-facturer	model	time in-situ	type
hip 004	wrought	DePuy	ULTIMA	5 million cycles	simulator tested
hip 017	cast	DePuy	ASR	nA	retrieval
PT09-238	cast	DePuy	ASR XL	41 month	retrieval
PT09-285	wrought	DePuy	ULTAMET XL	13 month	retrieval
PT10-004	cast	DePuy	ASR XL	46 month	retrieval
PT10-117	wrought	DePuy	ULTAMET XL	79 month	retrieval

Table 2 – Nano-indentation results to Figure 10

hip 017 head				
mixed hard phase	Young´s modulus Er [GPa]		hardness H [GPa]	
	mean	standard deviation	mean	standard deviation
a)	234.00	11.08	12.97	1.14
b)	231.22	5.02	12.61	0.50
c)	228.83	10.21	13.34	0.93
d)	227.60	6.48	12.65	0.67
e)	224.34	6.48	12.25	0.71

Table 3 – Nano-indentation results to Figure 11

carbide (PT10-004 head)		
data point	Young´s modulus Er [GPa]	hardness H [GPa]
0	256.16	18.94
1	267.06	20.81
2	259.90	18.94
3	264.41	19.94
4	233.30	16.09
5	269.57	20.99
6	255.82	16.93
mean	258.03	18.95
standard deviation	12.10	1.86

Table 4 – Nano-indentation results to Figure 12

carbide (PT10-004 head)		
data point	Young´s modulus Er [GPa]	hardness H [GPa]
2	252.20	18.78
3	254.95	20.28
5	255.53	19.86
6	266.92	19.33
7	249.73	19.32
mean	255.87	19.52
standard deviation	6.60	0.57

Table 5 – Nano-indentation results to Figure 13

mixed percolated phase (PT10-004 cup)		
data point	Young´s modulus Er [GPa]	hardness H [GPa]
0	215.31	9.09
1	213.92	8.80
2	228.90	9.95
3	190.40	7.55
4	203.39	7.34
5	185.47	6.91
6	193.15	7.74
7	197.47	7.58
8	206.60	8.21
9	207.08	7.31
10	189.82	7.65
11	217.53	9.09
12	180.56	7.56
13	171.23	7.81
mean	200.06	8.04
standard deviation	16.03	0.86

Table 6 - Nano-indentation results to Figure 14

mixed percolated phase (PT10-004 cup)		
data point	Young´s modulus Er [GPa]	hardness H [GPa]
0	207.67	7.70
1	212.12	8.39
2	227.14	9.01
3	199.67	7.65
4	194.80	6.97
5	201.72	7.95
6	200.64	8.07
7	206.68	7.98
8	211.94	9.07
9	206.26	7.76
10	231.92	9.89
11	209.02	7.87
12	208.45	7.47
13	220.53	10.62
18	221.55	9.17
mean	210.67	8.37
standard deviation	10.51	0.99

Table 7 - Nano-indentation results to Figure 15

mixed hard phase (PT10-004 cup)		
data point	Young´s modulus Er [GPa]	hardness H [GPa]
0	271.48	17.37
4	257.48	15.20
5	264.13	16.93
6	267.12	16.59
10	256.44	16.19
mean	263.33	16.46
standard deviation	6.39	0.83

Table 8 - Nano-indentation results to Figure 16

mixed hard phase (PT10-004 cup)		
data point	Young´s modulus Er [GPa]	hardness H [GPa]
1	260.70	17.03
6	270.95	17.71
7	257.18	16.49
8	265.40	17.93
mean	263.56	17.29
standard deviation	5.97	0.66

Table 9 - Nano-indentation results to Figure 17

mixed hard phase (PT09-238 cup)		
data point	Young´s modulus Er [GPa]	hardness H [GPa]
1	204.60	18.22
2	200.38	16.73
3	202.62	17.88
6	197.51	17.86
7	197.08	18.58
8	195.57	16.53
mean	199.63	17.63
standard deviation	3.51	0.82

Table 10 - Nano-indentation results to Figure 18

mixed hard phase (PT09-238 cup)		
data point	Young´s modulus Er [GPa]	hardness H [GPa]
1	202.89	17.12
4	215.42	16.97
6	210.76	16.72
7	213.56	17.19
mean	210.66	17.00
standard deviation	5.52	0.21

Table 11 - Nano-indentation results to Figure 19

mixed hard phase (PT09-238 cup)		
data point	Young´s modulus Er [GPa]	hardness H [GPa]
0	210.50	15.59
1	210.54	13.92
2	197.69	14.58
3	200.19	13.41
4	210.79	14.74
5	204.85	14.09
6	210.74	16.61
7	206.34	12.50
9	207.52	14.79
mean	206.57	14.47
standard deviation	4.87	1.20

Table 12 - Nano-indentation results to Figure 20

mixed hard phase (PT09-238 cup)		
data point	Young´s modulus Er [GPa]	hardness H [GPa]
0	207.19	12.61
1	197.65	10.54
2	197.66	12.05
3	198.81	11.25
4	202.85	11.54
5	202.29	11.98
6	196.53	12.29
8	186.77	10.27
9	197.56	11.76
10	197.61	12.03
12	194.98	10.27
13	189.31	11.39
mean	197.43	11.50
standard deviation	5.53	0.78

Table 13 - Nano-indentation results to Figure 21

carbide (PT09-238 head)		
data point	Young´s modulus Er [GPa]	hardness H [GPa]
3	280.76	21.43
4	270.33	20.27
7	280.73	21.84
9	273.29	22.05
mean	276.28	21.40
standard deviation	5.30	0.80

Table 14 - Nano-indentation results to Figure 21

intermetallic phase (PT09-238 head)		
data point	Young´s modulus Er [GPa]	hardness H [GPa]
1	274.67	20.86
2	272.99	21.06
6	269.25	20.09
10	278.96	20.51
11	271.97	21.27
13	266.70	21.06
mean	272.42	20.81
standard deviation	4.27	0.43

Table 15 - Nano-indentation results to Figure 22

carbide (PT09-238 head)		
data point	Young´s modulus Er [GPa]	hardness H [GPa]
1	284.88	20.75
2	279.02	21.23
6	271.54	20.76
7	285.56	22.29
9	280.36	21.91
13	266.61	21.22
14	283.52	21.09
15	270.39	21.16
mean	277.74	21.30
standard deviation	7.27	0.54

Table 16 - Nano-indentation results to Figure 22

intermetallic phase (PT09-238 head)		
data point	Young´s modulus Er [GPa]	hardness H [GPa]
0	236.12	18.92
3	273.00	20.46
10	273.51	21.29
12	278.45	20.97
16	284.63	21.93
17	284.20	20.95
mean	271.65	20.75
standard deviation	18.11	1.02

Table 17 - Nano-indentation results to Figure 23

mixed percolated phase (PT09-238 head)		
data point	Young´s modulus Er [GPa]	hardness H [GPa]
4	215.60	9.68
6	224.95	8.70
9	224.23	9.26
10	216.10	8.78
11	225.29	8.94
mean	221.24	9.07
standard deviation	4.93	0.40

Table 18 – Nano-indentation results to Figure 24

mixed percolated phase (PT09-238 cup)		
data point	Young´s modulus Er [GPa]	hardness H [GPa]
1	209.85	9.31
2	226.82	9.27
3	222.65	8.71
8	217.92	9.14
9	226.60	9.17
16	212.49	9.77
mean	219.39	9.23
standard deviation	7.19	0.34

Table 19 - Nano-indentation results to Figure 25

mixed percolated phase (PT09-238 head)		
data point	Young´s modulus Er [GPa]	hardness H [GPa]
4	219.52	9.11
5	215.40	9.41
9	210.47	8.86
10	208.85	9.61
12	229.55	8.24
13	220.91	8.79
14	218.08	8.71
15	225.28	9.38
mean	218.51	9.01
standard deviation	6.99	0.45

Table 20 – Nano-indentation overview matrix

matrix				
sample	Young´s modulus Er [GPa]		hardness H [GPa]	
	mean	standard deviation	mean	standard deviation
hip 17 head	194.70	5.66	7.09	0.32
PT10-004 cup	214.29	18.88	7.24	1.02
PT10-004 head	210.13	3.72	6.78	0.11
PT09-238 head	224.65	6.45	7.46	0.15
PT09-238 cup	168.54	7.07	6.42	0.54

Table 21 – Nano-indentation with increasing load (Figure 28)

accumulated hard phases (PT09-238 head)			
data point	load P_{max} [mN]	Young´s modulus Er [GPa]	hardness H [GPa]
0	4.00	271.46	21.43
1	4.66	276.28	21.22
2	5.33	279.49	21.70
3	6.00	277.18	21.56
4	6.66	282.00	22.19
5	7.33	241.21	11.18
6	8.00	264.06	19.75
7	8.66	282.31	20.99
8	9.33	272.68	20.27
9	10.00	255.42	15.98
mean		218.51	9.01
standard deviation		6.99	0.45

8. Figures

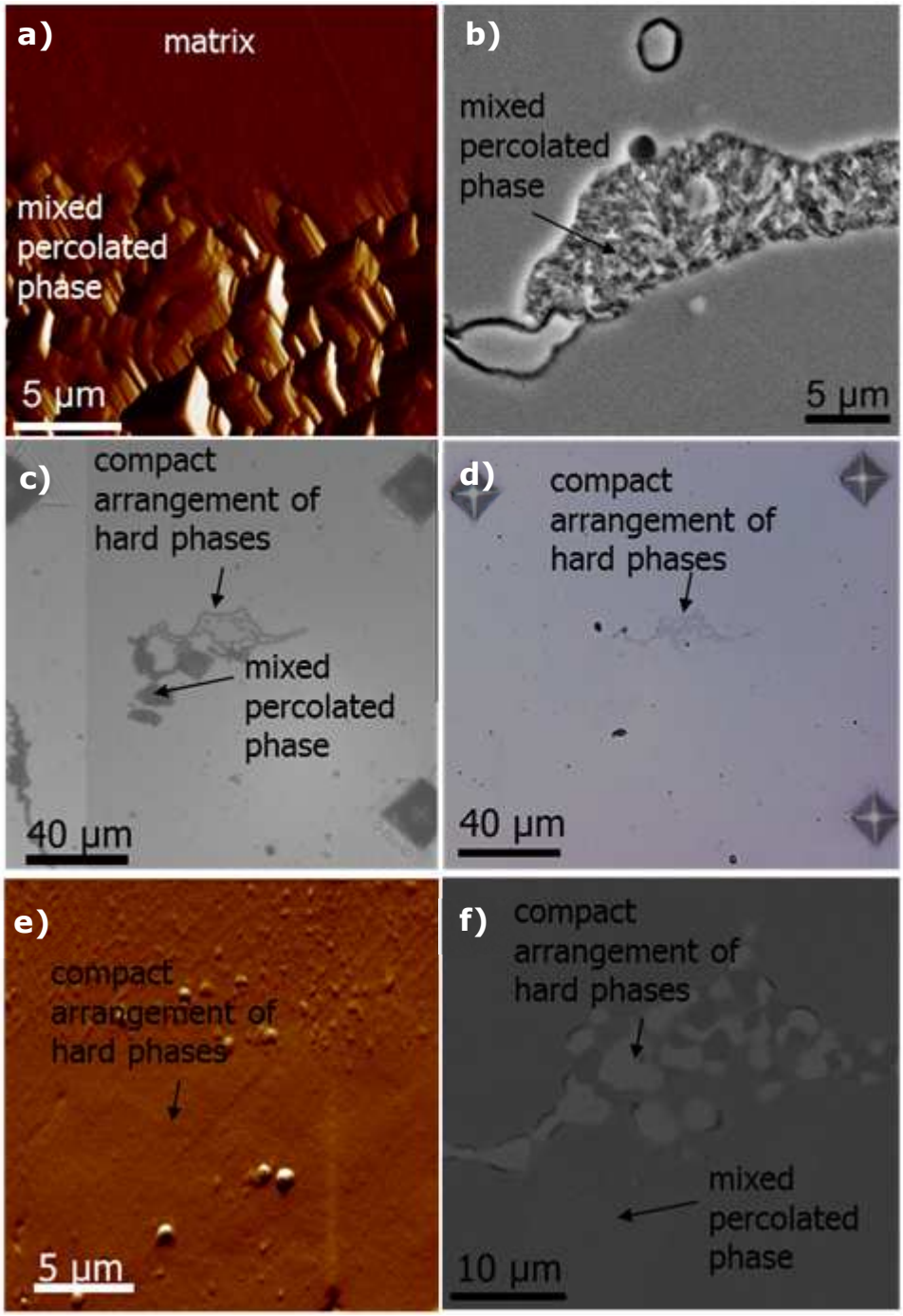

Figure 1 – Nano-indentation preparation
a) AFM scan exhibited rough structure of mixed percolated phase
b) Mixed percolated phase clearly visible on etches sample in SEM
c) Micro-hardness indents mark desired location on etches sample
d) Micro-hardness indents on polished sample, mixed percolated phase hardly visible
e) AFM-scan on polished sample, hard phases hardly visible
f) ZC shows distribution within compact arrangement of hard phases, mixed percolated phase barely visible

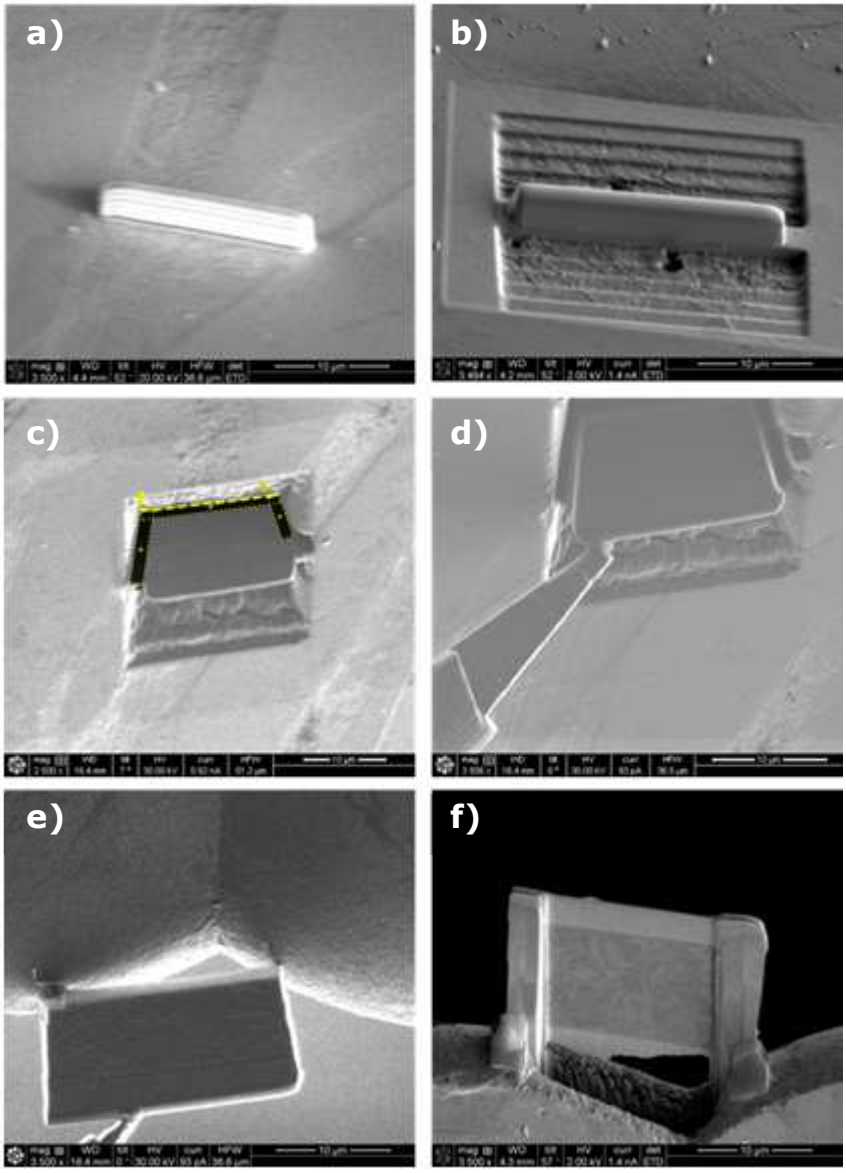

Figure 2 – TEM sample preparation using FIB
a) Pt-depositioning to protect surface from beam damage
b) Removal of surrounding bulk material using focused ion beam
c) Free FIB lamella from bulk due to so called U-cut
d) Lift out with Omniprobe
e) Mounting FIB lamella on TEM grid
f) Thinned FIB lamella

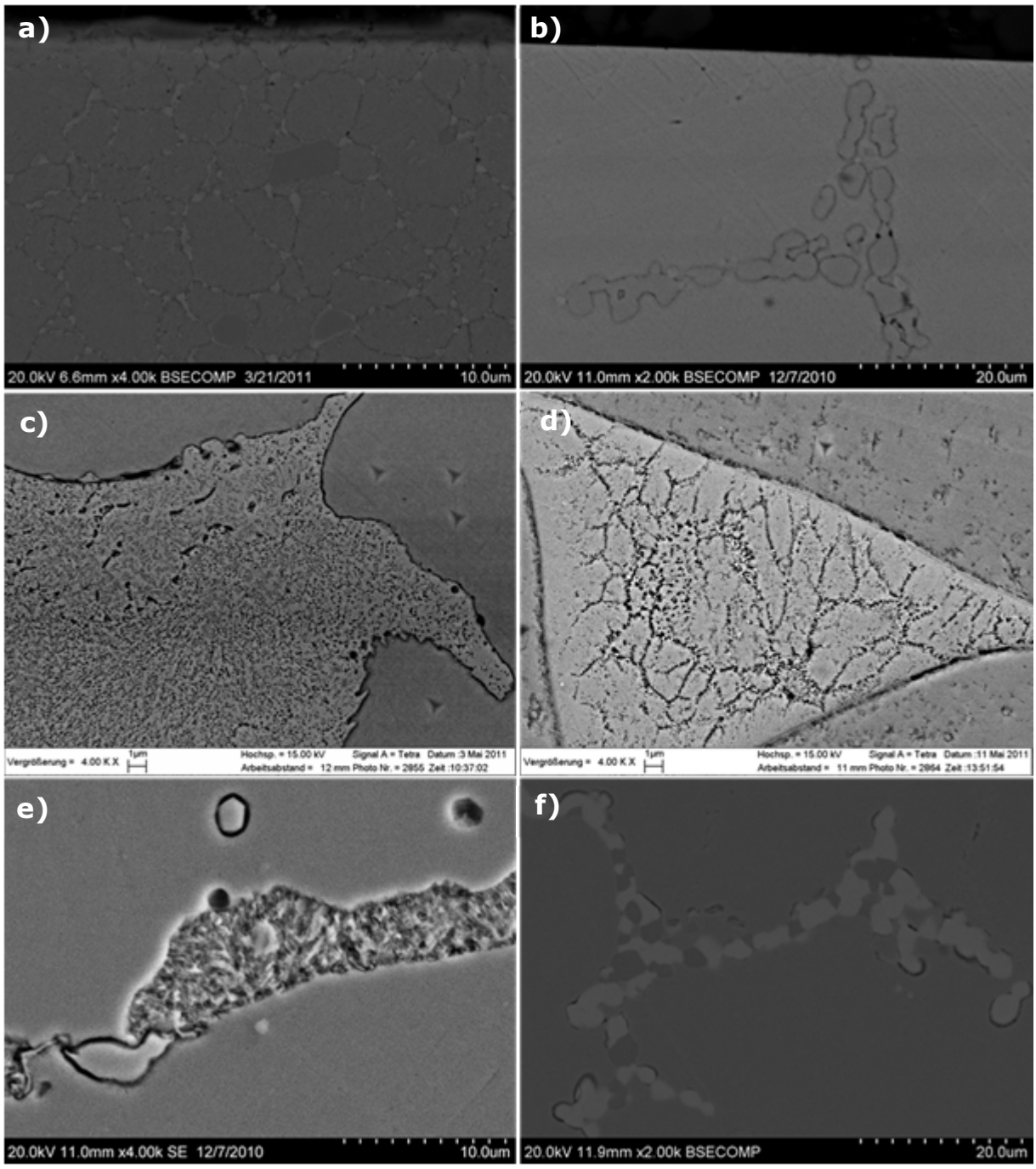

Figure 3 – Different phases in hc cobalt based alloys
a) (wrought alloy) fine and compact carbides and intermetallic phases
b) (cast alloy) fine lamellar carbides
c) + d) (cast alloy) mixed hard phases with different structures
e) (cast alloy) mixed percolated phase (fine carbides and intermetallic phases)
f) (cast alloy) lamellar arrangement of compact hard phases (carbides and intermetallic phases)

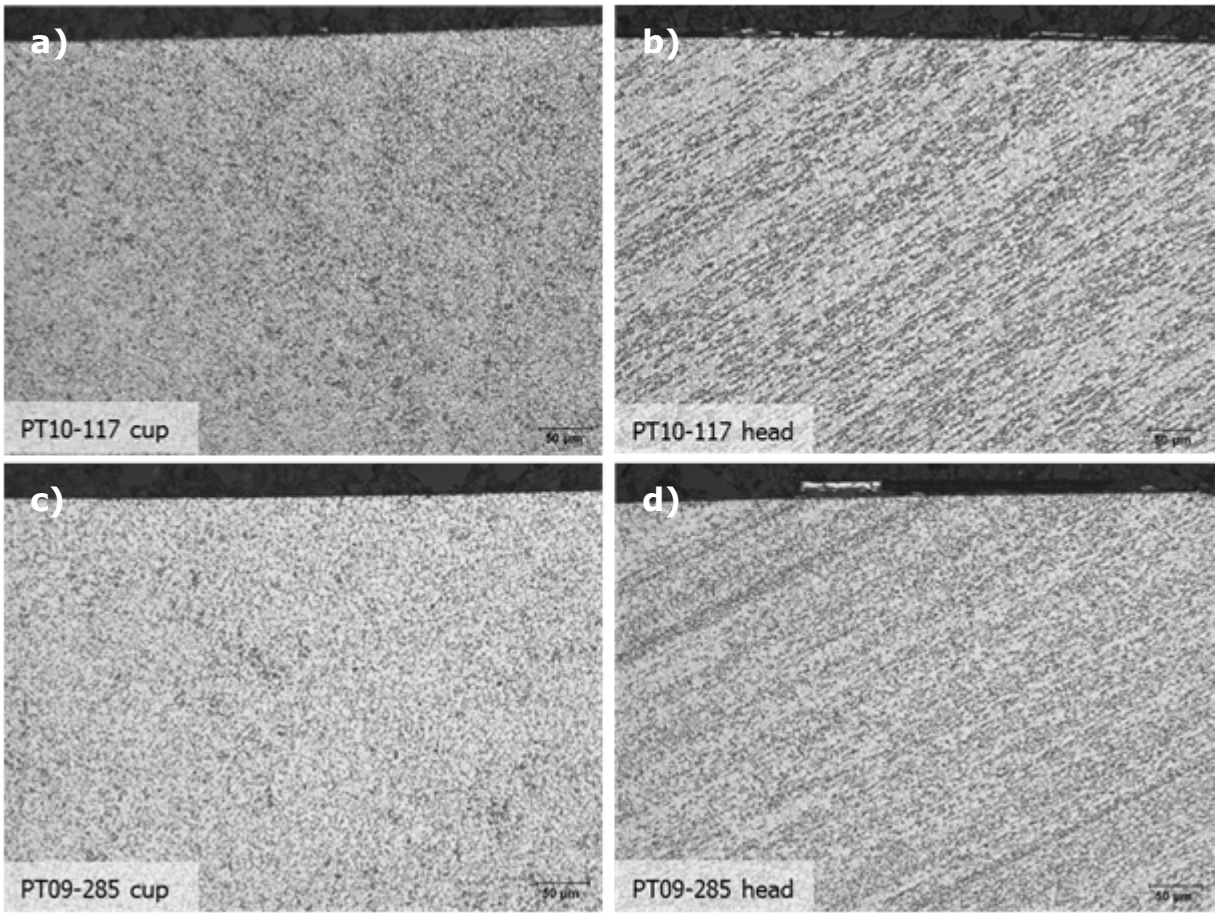

Figure 4 – OM images exhibit microstructure of hc wrought alloys.
a) + c) Cups show homogeneous distribution of hard phases.
b) + d) Heads exhibit inhomogeneous banded structure.

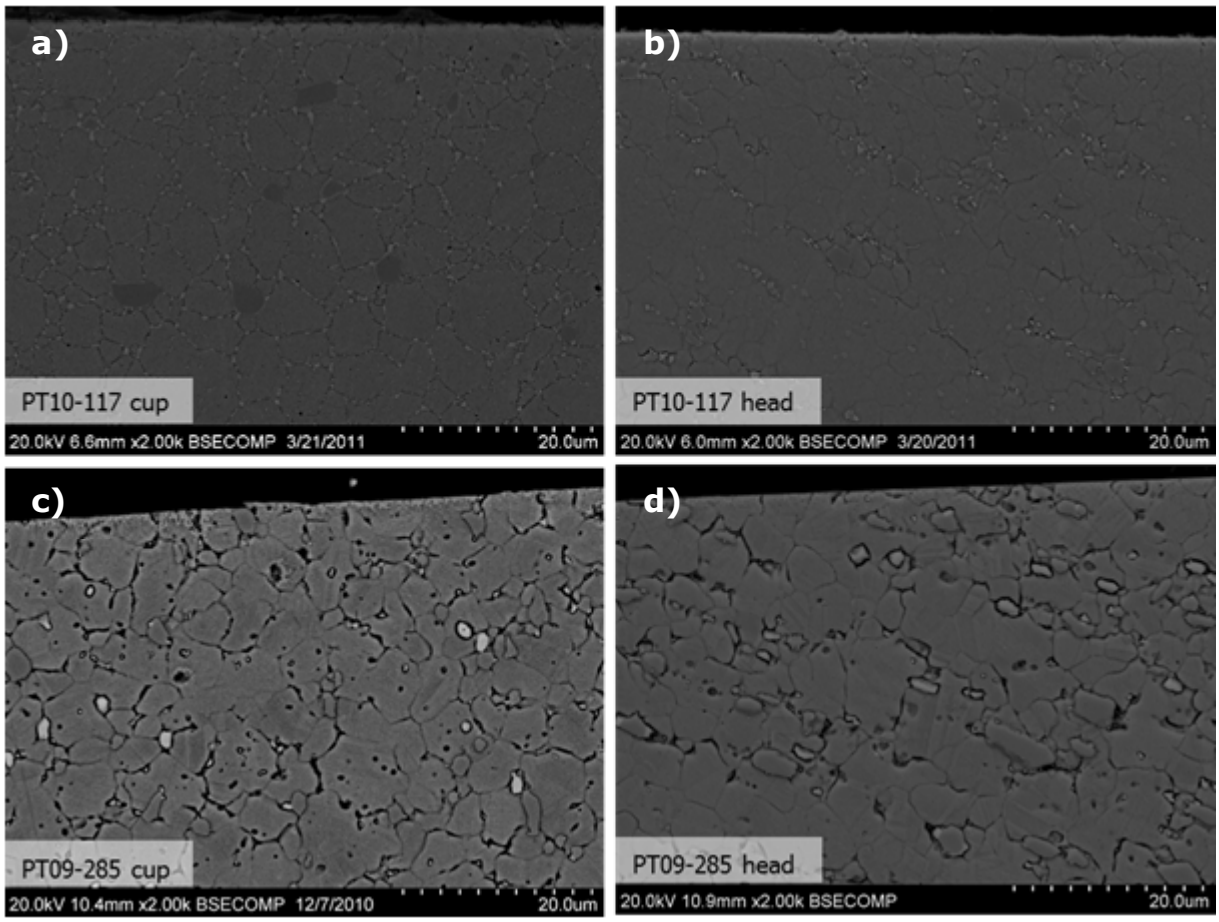

Figure 5 – ZC-images of hc wrought alloys.
a) Intermetallic phases along grain boundaries, homogeneous distribution of carbides.
b) Alteration between hard phase rich and depleted regions, intermetallic phases on grain boundaries.
c) Homogeneous distribution of hard phases, pits due to removal of intermetallic phases during preparation.
d) Banded structure, pits due to removal of intermetallic phases.

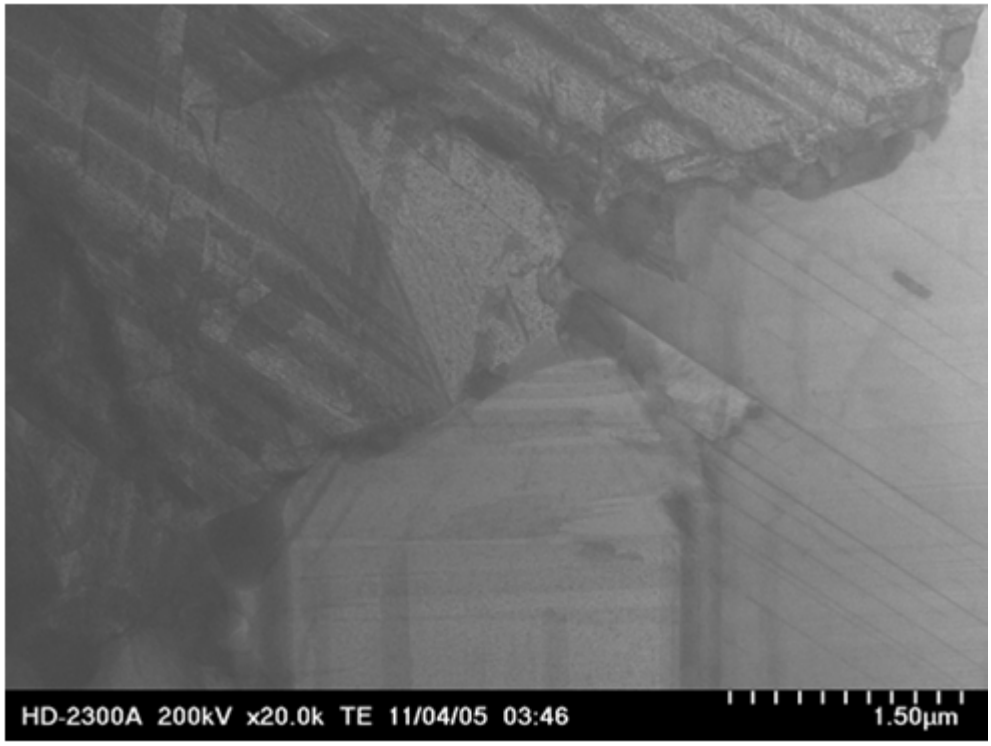

Figure 6 – BF image of hc wrought alloy (PT10-117)

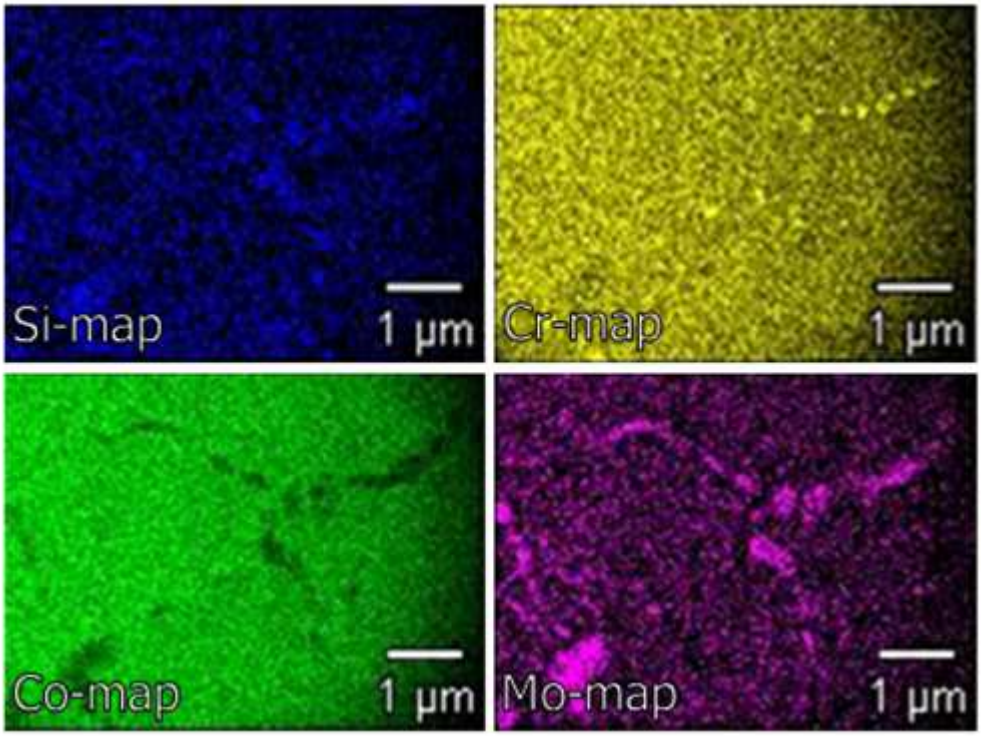

Figure 7 – EDX mapping from Figure 6

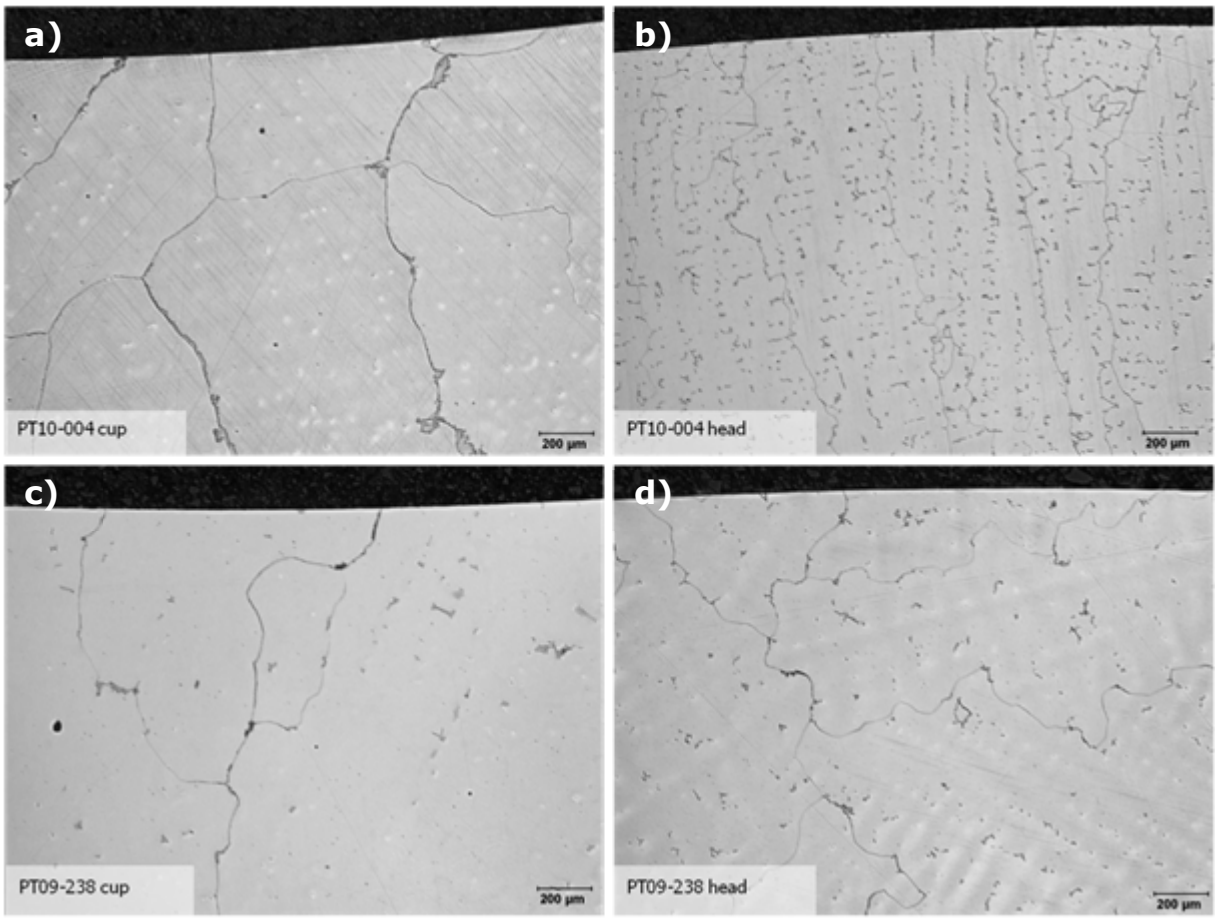

Figure 8 - OM images showing the microstructures of the cast alloys.
a) Globular shaped grains, mixed percolated hard phases on grain boundaries and compact blocky hard phases within the grains.
b) Lamellar shaped grains, accumulations of carbides within grains and on grain boundaries.
c) Very large, globular shaped grains, mixed percolated hard phases on grain boundaries and mixed hard phases within grains.
d) Lamellar shapes grains, mixed percolated hard phases on grain boundaries, accumulations of compact hard phases on grain boundaries and within grains. Grains show dendritic structure.

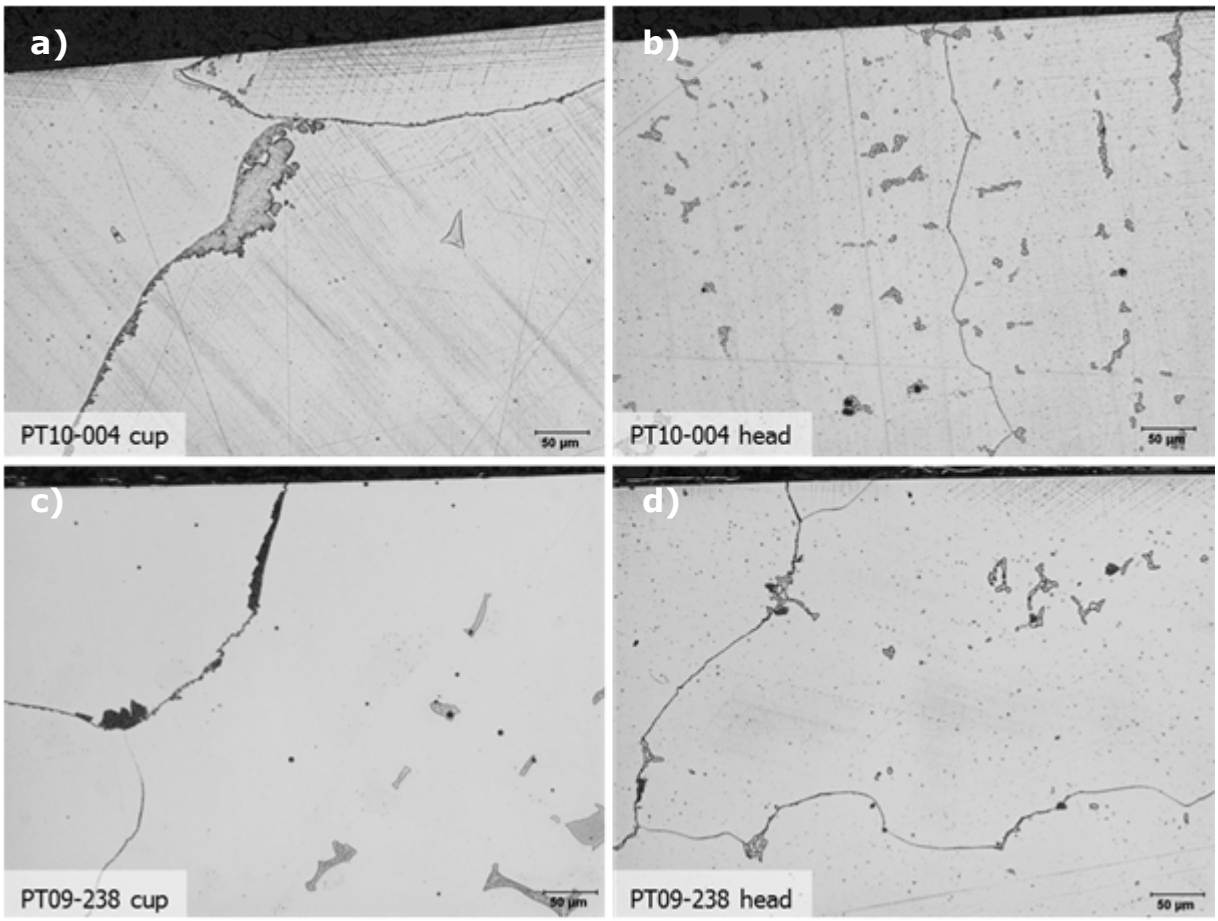

Figure 9 – OM-images exhibiting hard phases within hc cast alloys.
a) Mixed percolated phase on the grain boundaries, compact hard phase within the grains.
b) Carbides on the grain boundaries and within the grains.
c) Mixed percolated phases on the grain boundaries, mixed hard phases within the grains.
d) Mixed percolated phases on the grains boundaries, accumulation of hard phases on the grain boundaries and within the grains.

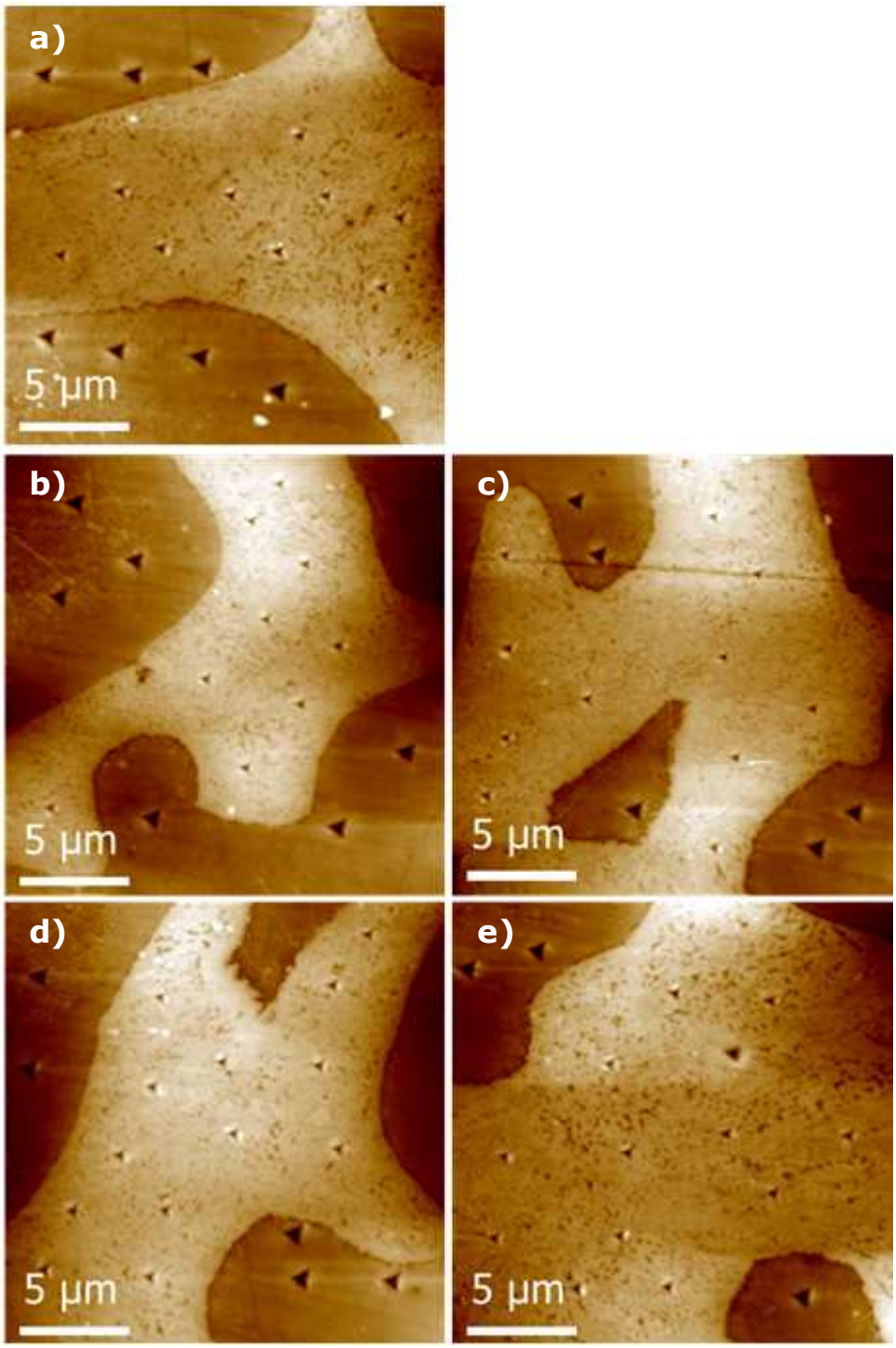

Figure 10 – Nano-indentation on mixed hard phases within hip 017

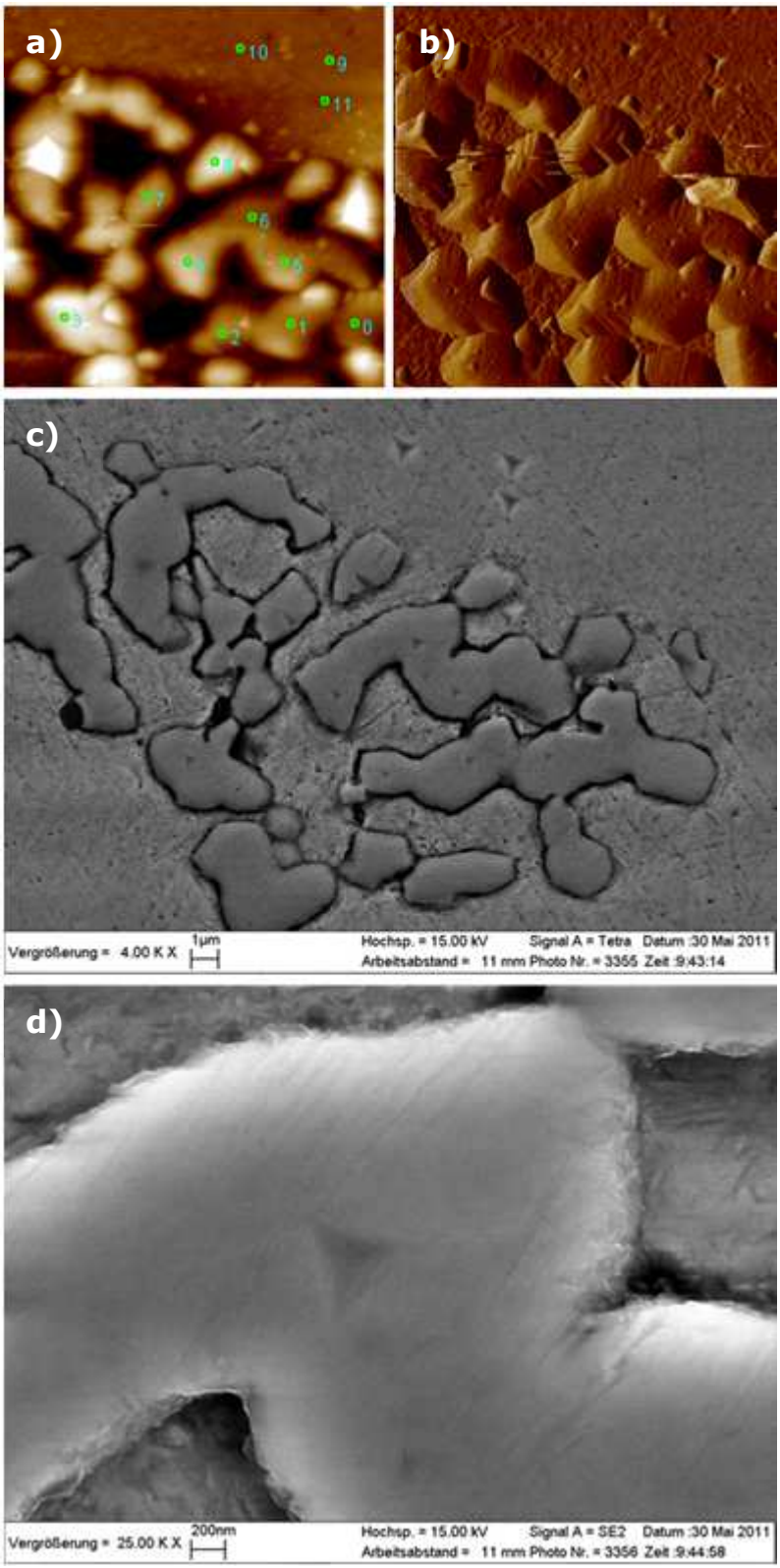

Figure 11 - Nano-indentation on hard phase in sample PT10-004 head
a) AFM scan before indentation with click script
b) AFM scan shows indents after indentation
c) SEM image of measured area
d) Magnified detail of c)

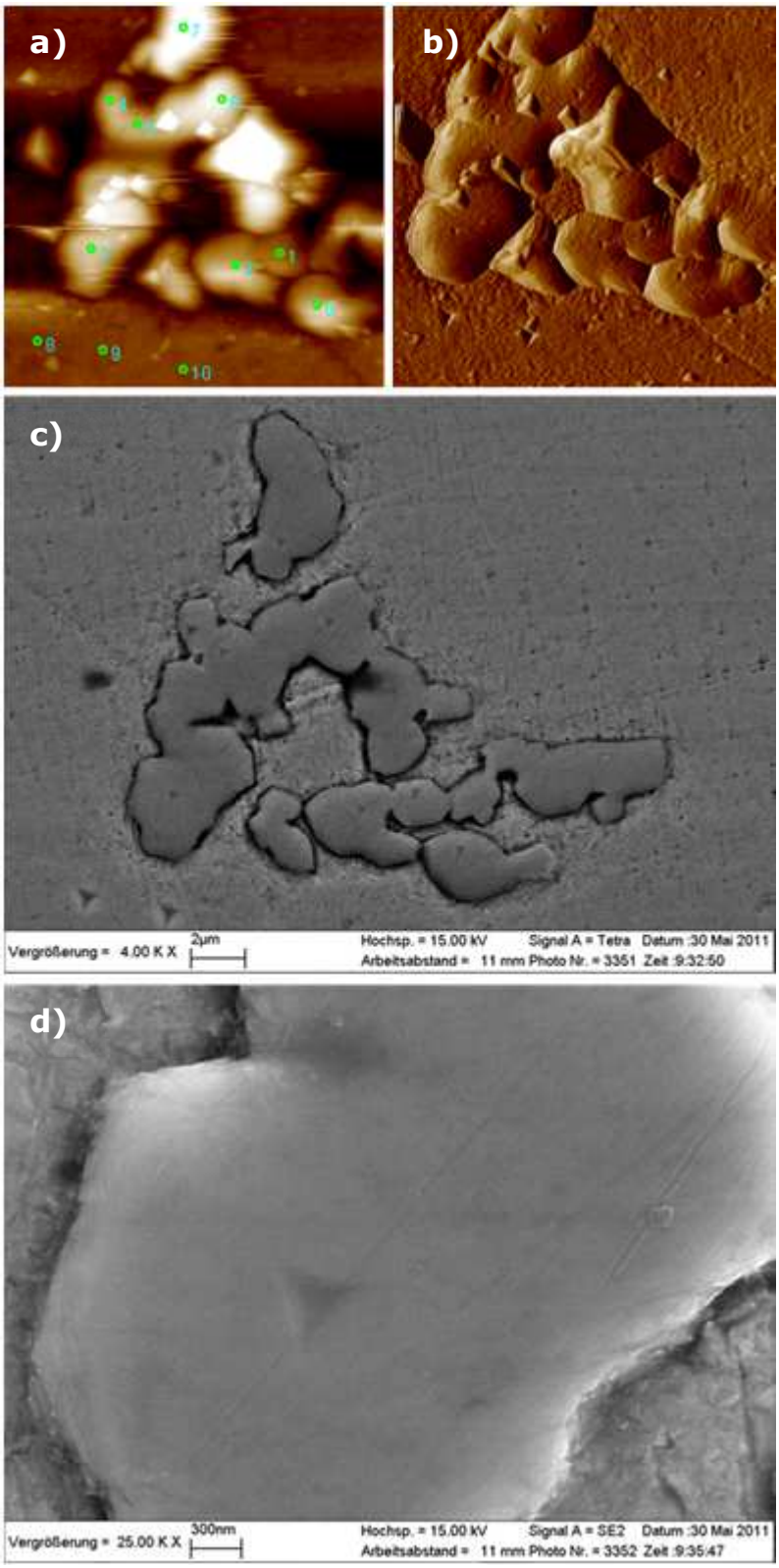

Figure 12 - Nano-indentation on hard phase in sample PT10-004 head
a) AFM scan before indentation with click script
b) AFM scan shows indents after indentation
c) SEM image of measured area
d) Magnified detail of c)

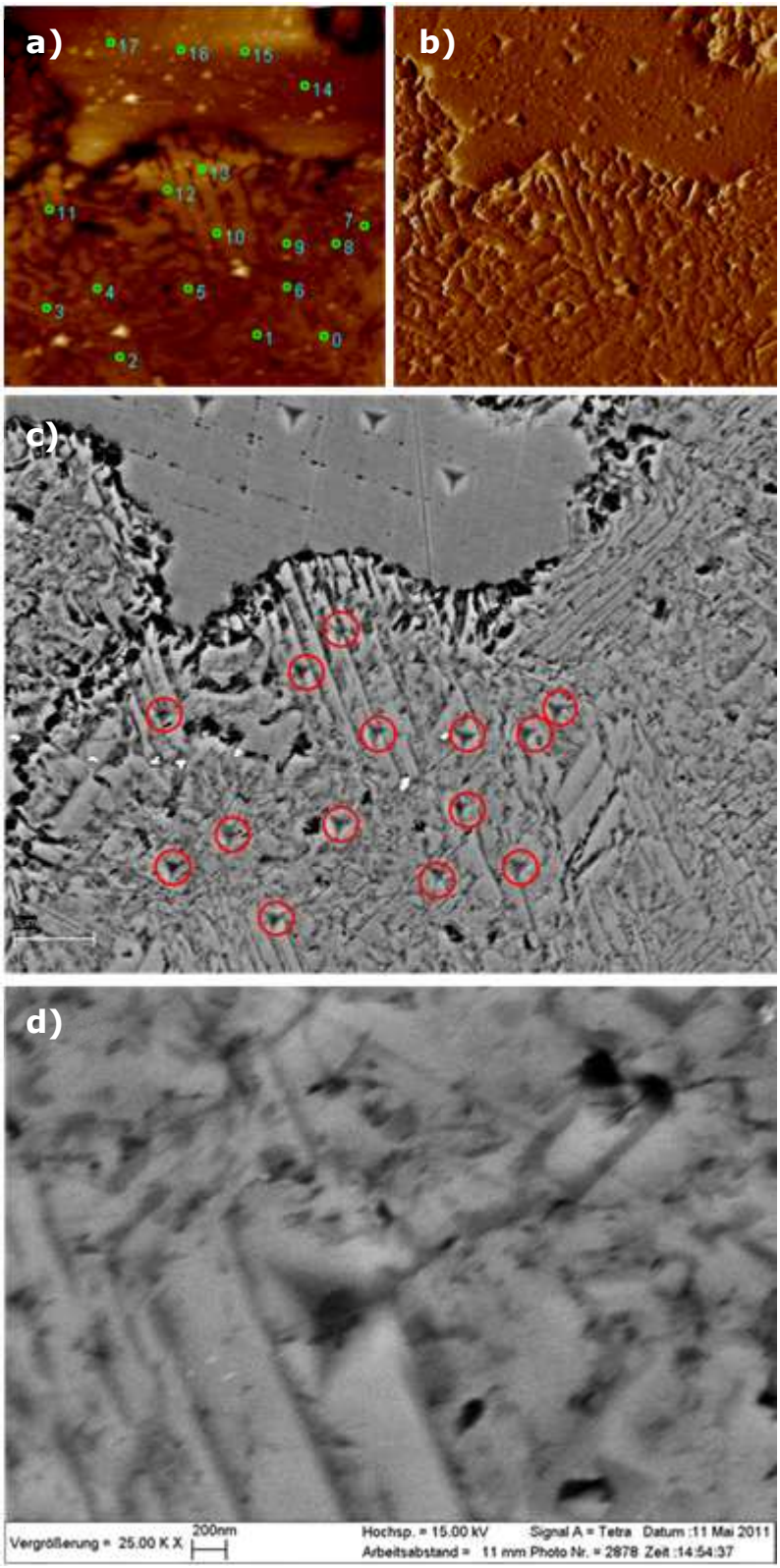

Figure 13 - Nano-indentation on sample PT10-004 cup
a) AFM scan before indentation with click script
b) AFM scan shows indents after indentation
c) SEM image of measured area
d) Magnified detail of c)

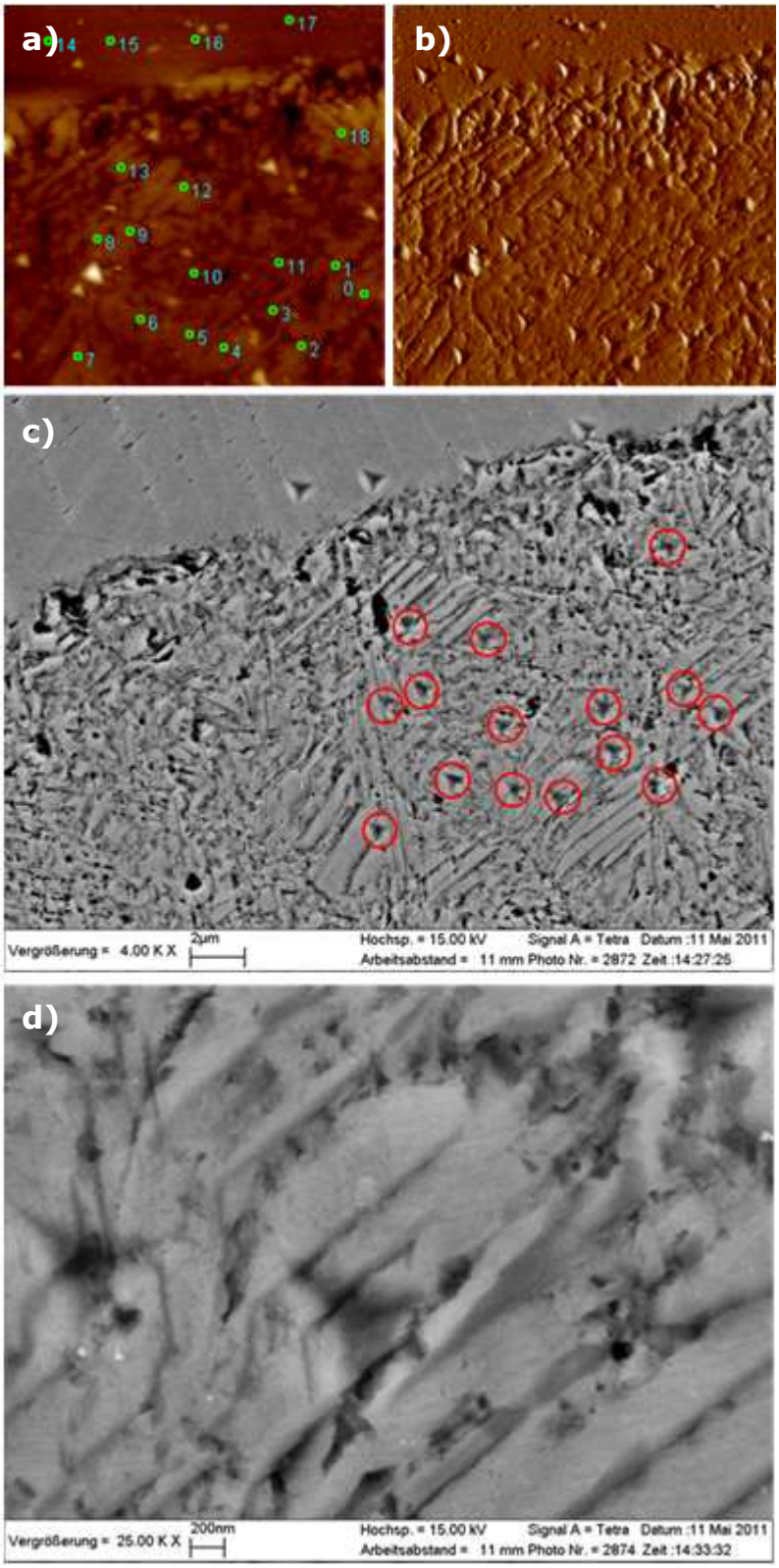

Figure 14 - Nano-indentation on sample PT10-004 cup
a) AFM scan before indentation with click script
b) AFM scan shows indents after indentation
c) SEM image of measured area
d) Magnified detail of c)

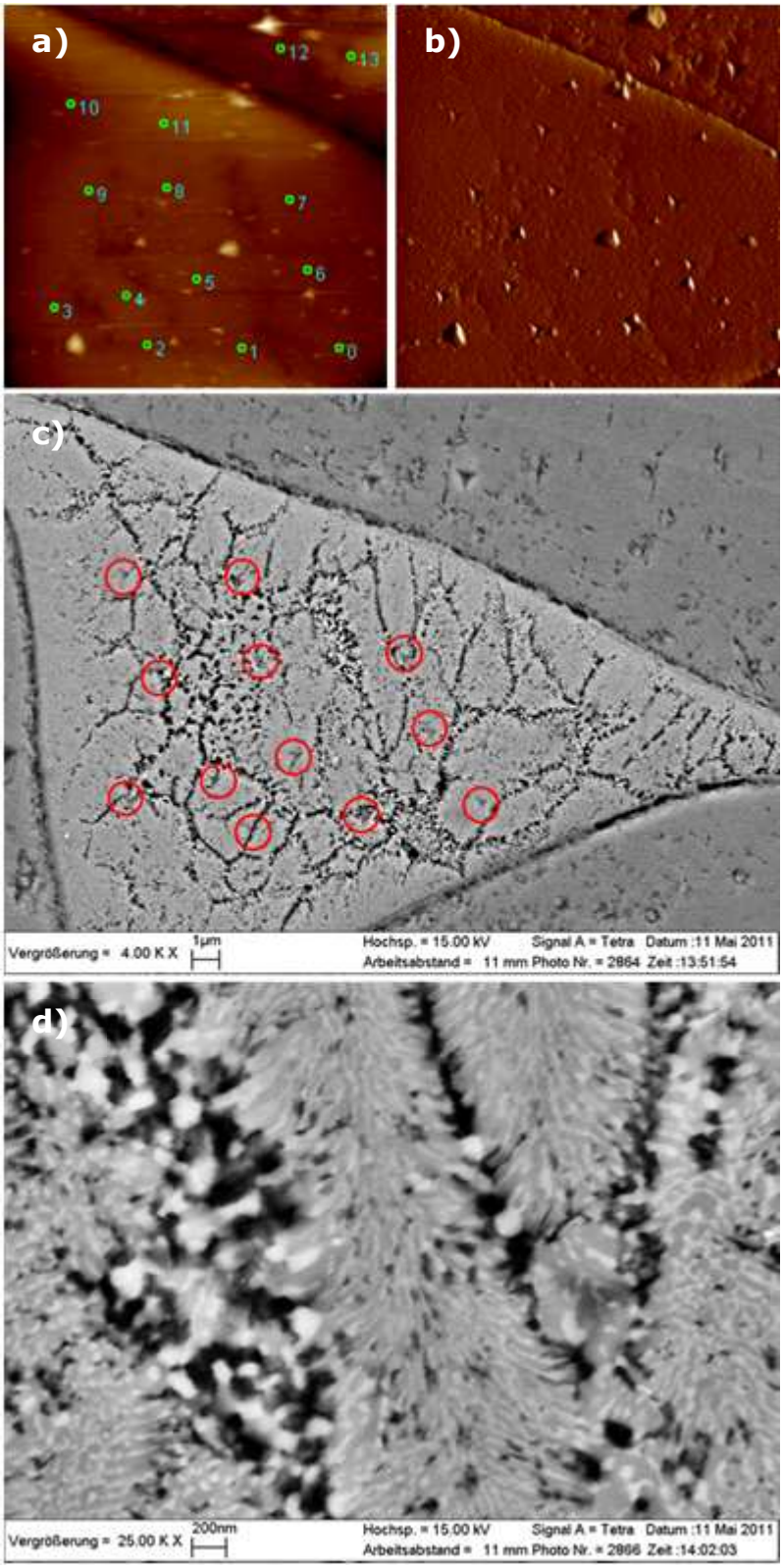

Figure 15 - Nano-indentation on hard phase within PT10-004 cup
a) AFM scan before indentation with click script
b) AFM scan shows indents after indentation
c) SEM image of measured area
d) Magnified detail of c) ZC exhibits mixed phase

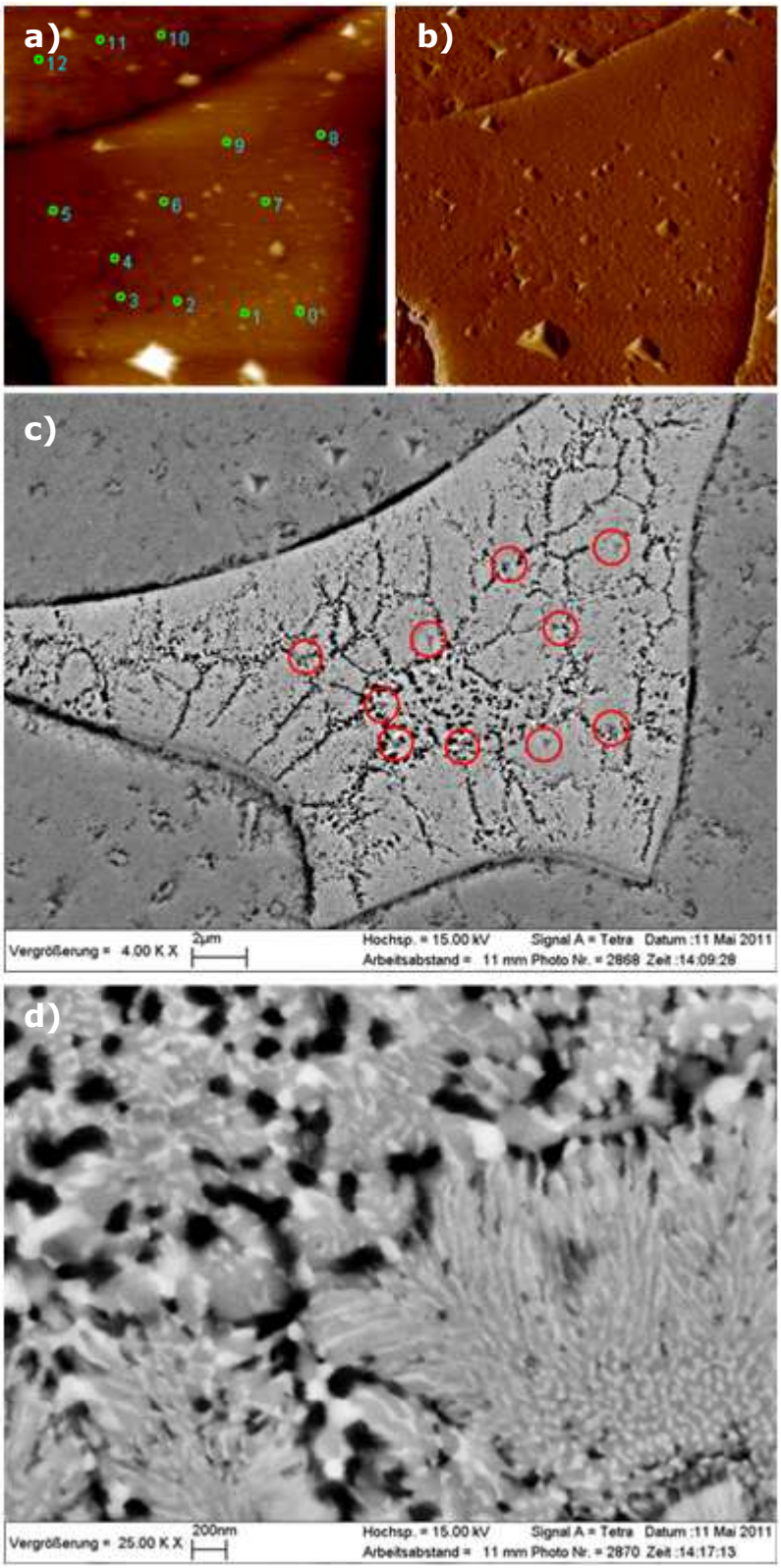

Figure 16 - Nano-indentation on hard phase within PT10-004 cup
a) AFM scan before indentation with click script
b) AFM scan shows indents after indentation
c) SEM image of measured area
d) Magnified detail of c) ZC exhibits mixed phase

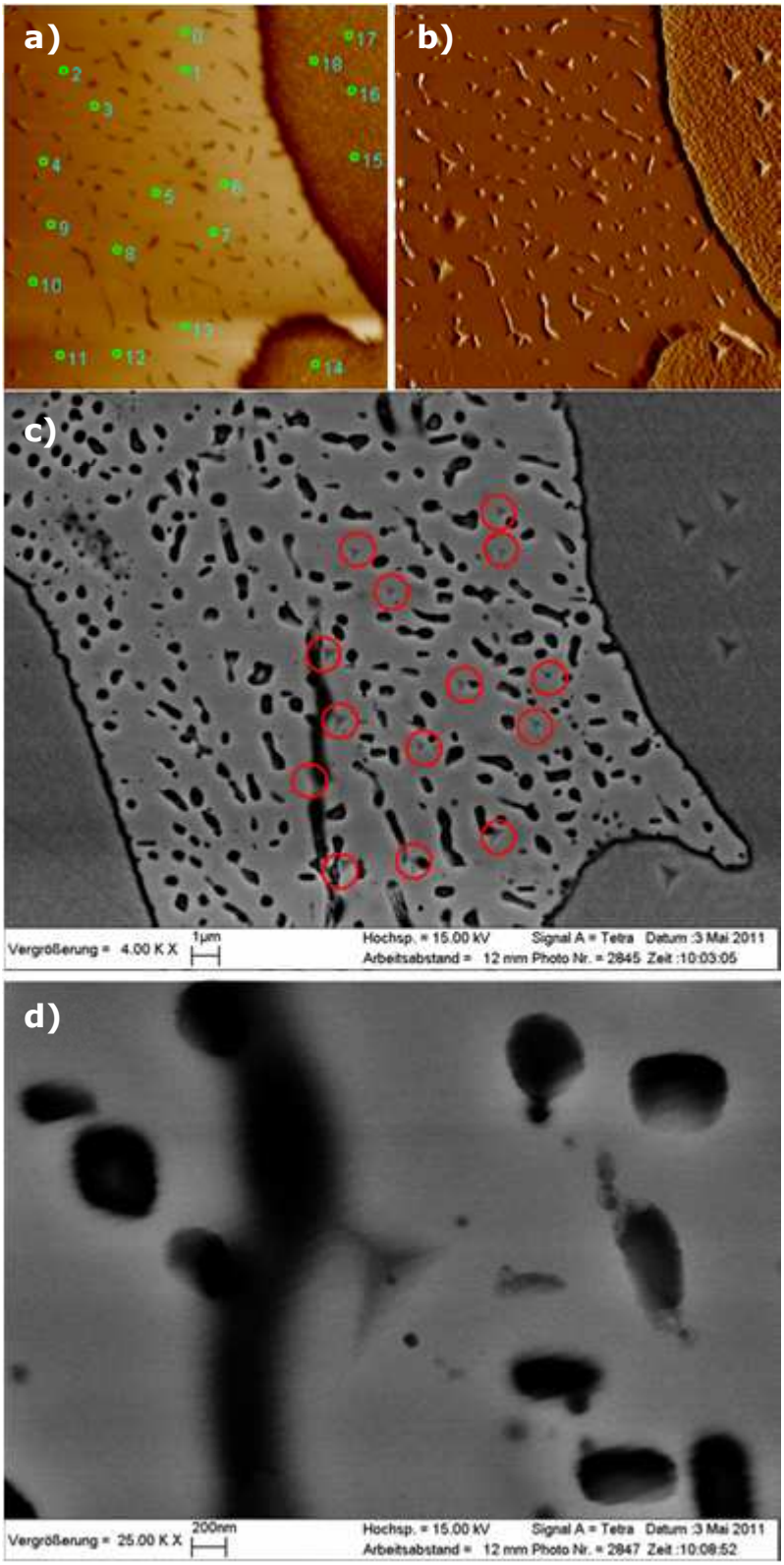

Figure 17 - Nano-indentation on hard phase in PT-238 cup
a) AFM scan before indentation with click script
b) AFM scan shows indents after indentation
c) SEM image of measured area, red circles mark indents
d) Magnified detail of c) exhibits pitted structure

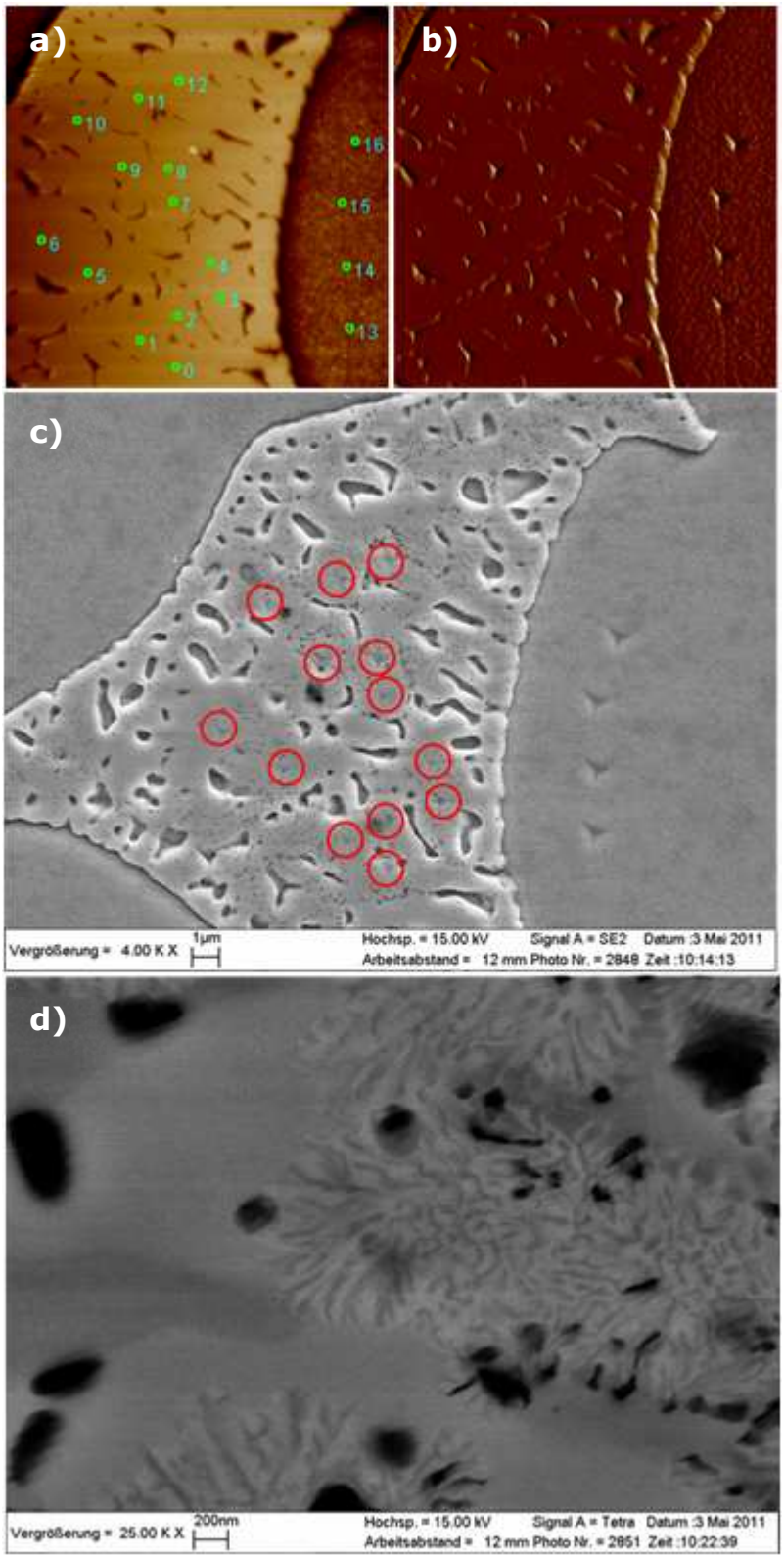

Figure 18 - Nano-indentation on hard phase in sample PT09-238 cup
a) AFM scan before indentation with click script
b) AFM scan shows indents after indentation
c) SEM image of measured area
d) Magnified detail of c) ZC exhibits mixed phase

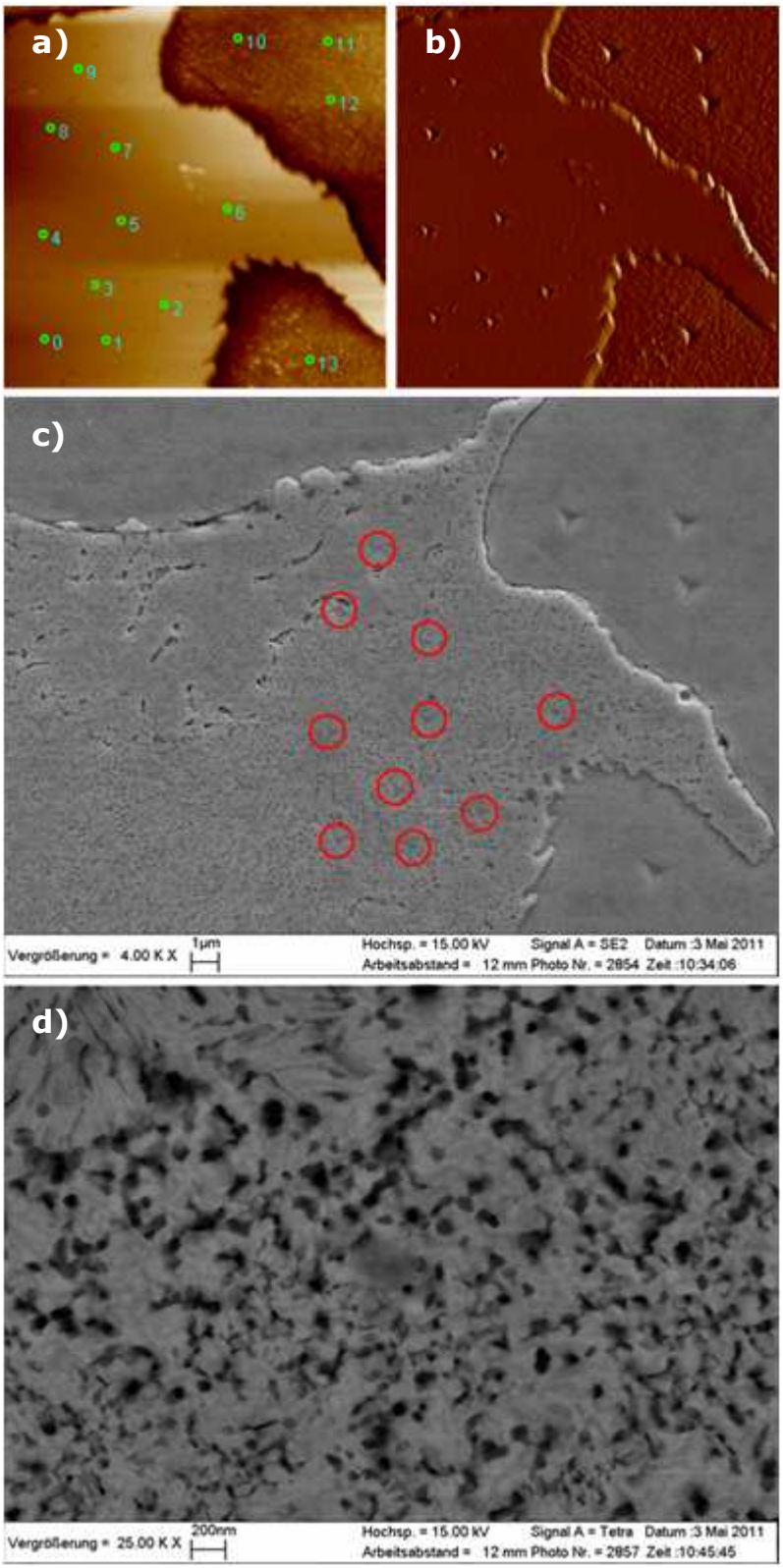

Figure 19 - Nano-indentation on hard phase in sample PT09-238 cup
a) AFM scan before indentation with click script
b) AFM scan shows indents after indentation
c) SEM image of measured area
d) Magnified detail of c) ZC exhibits mixed phase

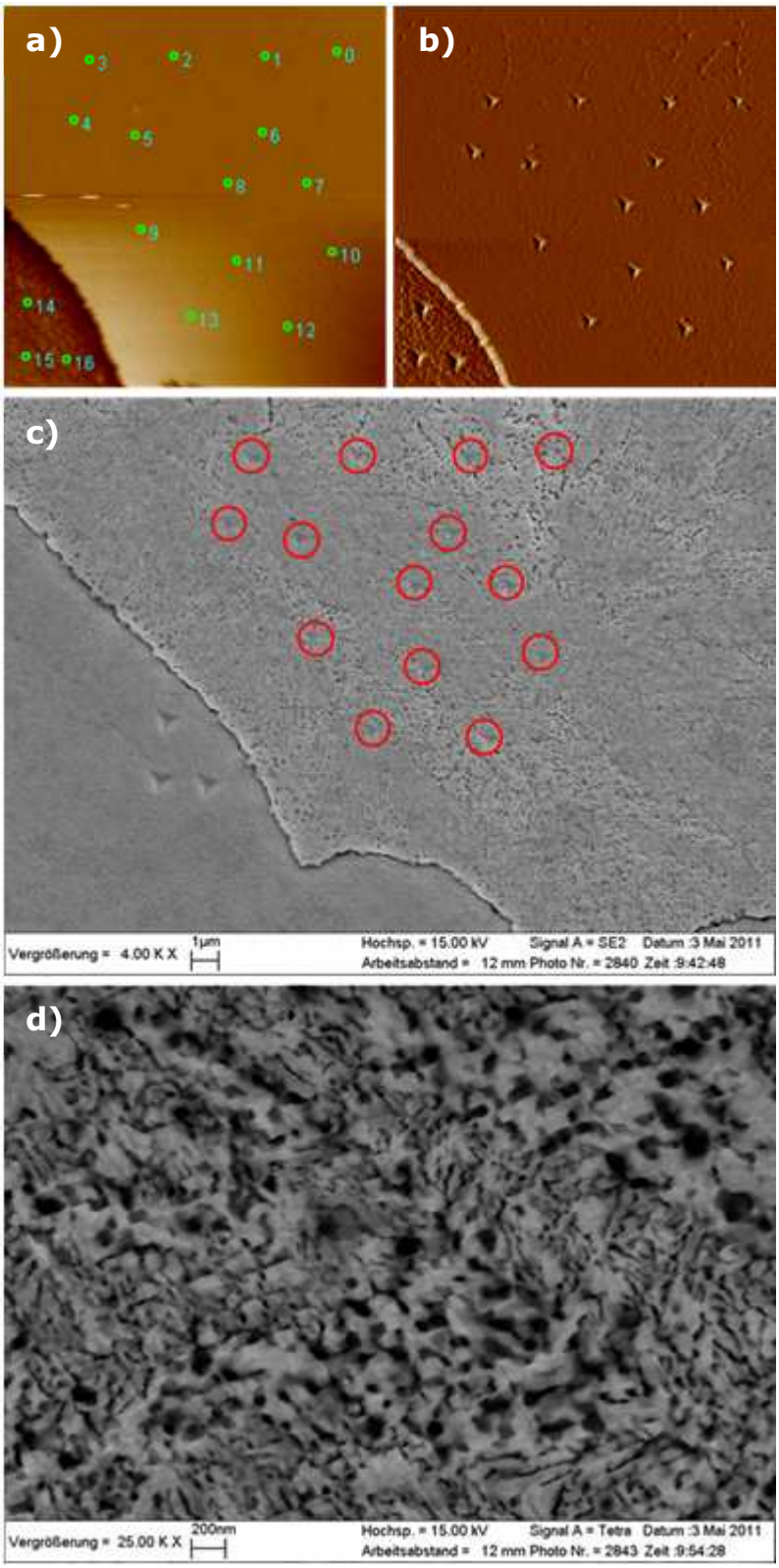

Figure 20 - Nano-indentation on hard phase within PT09-238 cup
a) AFM scan before indentation with click script
b) AFM scan shows indents after indentation
c) SEM image of measured area
d) Magnified detail of c) ZC exhibits mixed phase

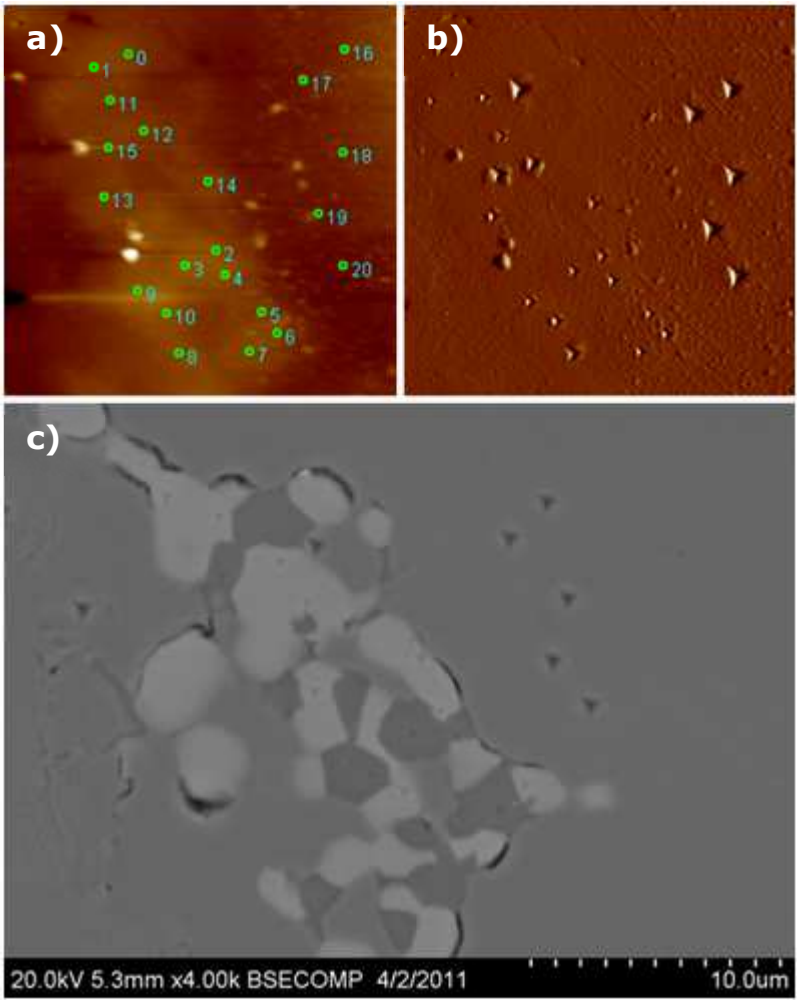

Figure 21 - Nano-indentation on hard phase in sample PT09-238 head
a) AFM scan before indentation with click script
b) AFM scan shows indents after indentation
c) ZC-image shows distribution of indents within accumulation of compact hard phases

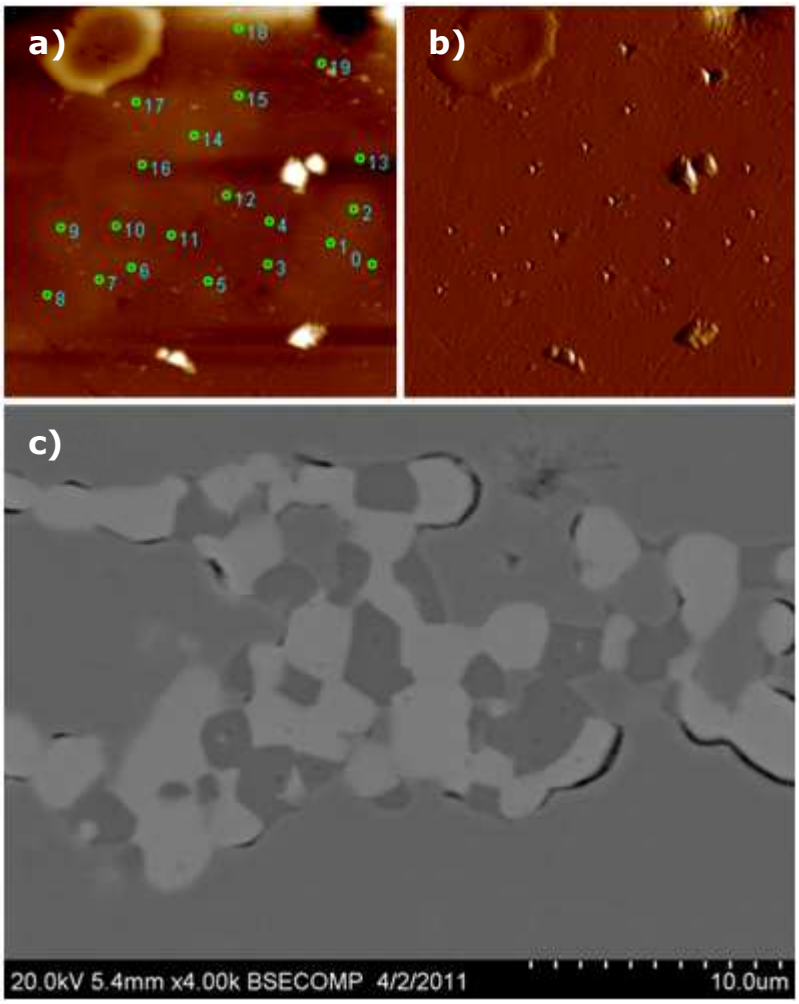

Figure 22 - Nano-indentation on hard phase in sample PT09-238 head
a) AFM scan before indentation with click script
b) AFM scan shows indents after indentation
c) ZC-image shows distribution of indents within accumulation of compact hard phases

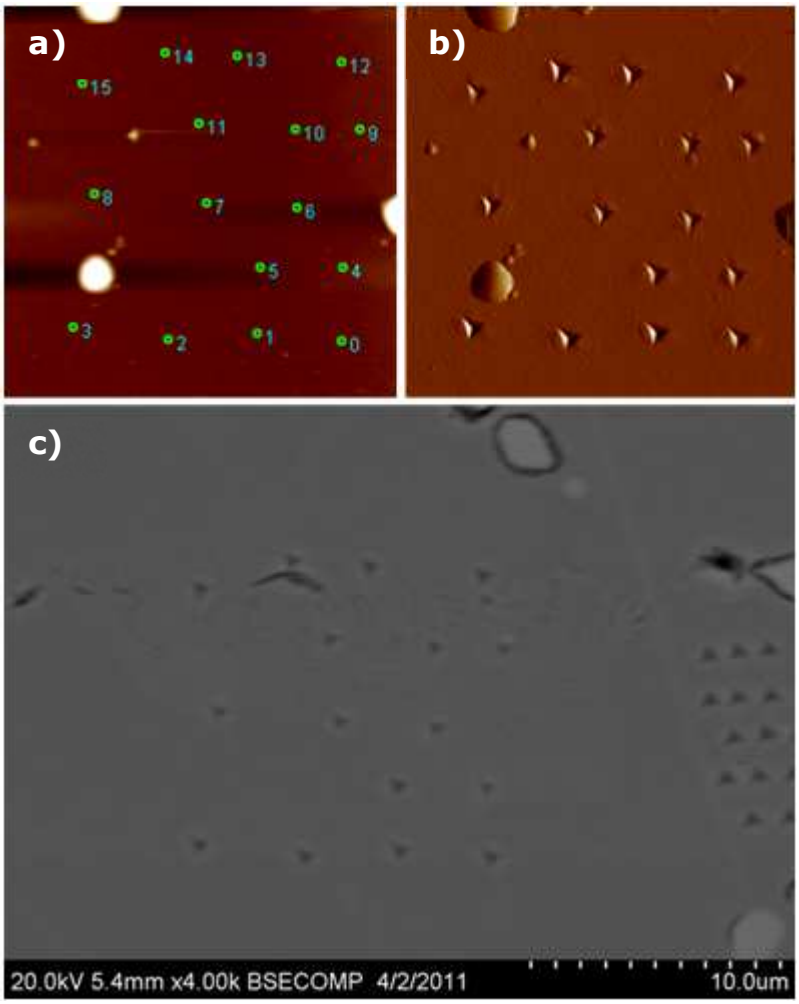

Figure 23 - Nano-indentation on sample PT09-238 head
a) AFM scan before indentation with click script
b) AFM scan shows indents after indentation
c) ZC-image shows indents within mixed percolated

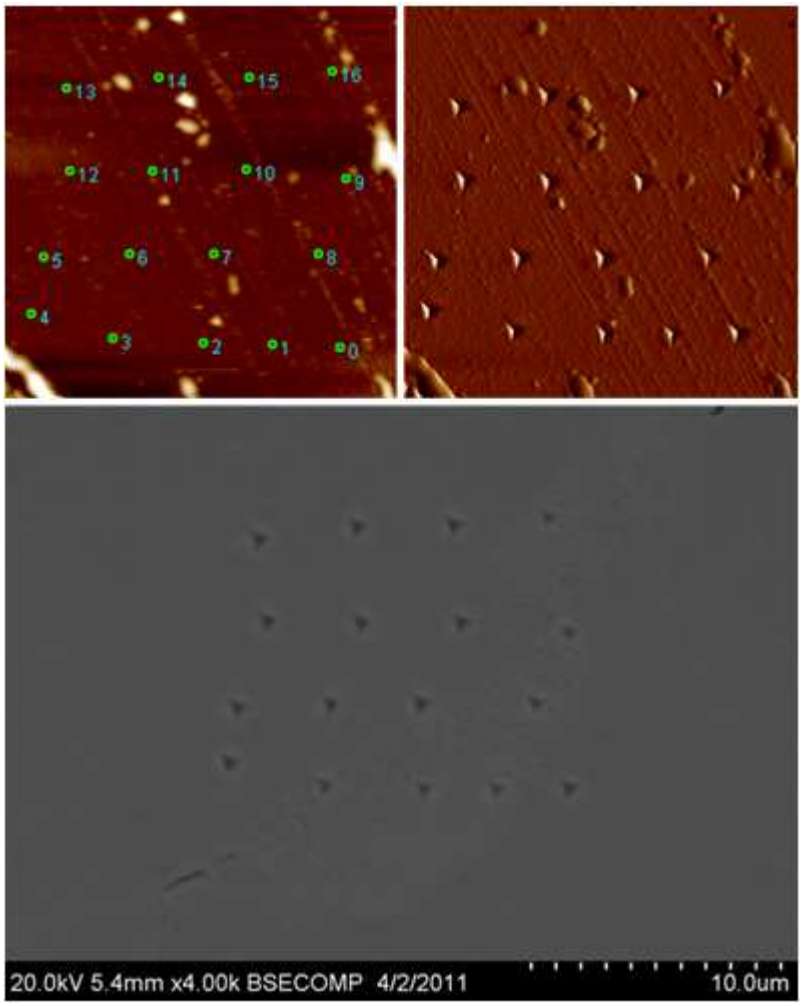

Figure 24 - Nano-indentation on sample PT09-238 head
a) AFM scan before indentation with click script
b) AFM scan shows indents after indentation
c) ZC-image of compact hard phase and mixed percolated phase, showing distribution of indents

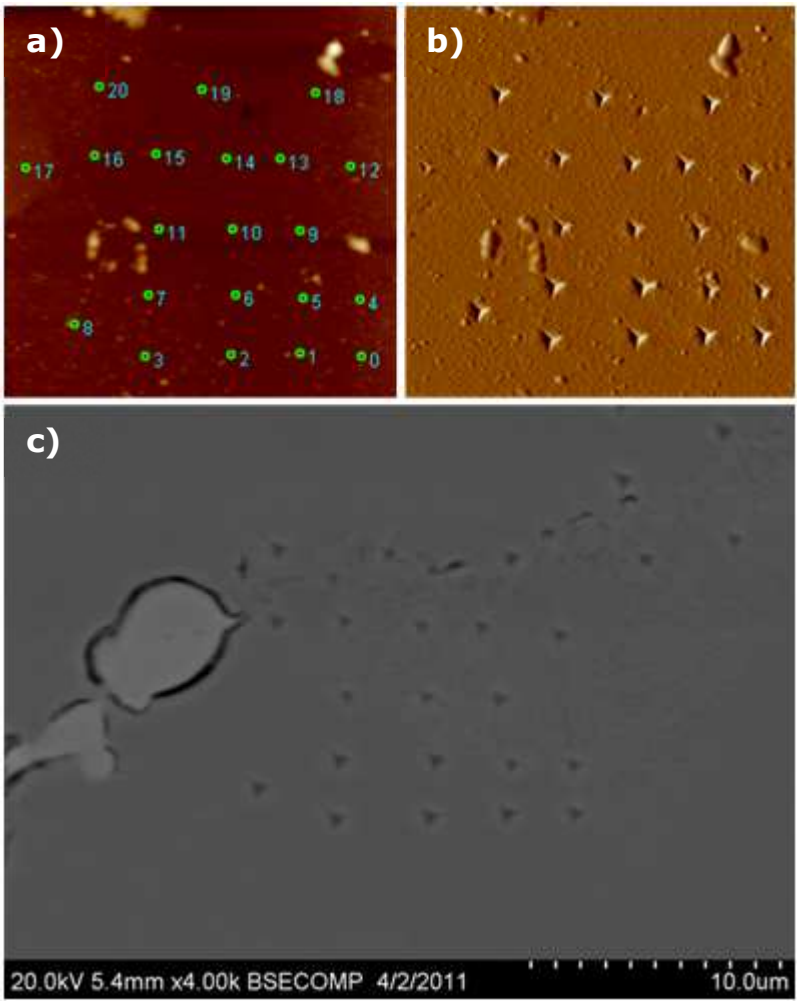

Figure 25 - Nano-indentation on sample PT09-238 head
a) AFM scan before indentation with click script
b) AFM scan shows indents after indentation
c) ZC-image of compact hard phase and mixed percolated phase, showing distribution of indents

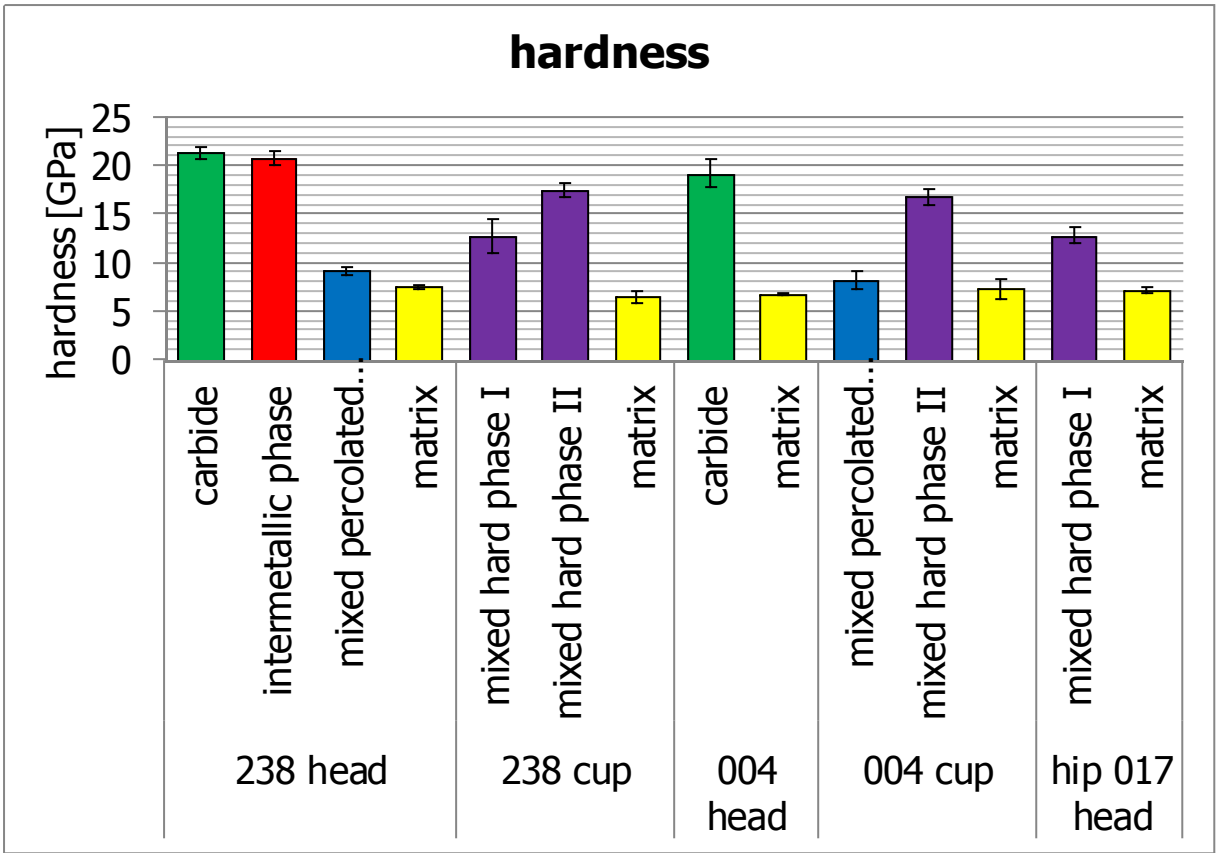

Figure 26 – Hardness diagram

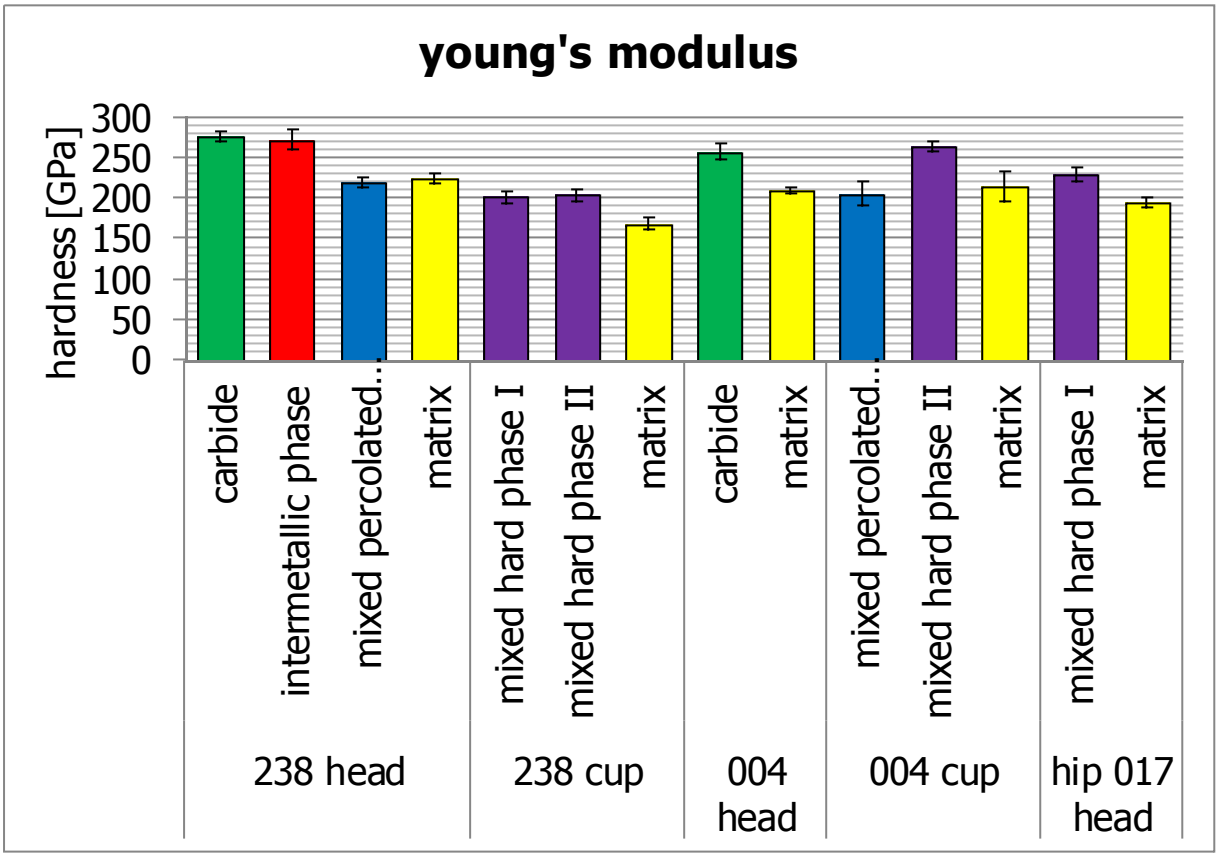

Figure 27 – Young´s modulus diagram

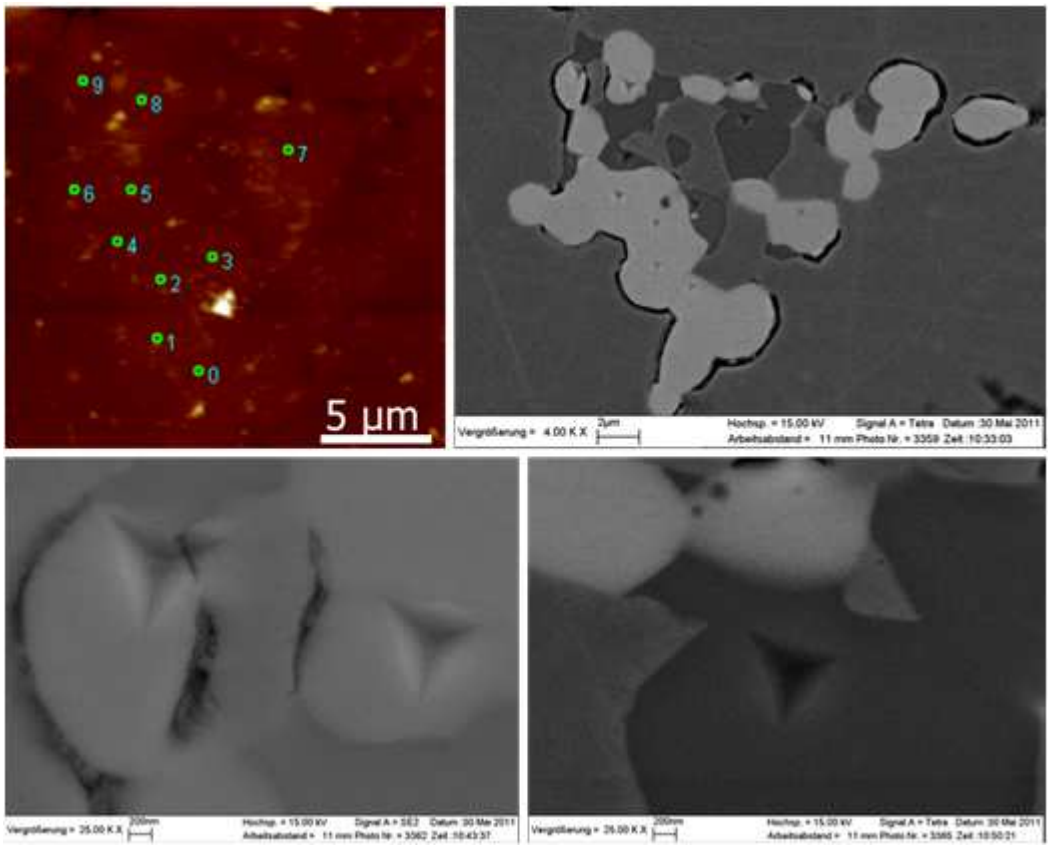

Figure 28 – Nano-indentation with increasing load (PT09-238)
a) AFM-scan before indentation with click-script
b) ZC-image exhibits where indents are located
c) Indents no. 9 (10 mN) and 8 (9.3 mN) in intermetallic phase
d) Indent no. 7 (8.7 mN) in carbide

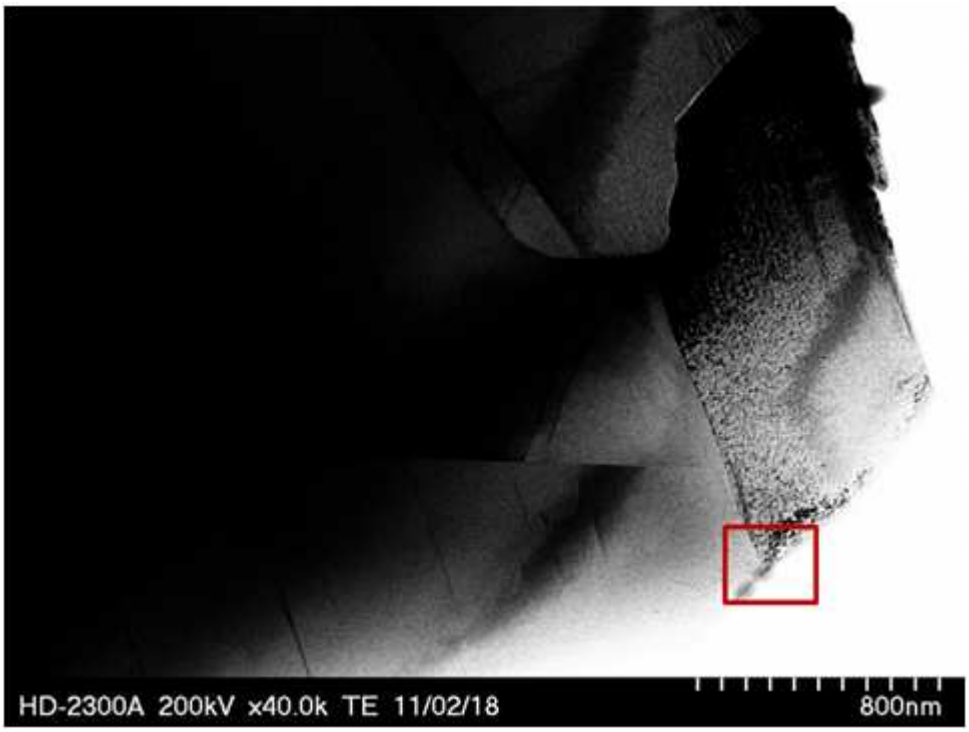

Figure 29 - BF-image shows grain boundary within hip 004. Rectangle indicates location of EDX scan.

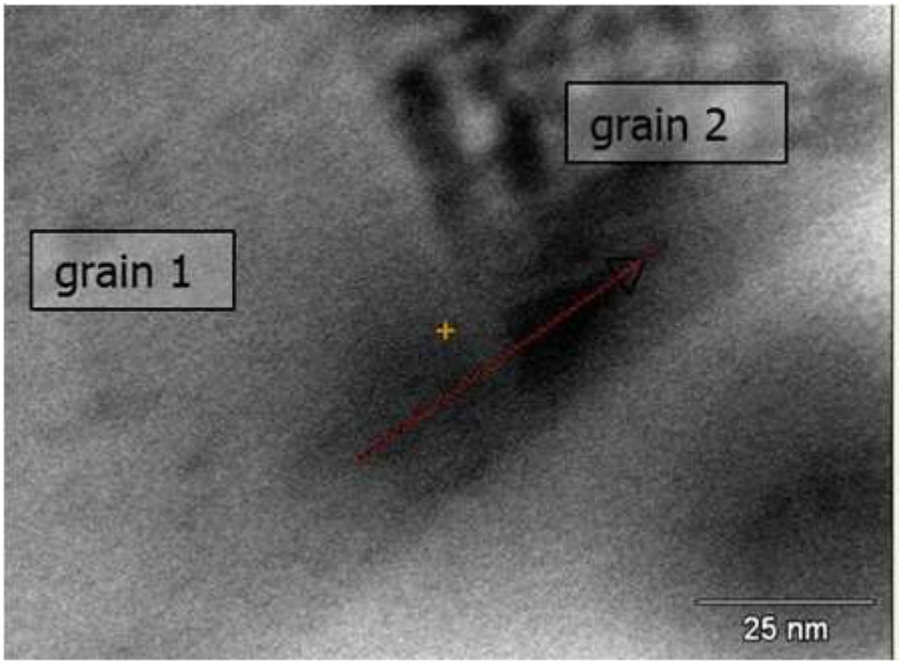

Figure 30 – BF of grain boundary (hip 004). Red arrow indicates location and direction of EDX scan across grain boundary.

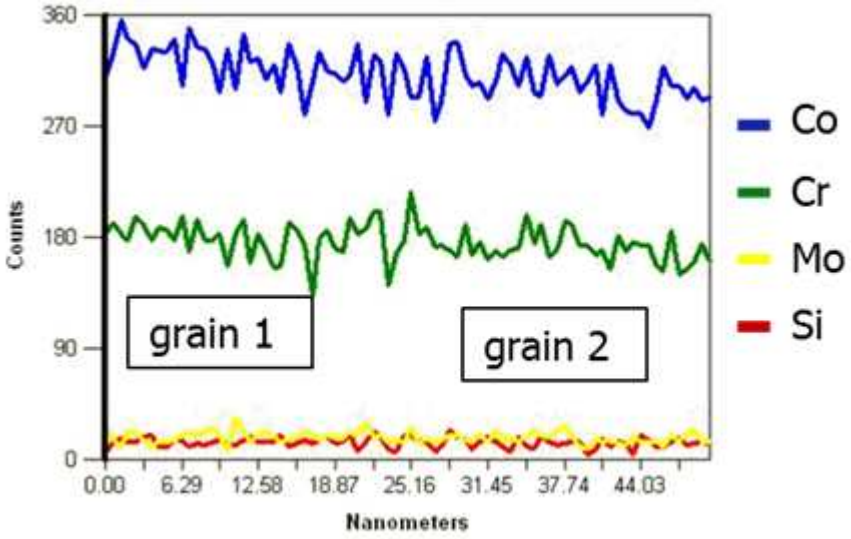

Figure 31 – Diagram of EDX line scan across grain boundary from Figure 30 with 80 points of measurement

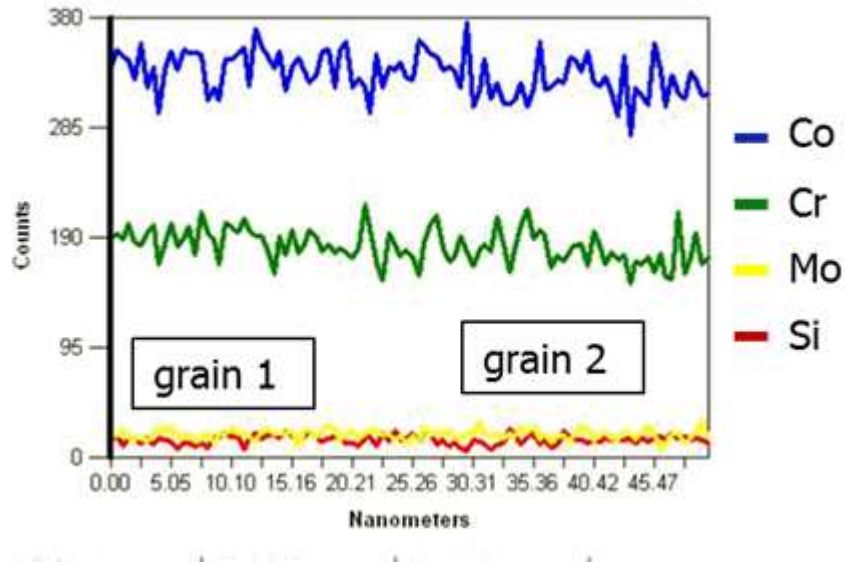

Figure 32 - Diagram of EDX line scan across grain boundary Figure 30 with 100 points of measurement

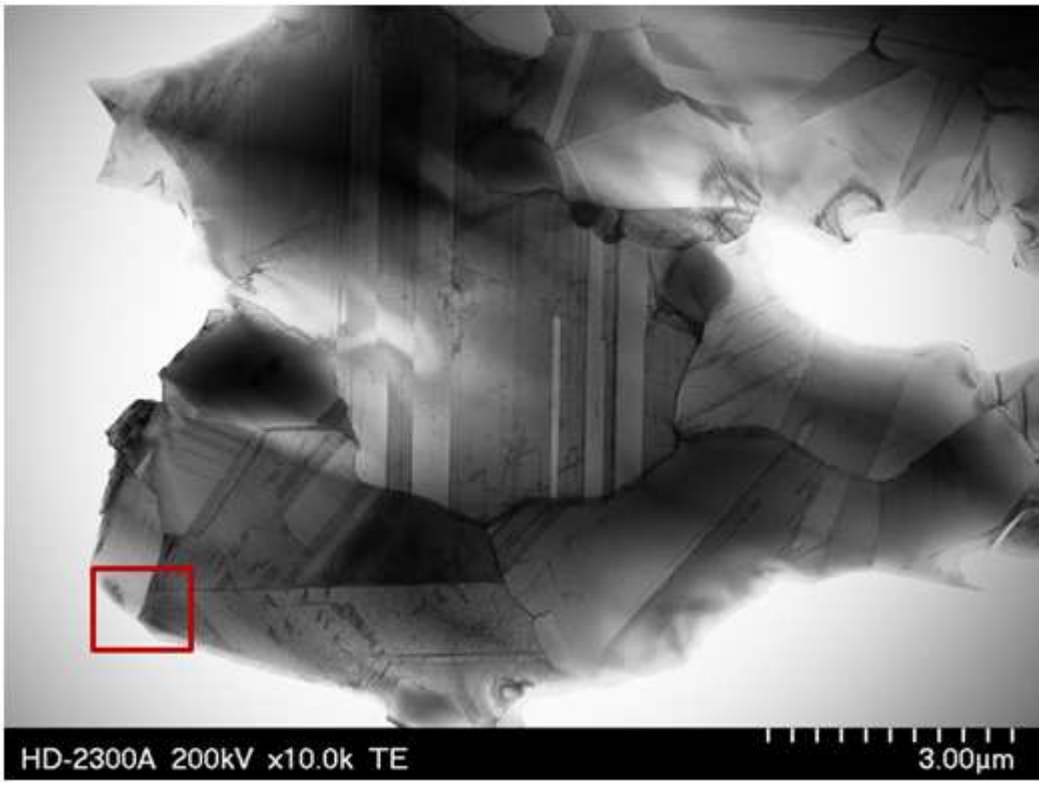

Figure 33 - BF-image of hc wrought alloy (hip 004)

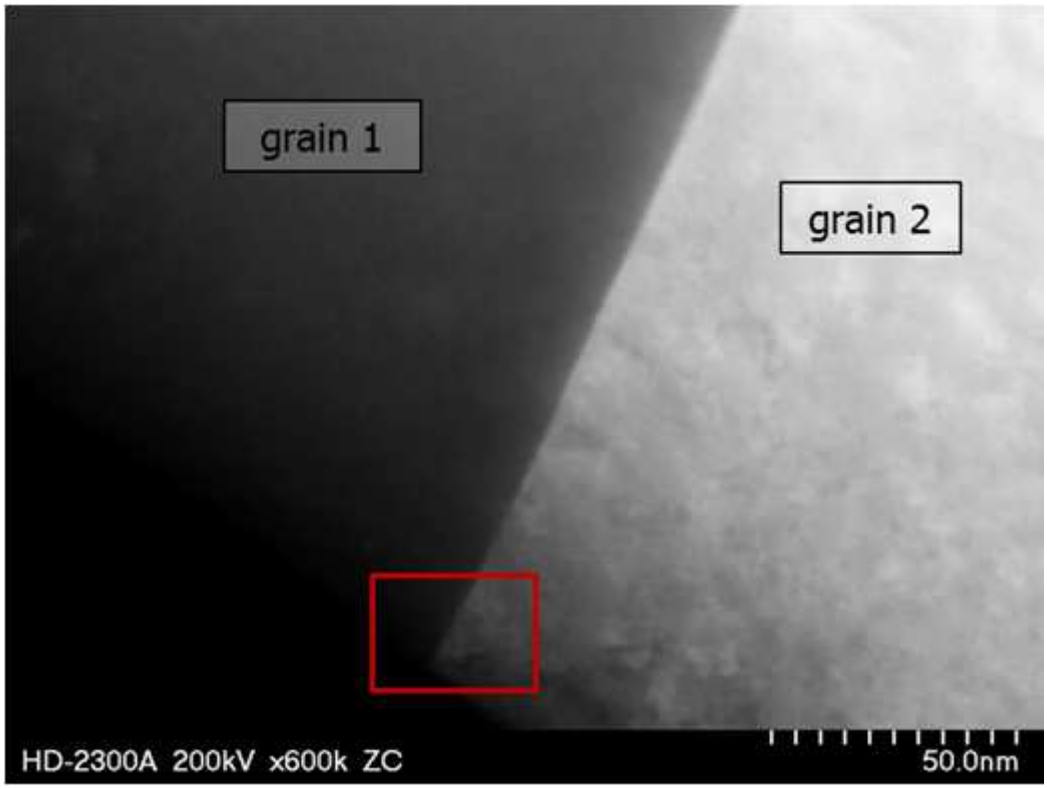

Figure 34 - ZC-image shows grain boundary. Rectangle indicates location of EELS scan.

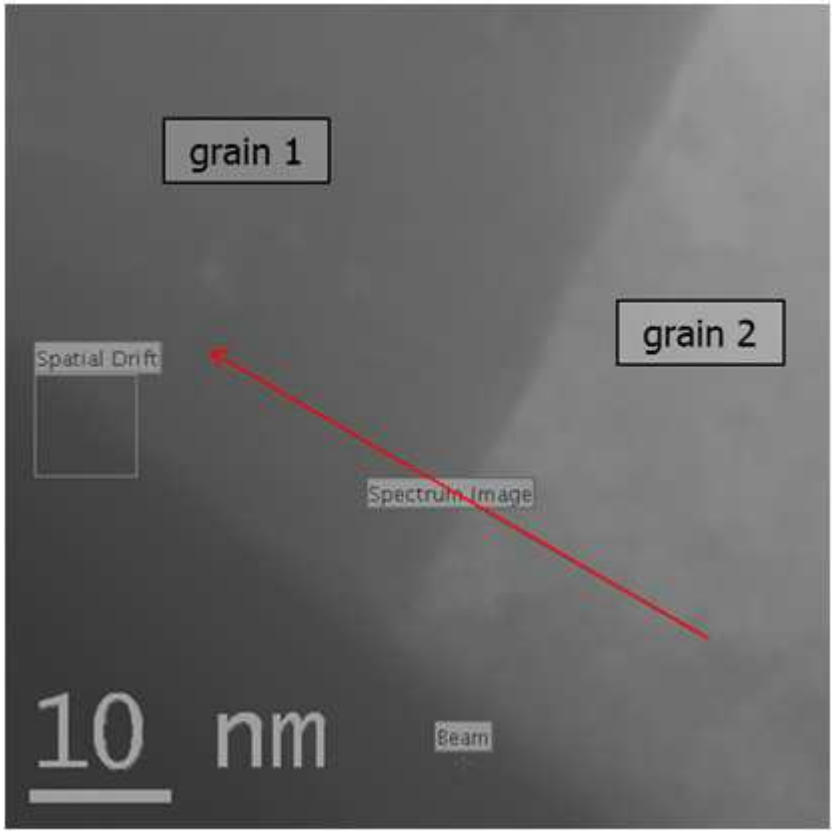

Figure 35 - ZC-image shows phase boundary. Arrow indicates location and direction of EELS line scan.

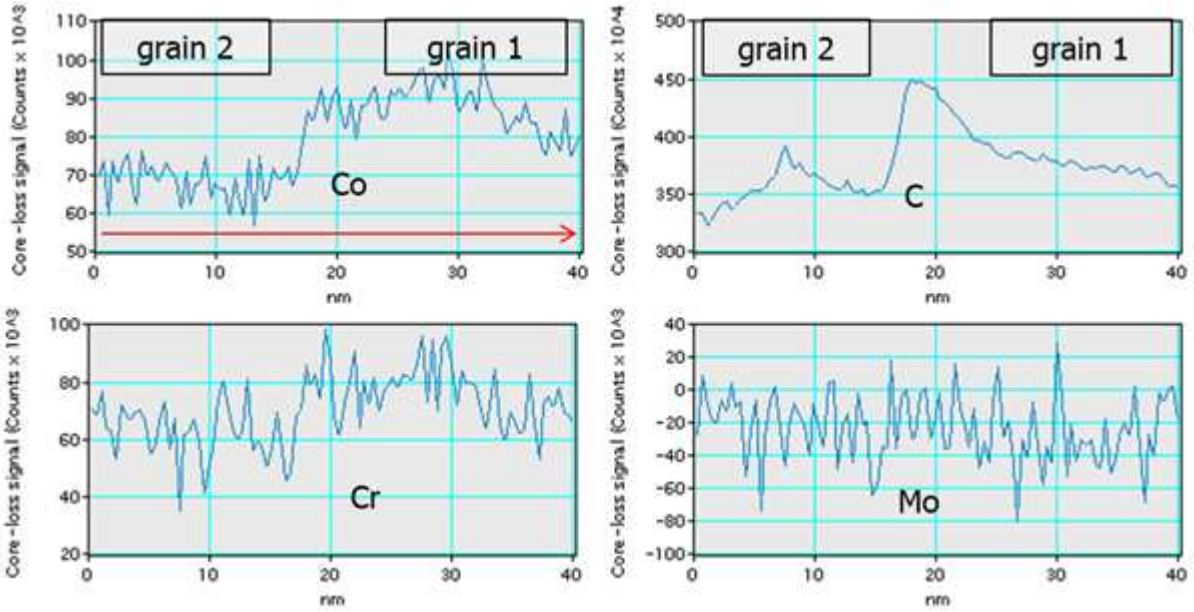

Figure 36 - EELS line scan diagram corresponding to Figure 35.

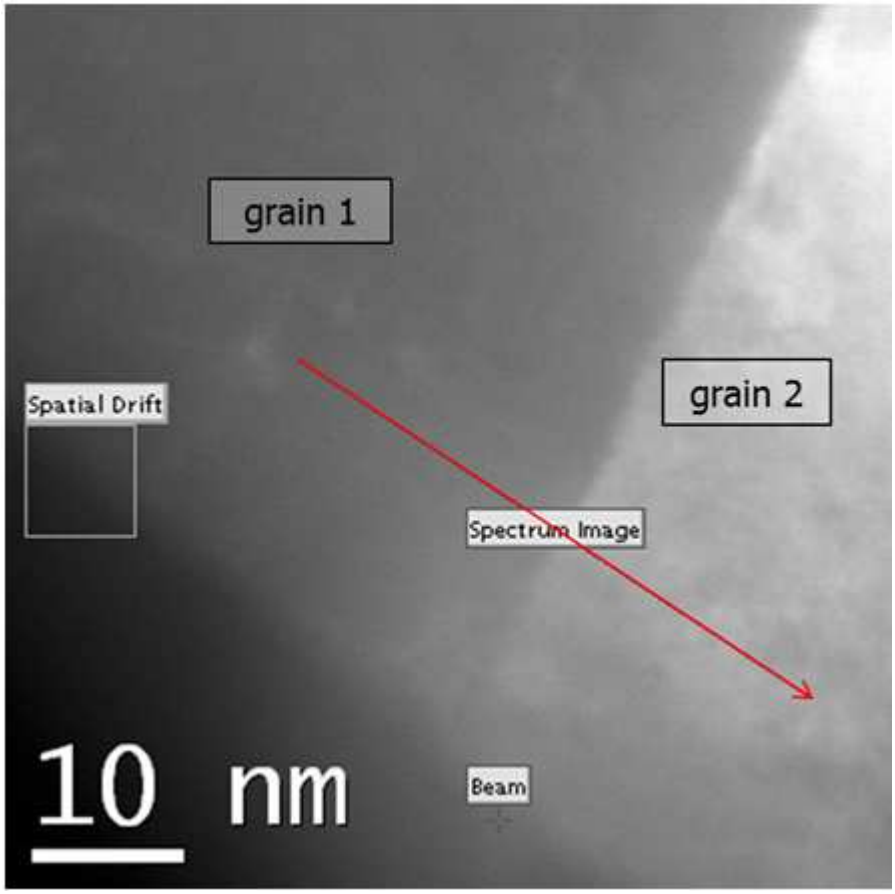

Figure 37 - ZC-image shows phase boundary. Arrow indicates location and direction of EELS line scan.

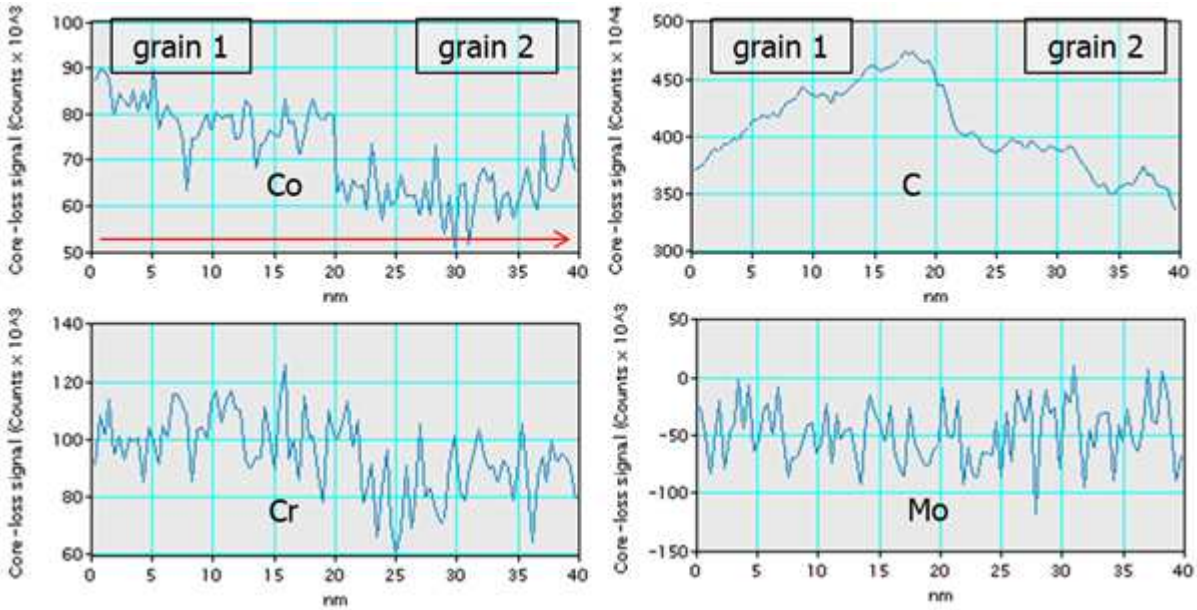

Figure 38 - EELS line scan diagram corresponding to Figure 37.

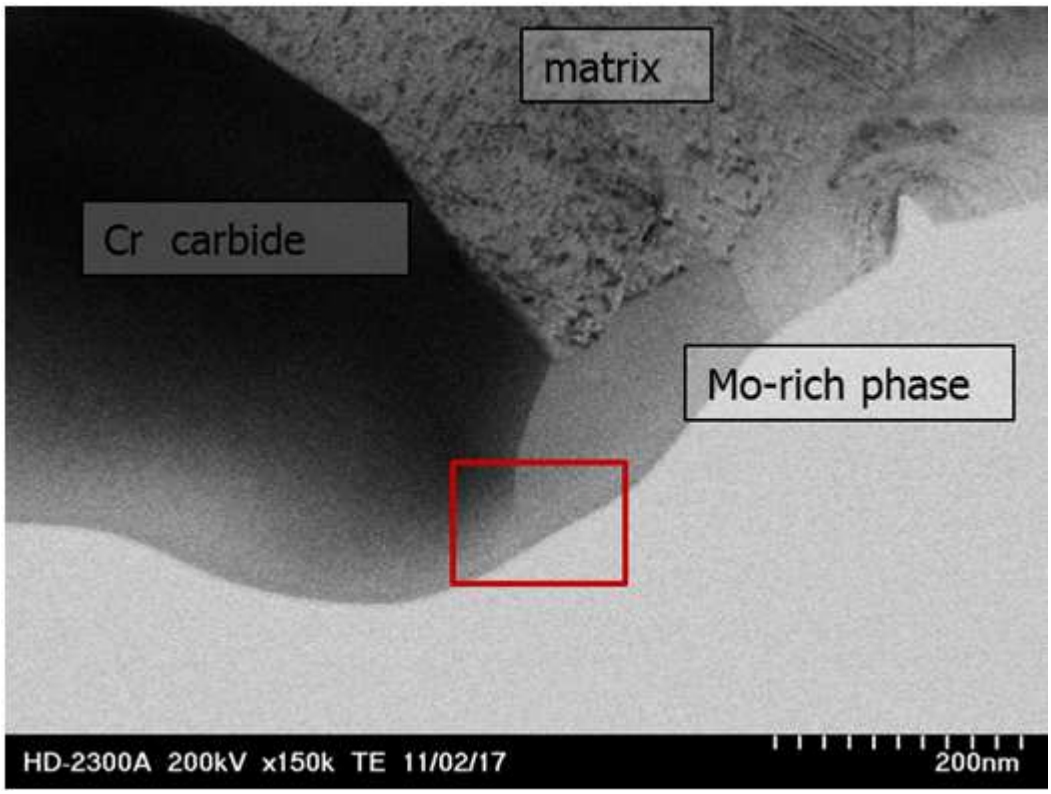

Figure 39 – BF of hc wrought alloy (hip004)

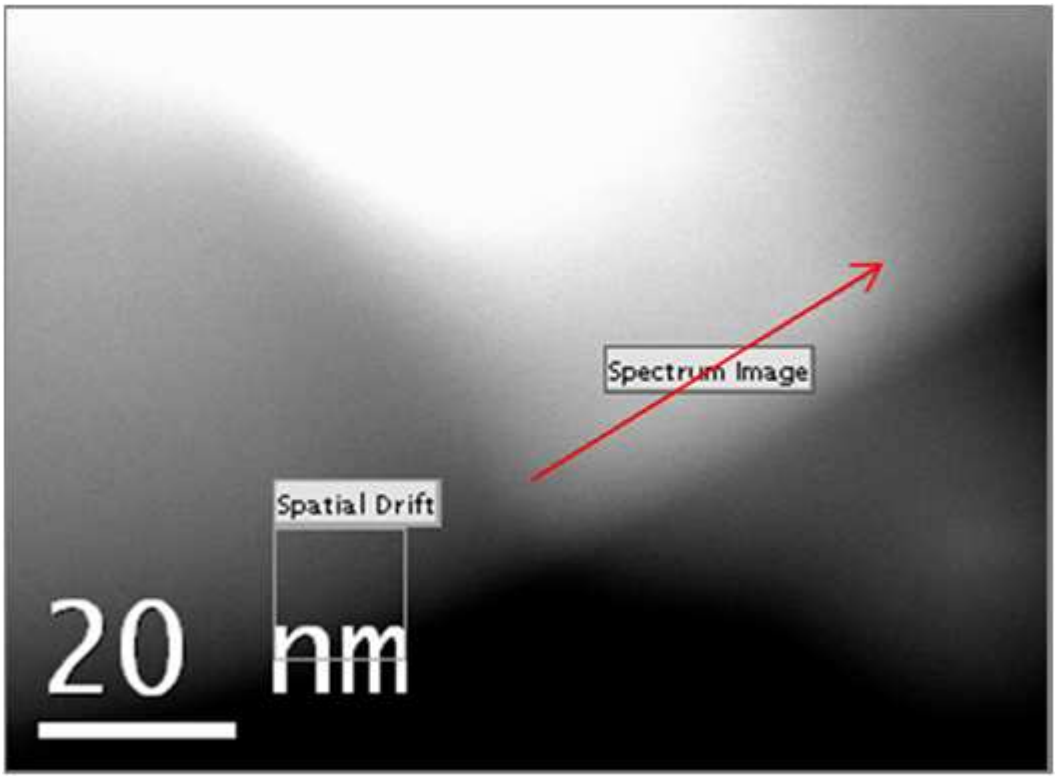

Figure 40 – ZC- image of phase boundary within hc wrought alloy (Figure 40). Red arrow indicates location and direction of EELS scan.

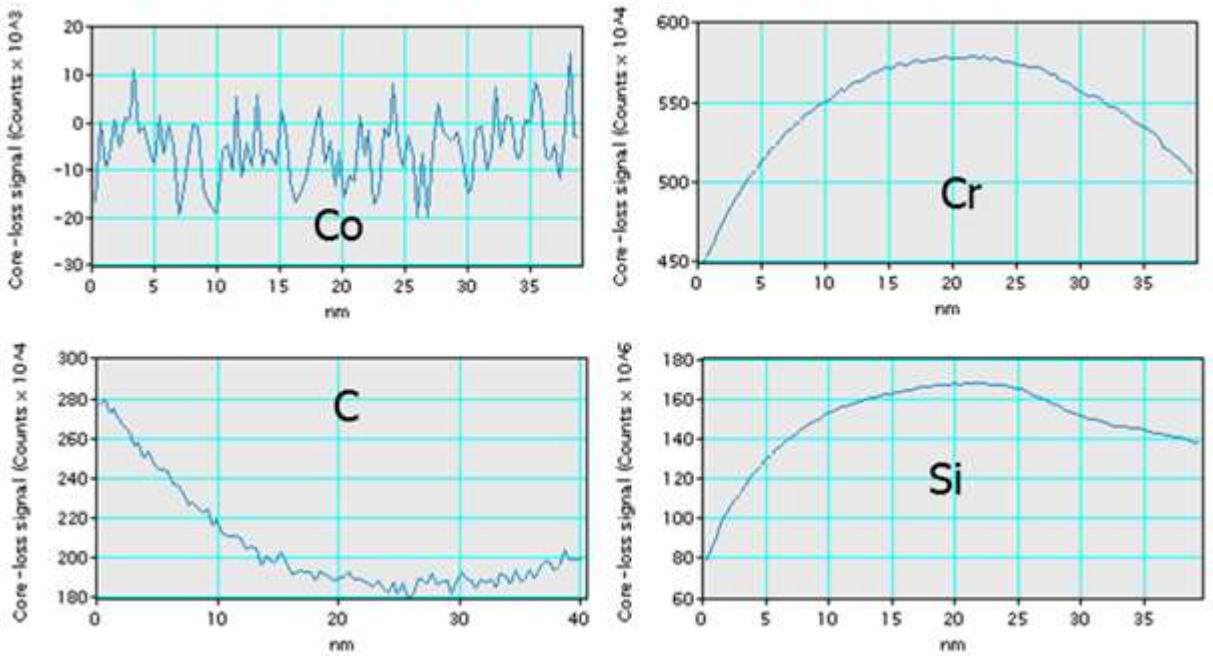

Figure 41 – EELS line scan across phase boundary (Figure 40). Results unevaluable due to sample drift.

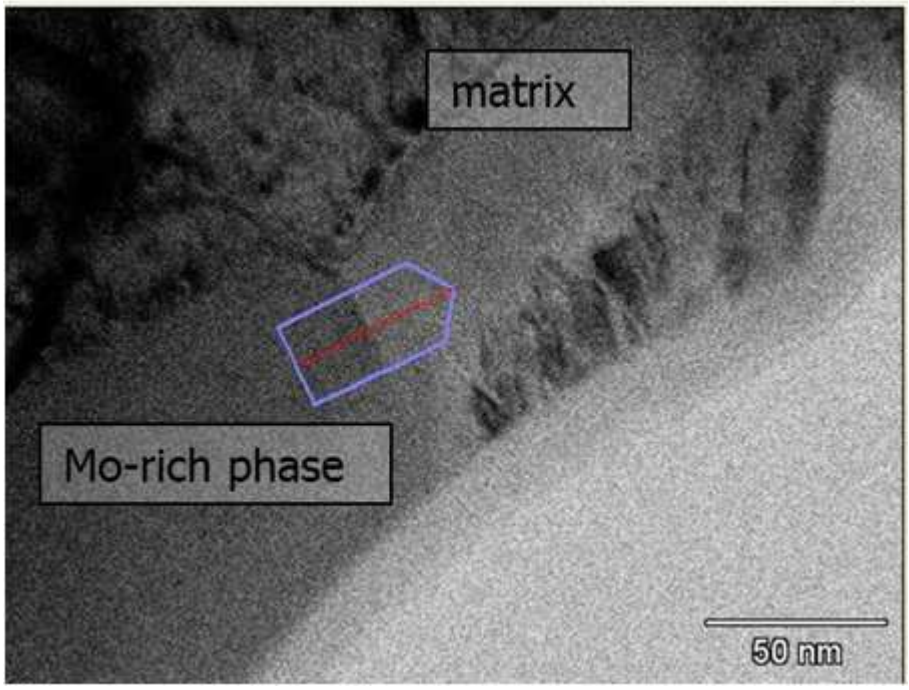

Figure 42 – BF-image of molybdenum-rich phase within hc wrought alloy (hip004). Blue arrow indicates location and direction of extracted line scan.

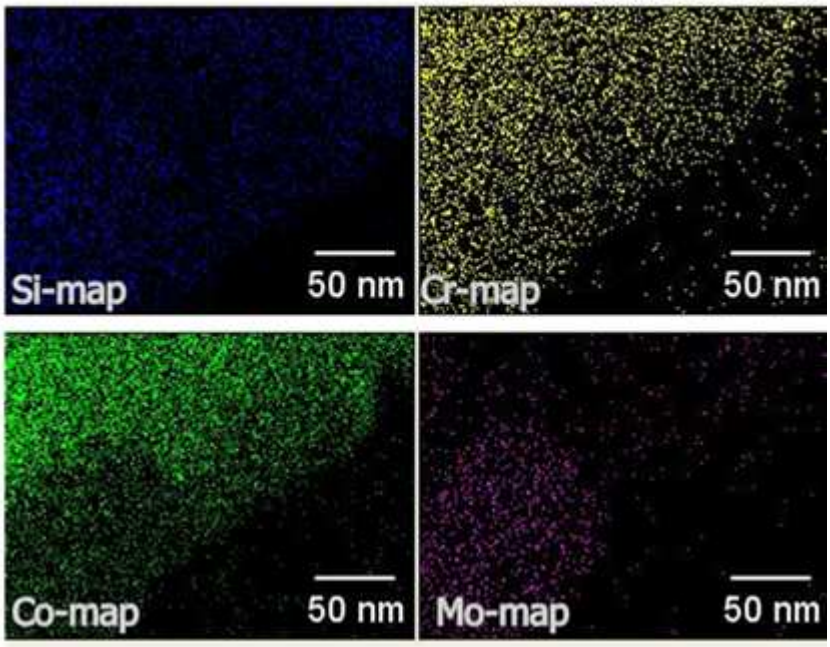

Figure 43 – EDX mapping across molybdenum-rich phase of Figure 42.

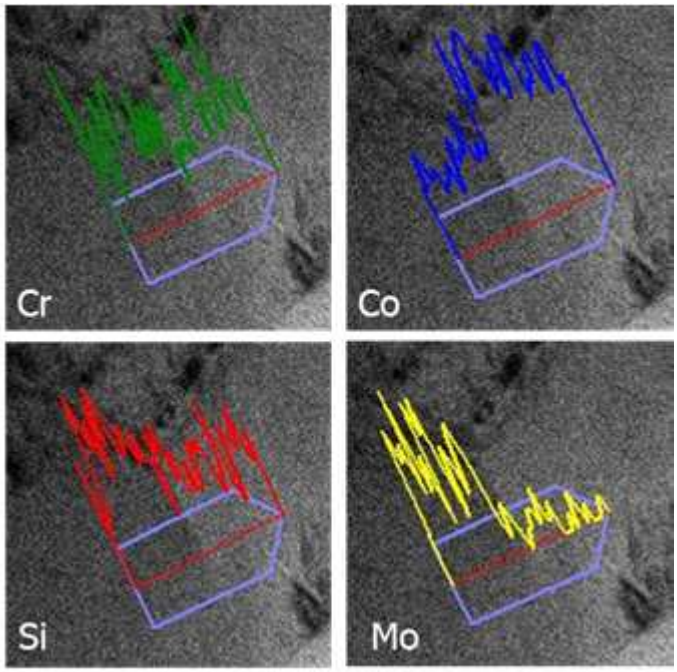

Figure 44 – Extracted line scans out of EDX mapping (Figure 43)

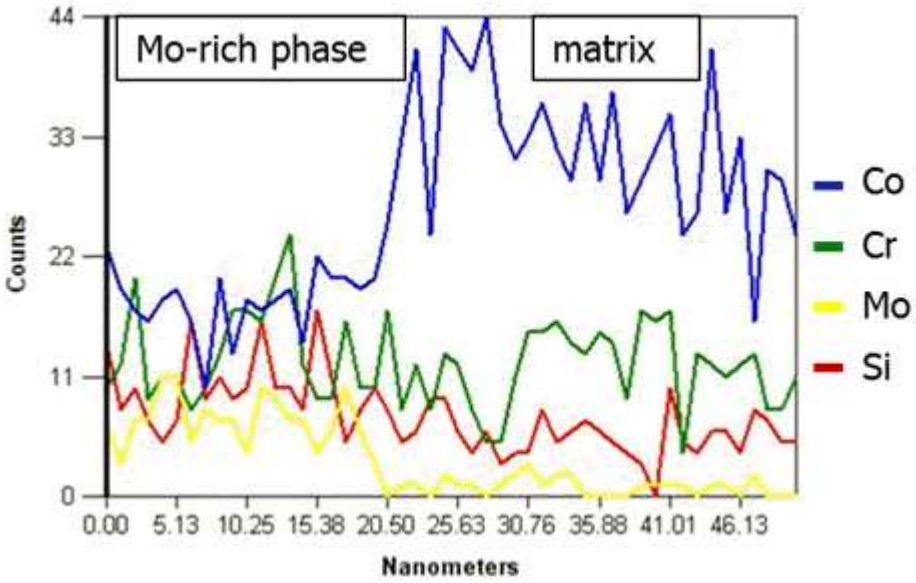

Figure 45 – Diagram of extracted line scans across phase boundary (Figure 44)

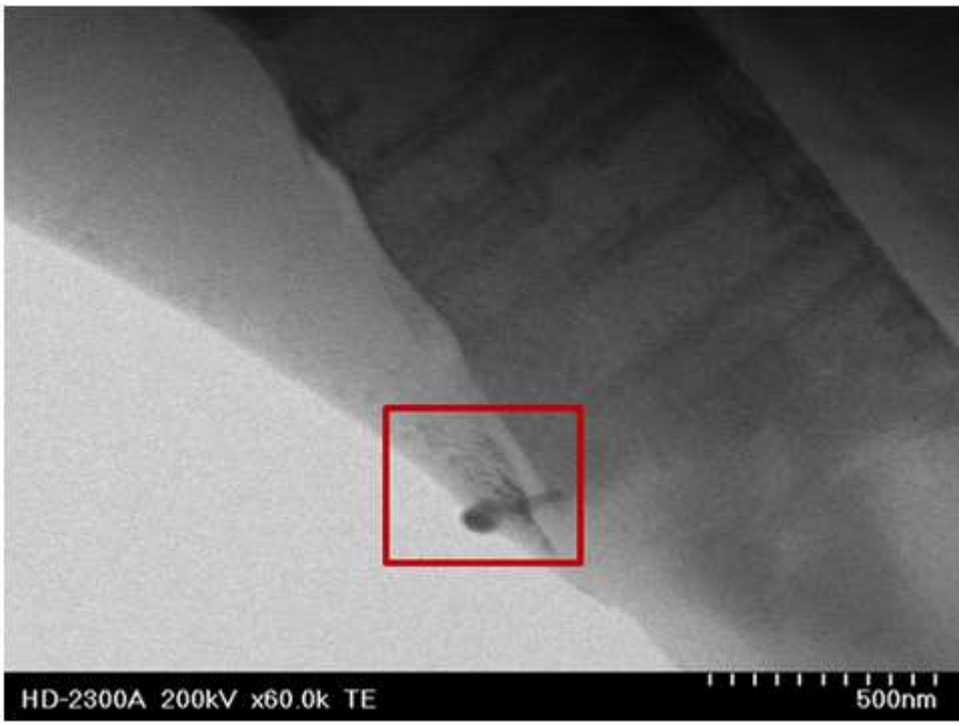

Figure 46 – BF-image from hc wrought alloy (hip 004). Carbide between two grains. Red rectangle indicates location for EDX and EELS measurement.

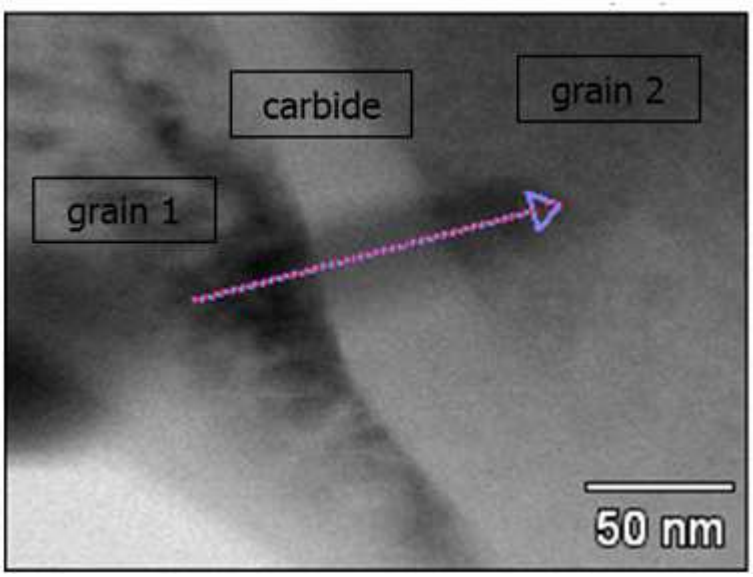

Figure 47 – BF-image shows carbide between two grains. Arrow indicates location and direction of EDX line scan.

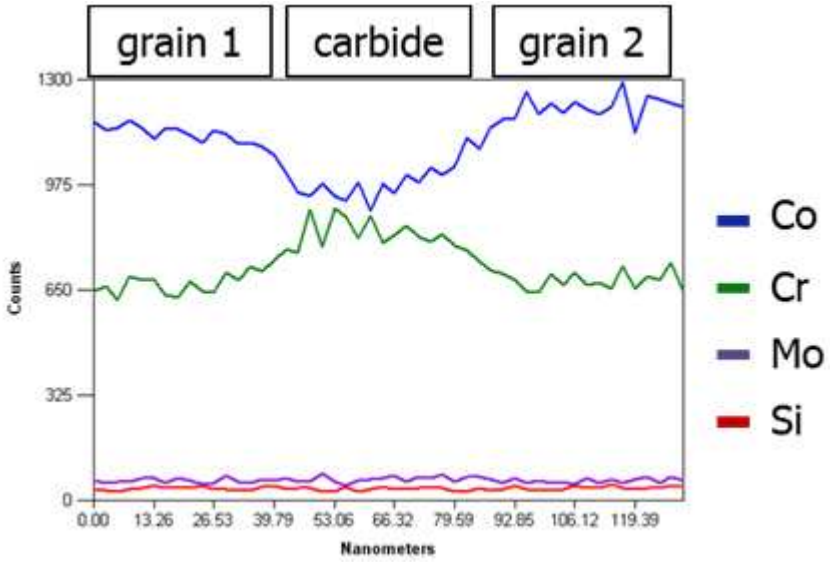

Figure 48 – EDX line scan diagram corresponding to Figure 47. Measured without EDX aperture. Clear influence of surrounding material.

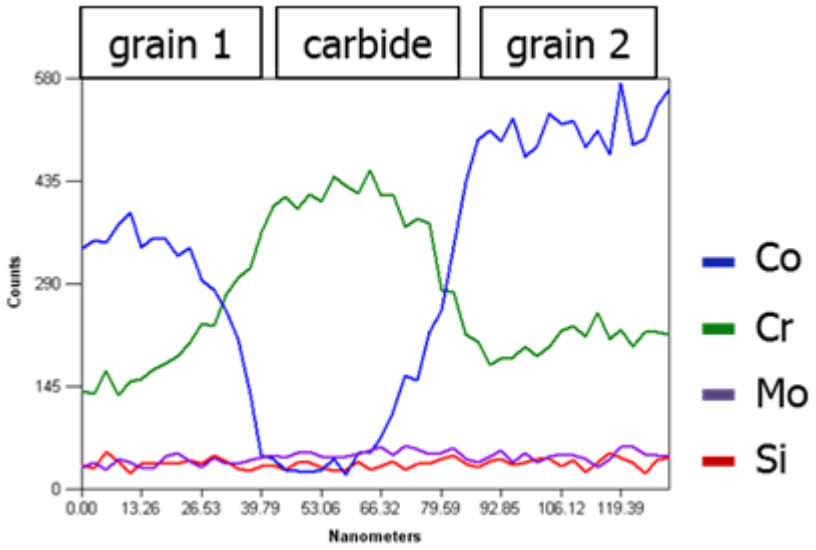

Figure 49 – EDX line scan diagram corresponding to Figure 47. Measured with EDX aperture.

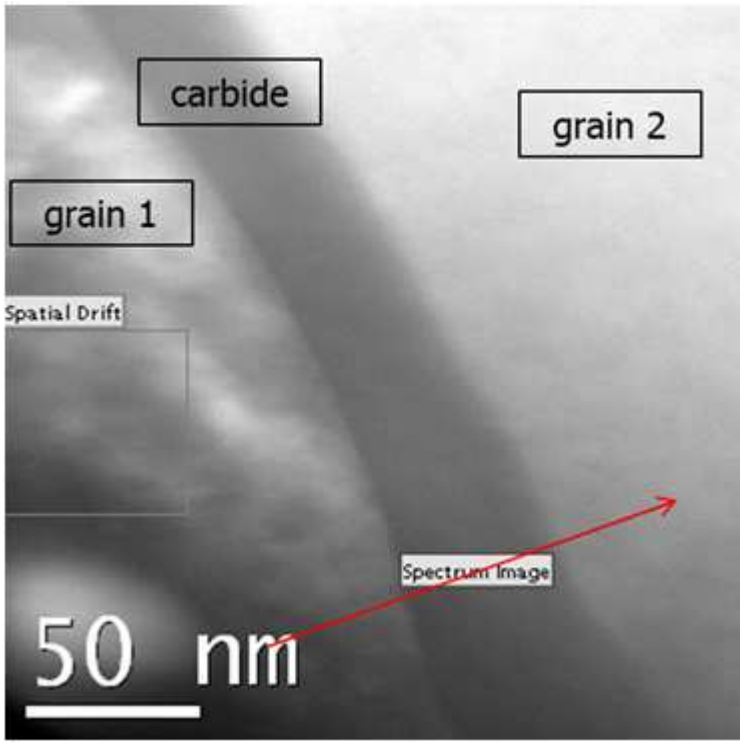

Figure 50 - ZC-image shows carbide between two grains. Arrow indicates location and direction of EELS line scan.

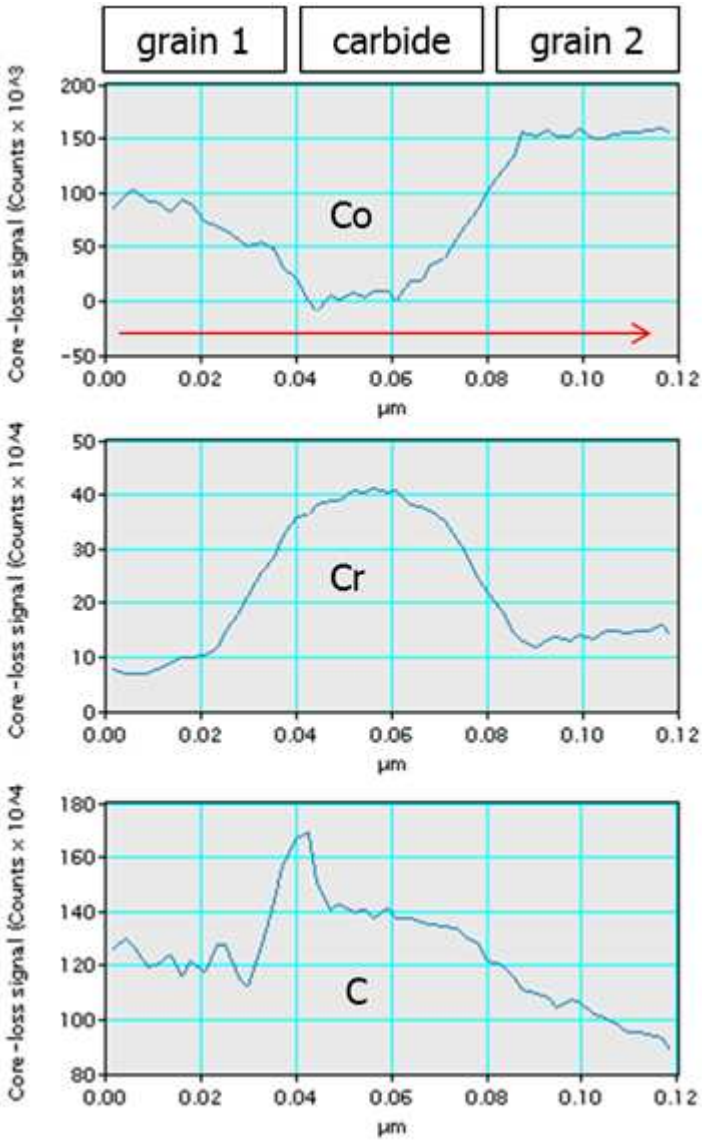

Figure 51 – EELS line scan diagram corresponding to Figure 47.

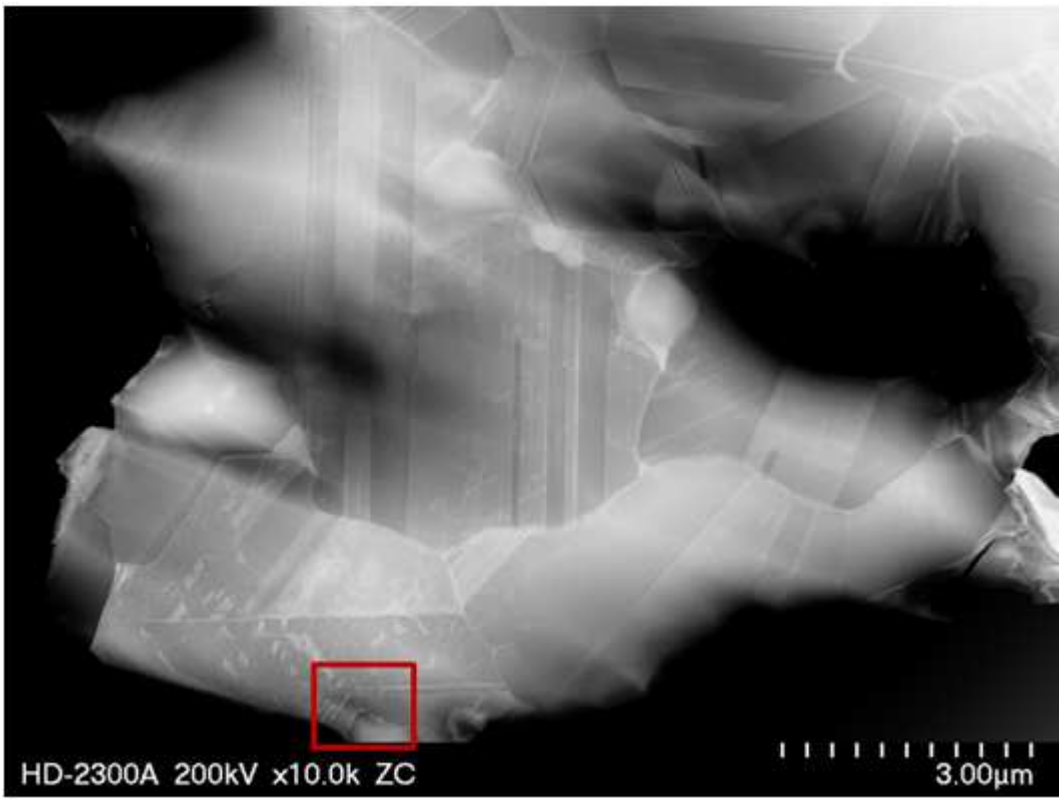

Figure 52 – ZC-image of hc wrought alloy (hip 004).

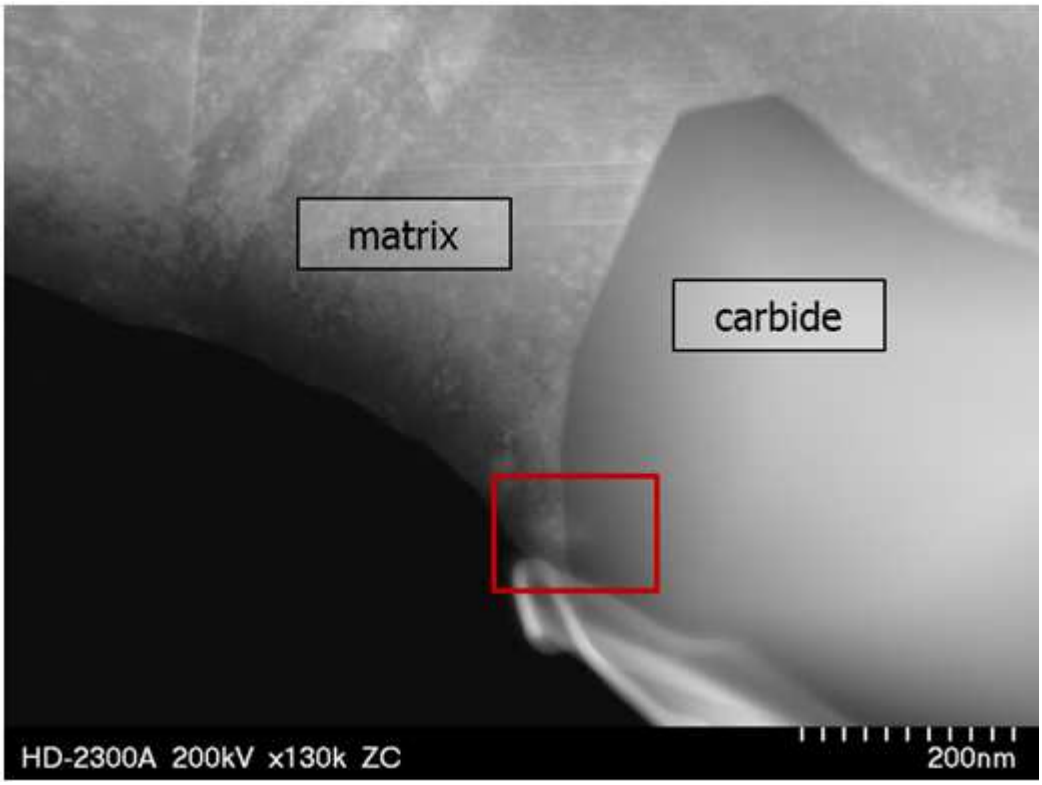

Figure 53 - ZC-image of hc wrought alloy (hip 004). Rectangle indicates location for EELS scans.

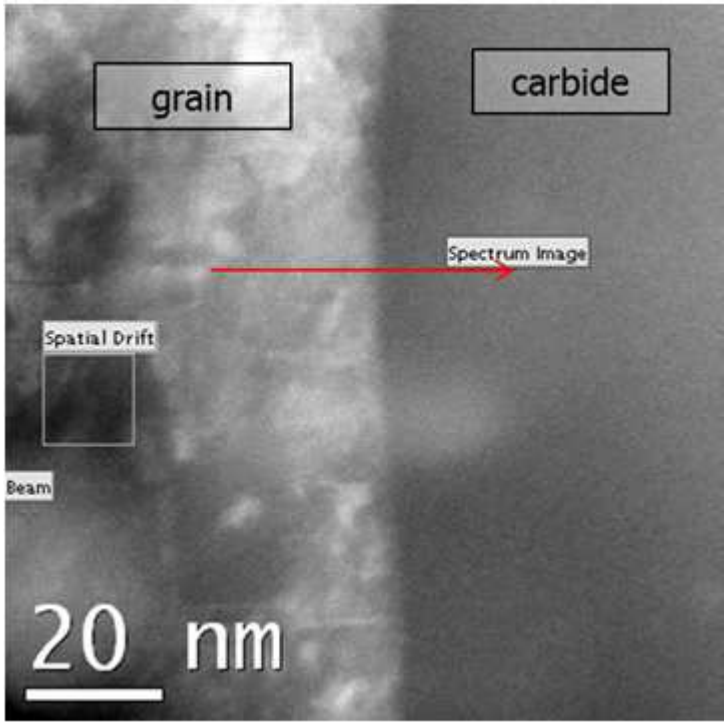

Figure 54 - ZC-image shows phase boundary. Arrow indicates location and direction of EELS line scan.

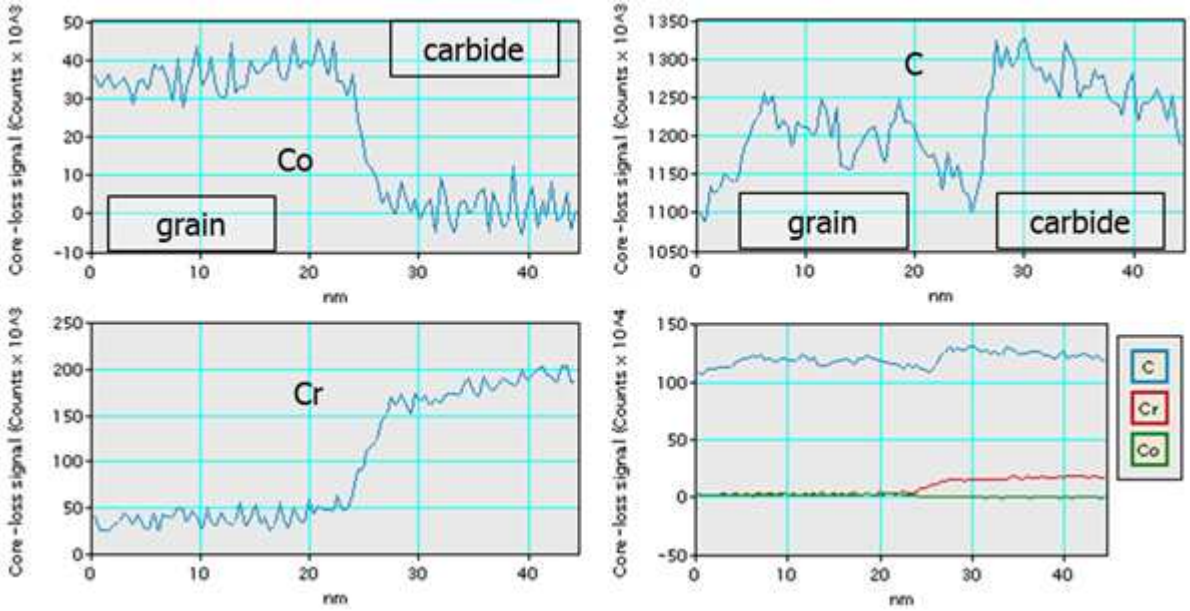

Figure 55 - EELS line scan diagram corresponding to Figure 54.

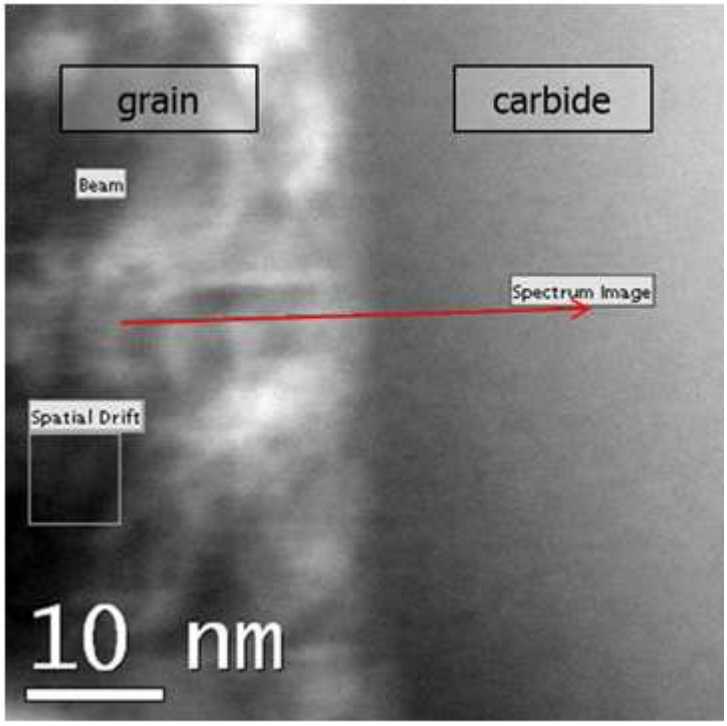

Figure 56 - ZC-image shows phase boundary. Arrow indicates location and direction of EELS line scan.

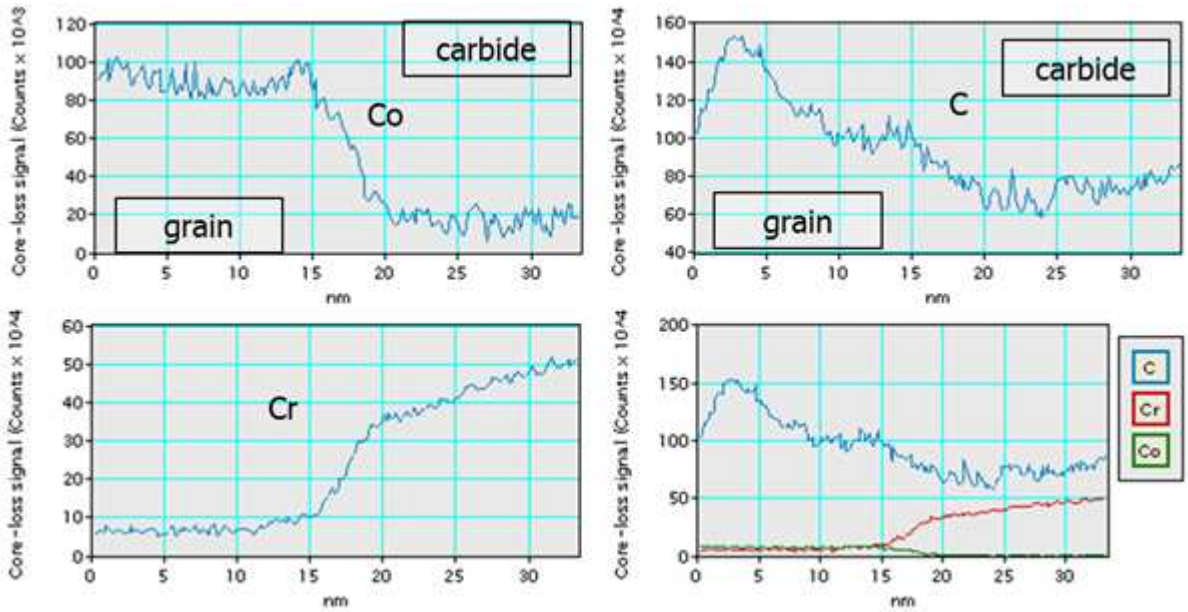

Figure 57 - EELS line scan diagram corresponding to Figure 56.

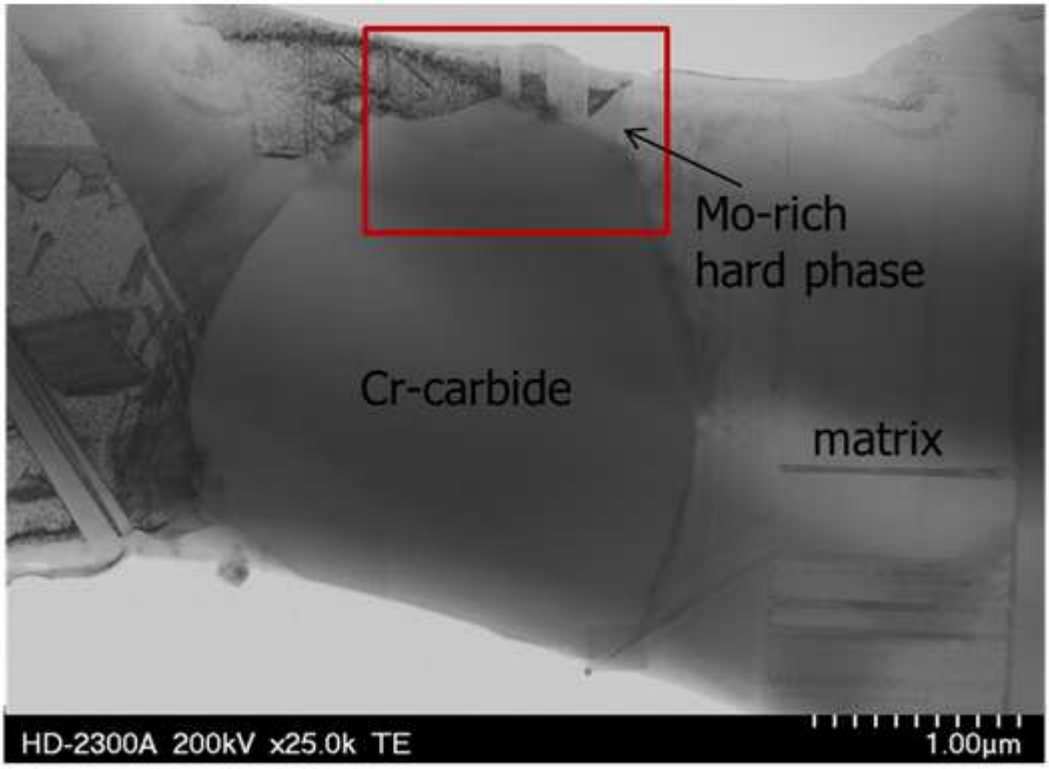

Figure 58 – BF-image shows carbide within hc wrought alloy (hip004)

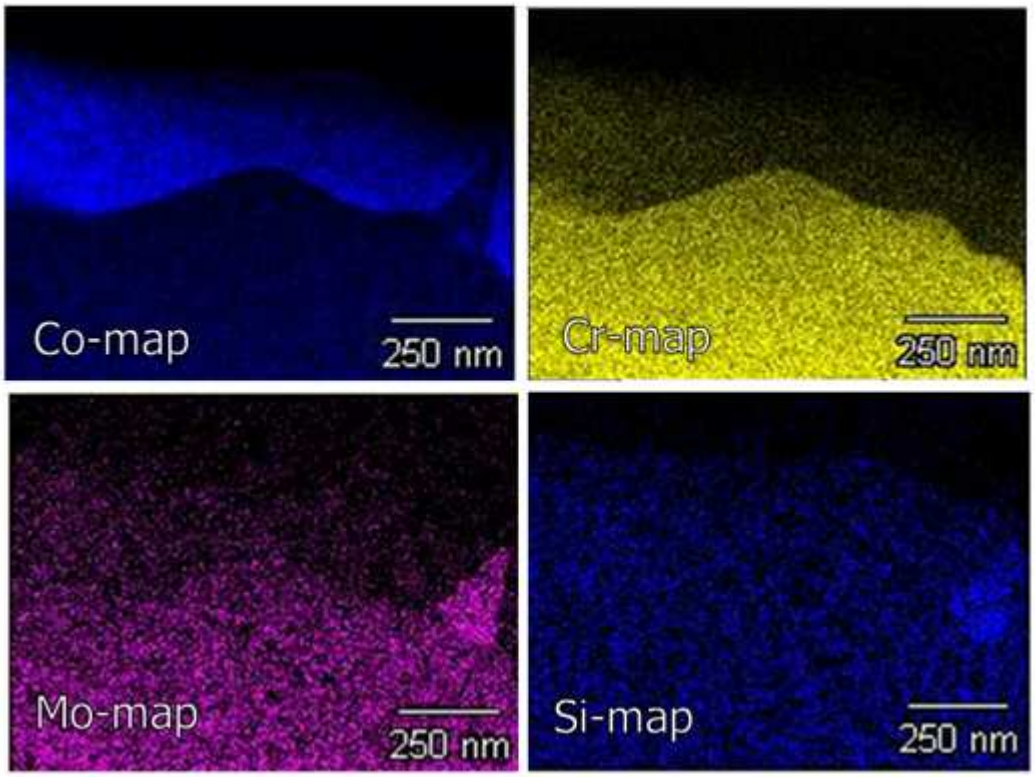

Figure 59 – EDX mapping across carbide from Figure 58

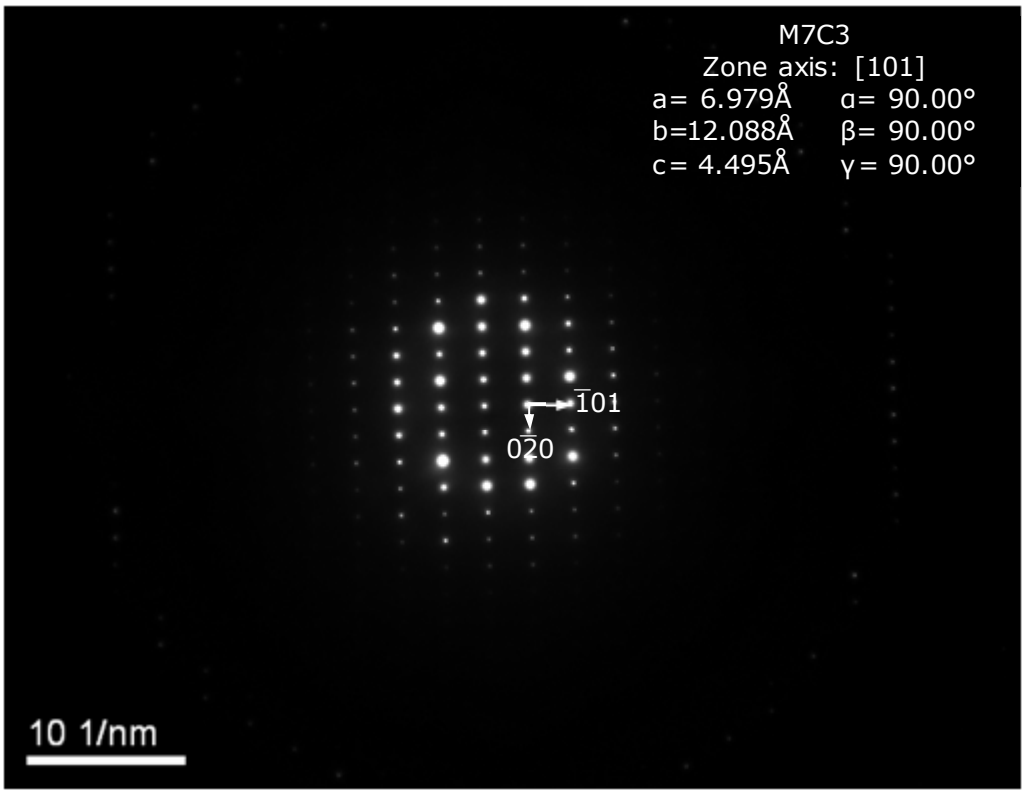

Figure 60 – Diffraction pattern from carbide in Figure 58

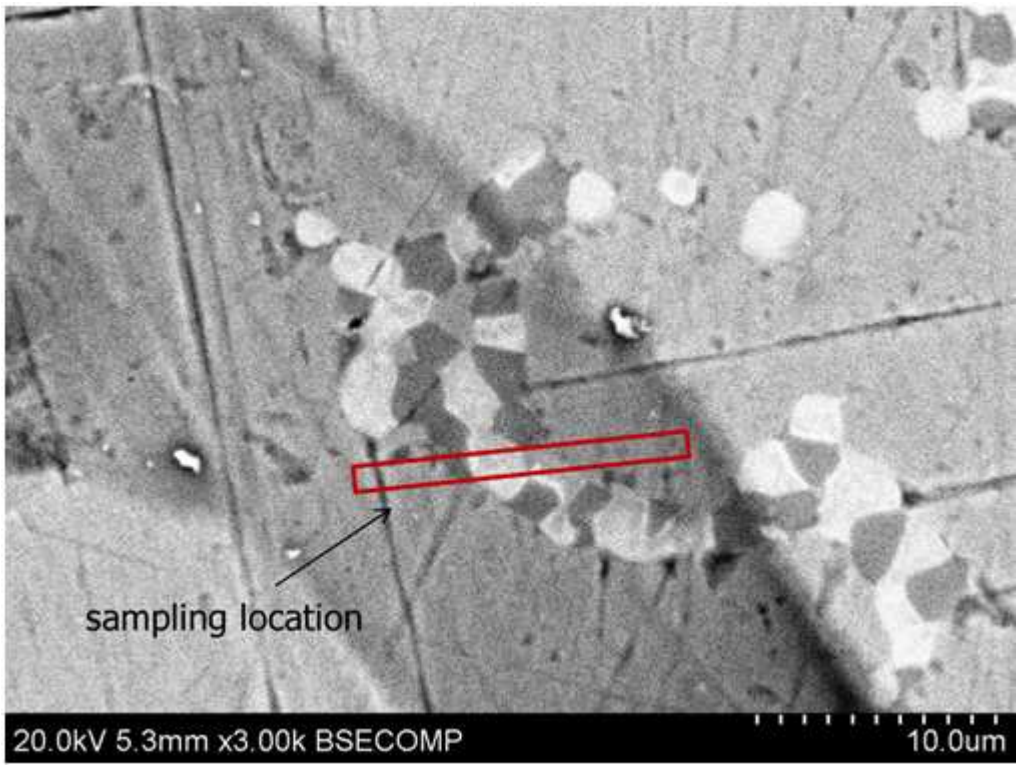

Figure 61 – ZC-image showing an arrangement of hard phases under the surface (PT09-238 head). Rectangle indicates sampling location for FIB.

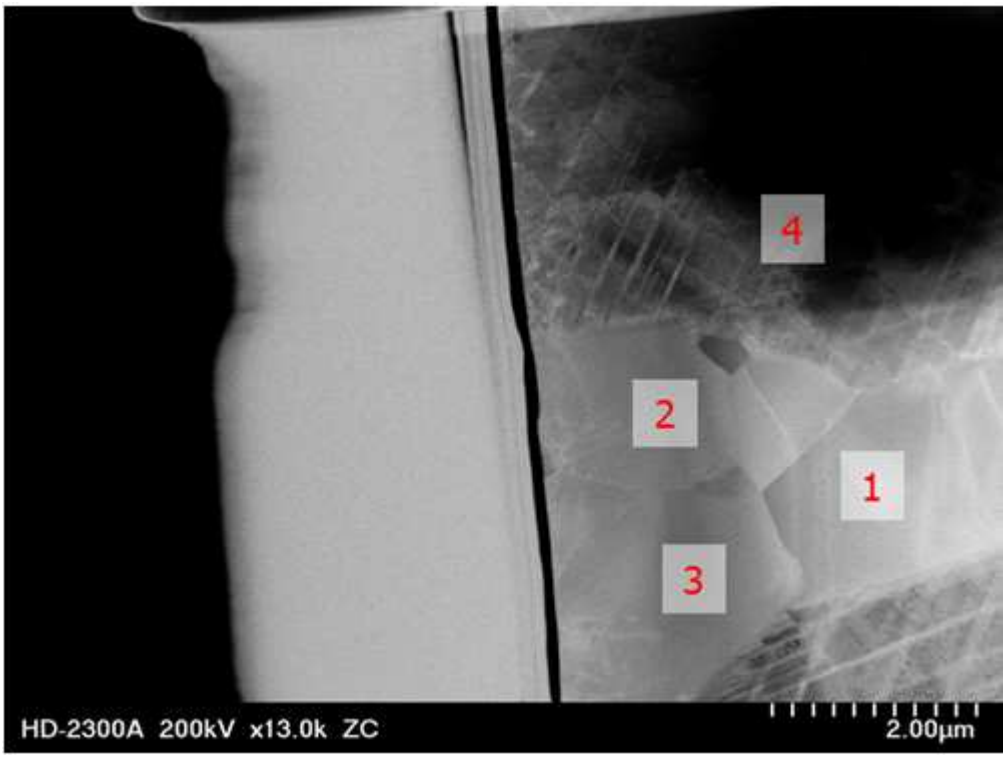

Figure 62 – ZC-image showing a FIB-lamella from PT238 head

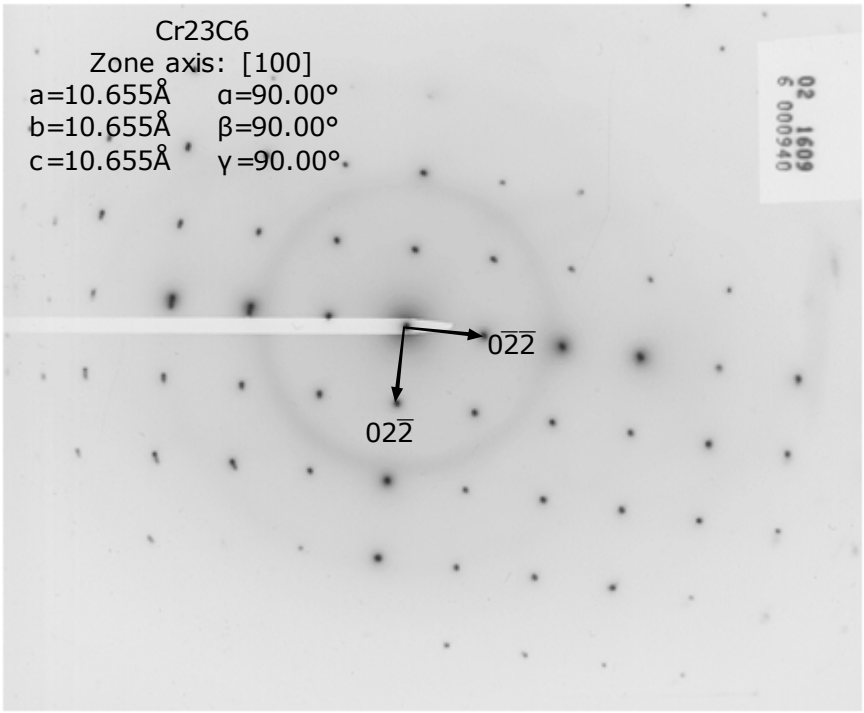

Figure 63 – Diffraction pattern from spot 1 within chromium rich hard phase in Figure 62

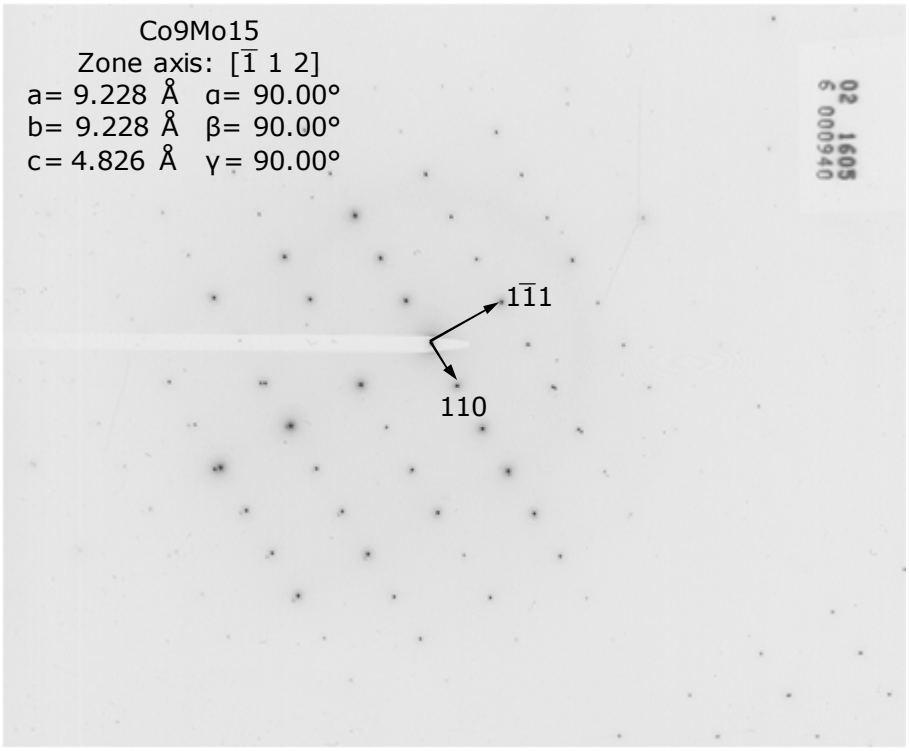

Figure 64 - Diffraction pattern from spot 2 within molybdenum rich hard phase in Figure 62

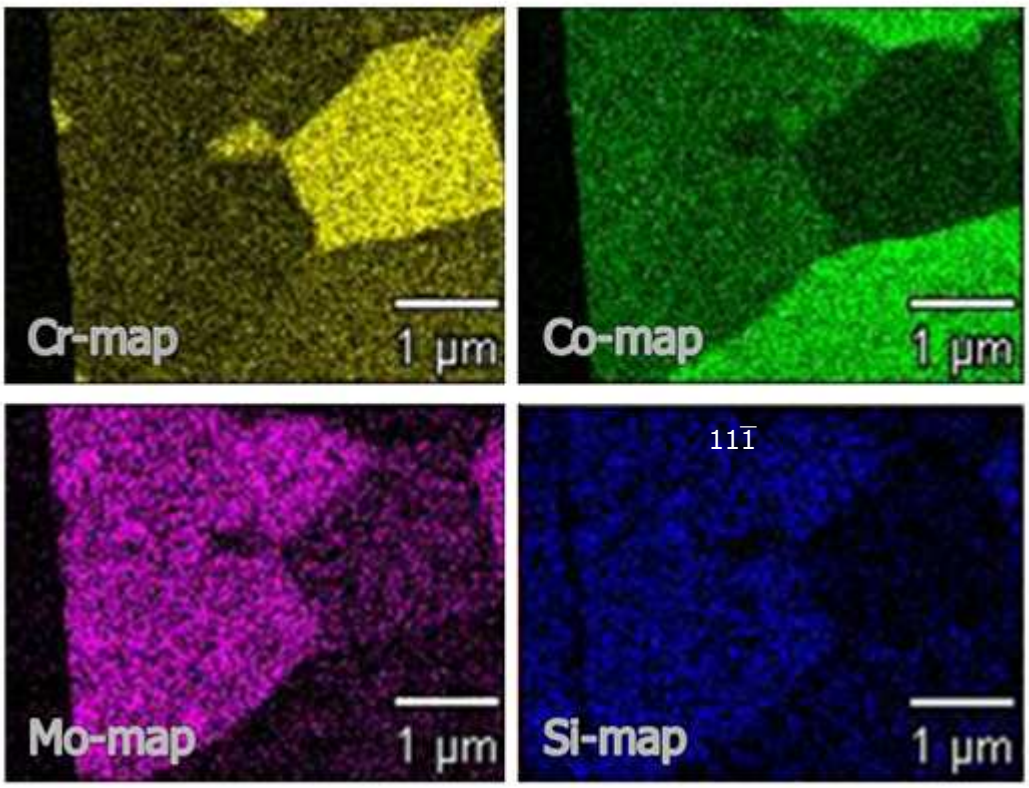

Figure 65 –EDS mapping across accumulated hard phases in PT09-238 head (Figure 62).

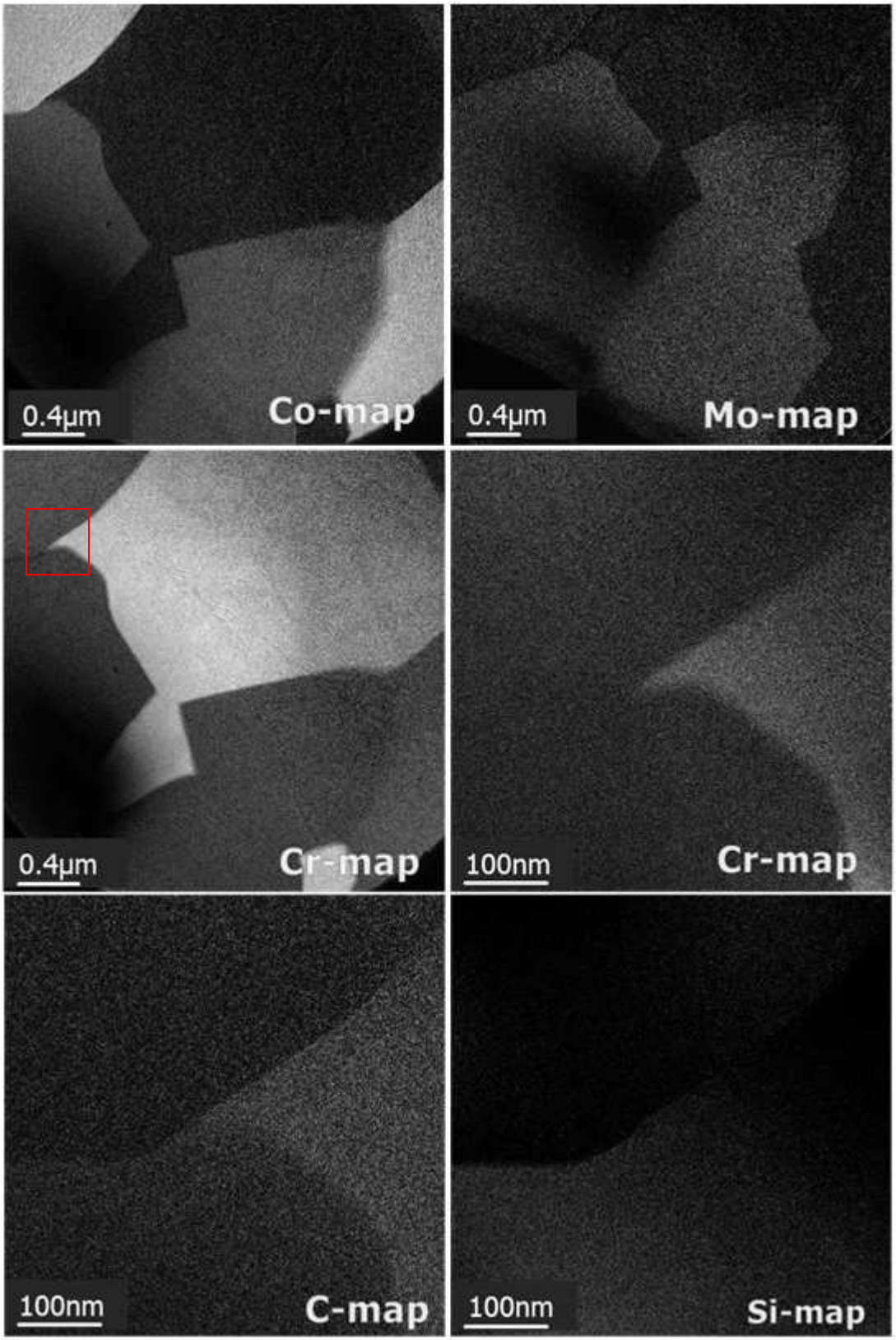

Figure 66 - EFTEM mapping across accumulated hard phases within PT-238 head (Figure 62).

9. Literature

[1] Gilbert JL. Metals. In: Callaghan JJ, Rosenberg AA, Rubash HE, editors. The Adult Hip, vol. 1. Philadelphia: Lippincott Williams and Wilkins, 2007

[2] Pourzal R. et al. How well do we know CoCrMo cast alloy? Annual meeting of the Orthopaedic Research Society 2011, Long Beach, CA, USA

[3] Flewitt PEJ, Wild RK. Grain Boundaries: Their Microstructure and Chemistry, Wiley, 2001

[4] Baley GW, Price RL, Voelkl E, Musselman IH. Microstructure and Microanalysis, Springer, 2001

[5] Hornbogen E, Eggeler G, Werner E. Werkstoffe, Aufbau und Eigenschaften von Keramik-, Metall-, Polymer-, und Verbundwerkstoffen, 9th edition, Springer, 2008

[6] Brody HD. Microsegregation. Casting, Vol 15, ASM Handbook, 2008; 338-347.

[7] Sha G, Yao L, Liao X Ringer SP, Duan ZC, Langdon TG. Segregation of solute elements st grain boundaries in an ultrafine grained Al-Zn-Mg-Cu alloy, Ultramicroscopy, Elsevier, 2010

[8] Oliver WC, Pharr GM. An improved technique for determining hardness an elastic modulus using load and displacement sensing indentation experiments, J. Mater. Res. Vol. 7, 1992

[9] Williams DB, Carter CB. Transmission Electron Microscopy, A Textbook for Materials Science, second edition, Springer, 2009

[10] Weiß S. Script Grundlagen der Elektronenmikroskopie

[11] Egerton RF. Electron Energy-Loss Spectroscopy in the Electron Microscopy, second edition, Plenum Press, 1996

[12] Cullity BD, Stock SR. Elements of X-Ray Diffraction, third edition, Prentice Hall, 2001

[13] Goodhew PJ, Humphreys J, Beanland R. Electron microscopy and analysis, third edition, Taylor & Francis, 2001

[14] Pourzal R. Possible Pathways of Particle Formation in CoCrMo Sliding Wear, 2011